MULTISCALE CONTINUUM-KINETIC MODELING OF IONIC EMISSION IN ELECTROSPRAY THRUSTERS

by

Amin Taziny

B.S., Binghamton University, 2019

M.S., University of Colorado, 2023

A thesis submitted to the

Faculty of the Graduate School of the

University of Colorado in partial fulfillment

of the requirements for the degree of

Doctor of Philosophy

Department of Aerospace Engineering Sciences

2025

Committee Members:

Iain D. Boyd, Chair

Brian M. Argrow

Jed Brown

John A. Evans

James A. Nabity

Taziny, Amin (Ph.D., Aerospace Engineering Sciences)

MULTISCALE CONTINUUM-KINETIC MODELING OF IONIC EMISSION IN ELECTROSPRAY THRUSTERS

Thesis directed by Prof. Iain D. Boyd

Electrospray thrusters are a class of electrostatic propulsion systems that utilize strong electric fields to extract and accelerate charged particles and/or droplets from a conductive fluid surface. A subset of electrospray thrusters include ionic liquid ion sources (ILISs) that operate in a purely ionic emission mode and utilize room temperature molten salts, otherwise known as ionic liquids, as propellant. ILISs have the highest specific impulse across electrospray thruster technologies and offer high efficiency and scalability for small satellite applications relative to conventional electric propulsion systems. Despite their potential, electrospray thrusters face critical challenges related to emission stability, plume characterization, and long-term operational reliability. This dissertation presents a coupled continuum-kinetic computational framework to model ionic emission from a single emitter ILIS configuration, coupling an electrohydrodynamic (EHD) meniscus model with a particle-in-cell (PIC) and direct simulation Monte Carlo (DSMC) plume model to characterize the multiscale process from the nanoscale emission dynamics at the emitter apex to the micronscale plume downstream. The first component of this work develops a physics-based EHD model to resolve the steady-state meniscus morphology and field-driven ionic emission from a porous emitter architecture. A finite-element approach is employed to solve Laplace's equation for the electric potential and Stokes flow for the ionic liquid hydrodynamics, capturing interfacial stresses governing meniscus formation. The resulting emission properties are then coupled to a kinetic PIC model, which simulates ion trajectories, Coulombic interactions, and fragmentation processes within the plume. A semi-empirical emission model is incorporated to improve computational efficiency and ensure compatibility with experimental data. This framework is

applied to analyze key electrospray thruster performance metrics, including emission current, thrust, and beam divergence. Sensitivity analyses are conducted to explore the effects of geometric and operational variations on plume characteristics, providing insights into failure mechanisms such as electrode overspray and grid contamination. The results inform design strategies to optimize emission stability and enhance thruster longevity. This dissertation contributes a novel end-to-end modeling approach for ionic electrospray emission, offering a computational toolset that aids in the development of next-generation ILIS thrusters.

Dedication

لأختي وماما. لأخويا و بابا.

Acknowledgements

A Ph.D., like most research, cannot be done without standing on the shoulders of giants. I will forever hold immense gratitude to those who have, directly and indirectly, paved the road for me and became a part of this journey that brought me to where I am today. When I think of this immense world and the infinite possibilities of what could have been, all I know for certain is that I am truly blessed.

It goes without saying that none of this would have been possible without my advisor, Professor Iain D. Boyd. Thank you for seeing the potential in me that I had yet to see in myself. For your gracious support, mentorship, and guidance throughout these years, I would not have reached this point without your steady hand and belief in me. Your wisdom, patience, and unwavering dedication to both the science and the people behind it have left an indelible mark on my academic and personal growth.

I would also like to extend my heartfelt thanks to Dr. Wai Hong Ronald Chan, whose mentorship was instrumental during the most formative stage of my Ph.D. journey. In those early years, when everything felt overwhelming and the path forward was uncertain, Ron provided the hands-on guidance, clarity, and encouragement I desperately needed.

I am deeply thankful for the vibrant and supportive community I found at CU Boulder. The SOARS program first welcomed me into a space where I saw myself reflected in science and felt empowered to belong. That early encouragement laid a foundation of confidence that carried into graduate school. To the incredible members of my lab—thank you for the camaraderie, collaboration, and for turning the office into a highly efficient procrastination

hub disguised as a workspace. Tim Aiken, Tommy Kava, Charles Lipscomb, Matthew Stasiukevicius, Kal Monroe, Marisa Petrusky, Mitch Wall, Jens Rataczak, and Jenny Horing—I couldn't have asked for better colleagues and friends.

Lastly, I would like to thank my wonderful partner Camila for her unwavering support, love, and for relentlessly calling me "Mister" throughout the years, annoying me just enough to find the motivation I needed to reach the finish line. And to my cat Jiji—thank you for being delightfully derpy and reminding me every day that life doesn't have to be as serious as we sometimes make it out to be.

Contents

Chapter

Tables

Table

Figures

Figure

Chapter 1

Introduction

1.1 Electric Propulsion

The mid-20th century marked the beginning of the Space Age, ushering in an era of rapid advancements in spacecraft propulsion technology that continues to this day. Among these developments include electric propulsion (EP) systems, a class of space propulsion technologies that utilizes electricity to accelerate a propellant and generate thrust [87]. The source of this electrical power is derived externally (for example, from a solar array), which uniquely characterizes EP systems relative to chemical propulsion systems where the energy is stored in molecular bonds within the fuel. This allows the designers of EP devices to focus on how to most efficiently utilize the propellant, which is achieved by maximizing the exhaust velocity.

Efficiency is quantified by the thruster specific impulse, a metric that measures the amount of impulse a thruster can generate per unit of expended mass. While most chemical thrusters cannot surpass specific impulses of about 500 seconds, EP systems can exceed this value by more than an order of magnitude [75]. As a result, a spacecraft requires comparatively less fuel to execute a given mission, freeing up crucial mass and volume that can be allocated to the payload, thereby maximizing mission capability. Alternatively, the reduced propellant mass could be used to lower the overall mass of a spacecraft or satellite, leading to a reduced cost in launch costs and increased accessibility to space that has contributed to the recent proliferation of small satellites [1, 68, 74, 102].

The history of EP dates back more than a century, beginning with the theoretical basis that ionized gasses could propel spacecraft that was independently postulated by both Robert Goddard in America as early as 1906 [53] and Konstantin Tsiolkovsky in Russia in 1911 [93]. From there, EP as we know it was first qualitatively and publicly conceptualized by Herman Oberth in 1929 [101] and later refined by British physicists Shepard and Cleaver in 1949 with the first quantitative study of the practicality of electrostatic propulsion for deep-space missions [112]. These scientists laid the groundwork for the seminal research of Ernest Stühlinger in the mid-1950s, whose systemic analysis on the feasibility of EP systems [116–118] helped transition the field from a conceptual idea to a burgeoning discipline with profound technological potential that continues to advance till this day.

Once established as a viable means of space propulsion, several EP research initiatives emerged during the 1960s. In the U.S., these included programs at NASA's Glenn Research Center, Jet Propulsion Laboratory, and Hughes Research Laboratories. At the same time, several programs were also begun at various Russian research institutions. This newfound focus among Cold War superpowers quickly culminated with the first in-space demonstration of EP in 1964 with NASA's SERT-1 probe and shortly thereafter the USSR's Zond-2 satellite, where each spacecraft can be seen in Fig. 1.1. The former featured a electrostatic gridded ion thruster while the latter featured a pulsed plasma thruster [87]. Since then, EP technology has only continued with its rapid development, where today it is widely implemented across commercial, defense, and civil space mission applications. By the end of 2019, approximately 600 spacecraft had been launched incorporating some variation of EP [75]. Today, its implementation has exponentially grown mainly due to the launch of SpaceX's StarLink satellites equipped with Hall-effect thrusters. By the end of 2024, over 7,000 have been launched out of a planned total of 12,000, where a possible future extension could extend the fleet to over 34,000 satellites [88].

Modern EP systems can be partitioned into one of three broad categories depending on the acceleration mechanism through which thrust is generated: electrothermal, electro-

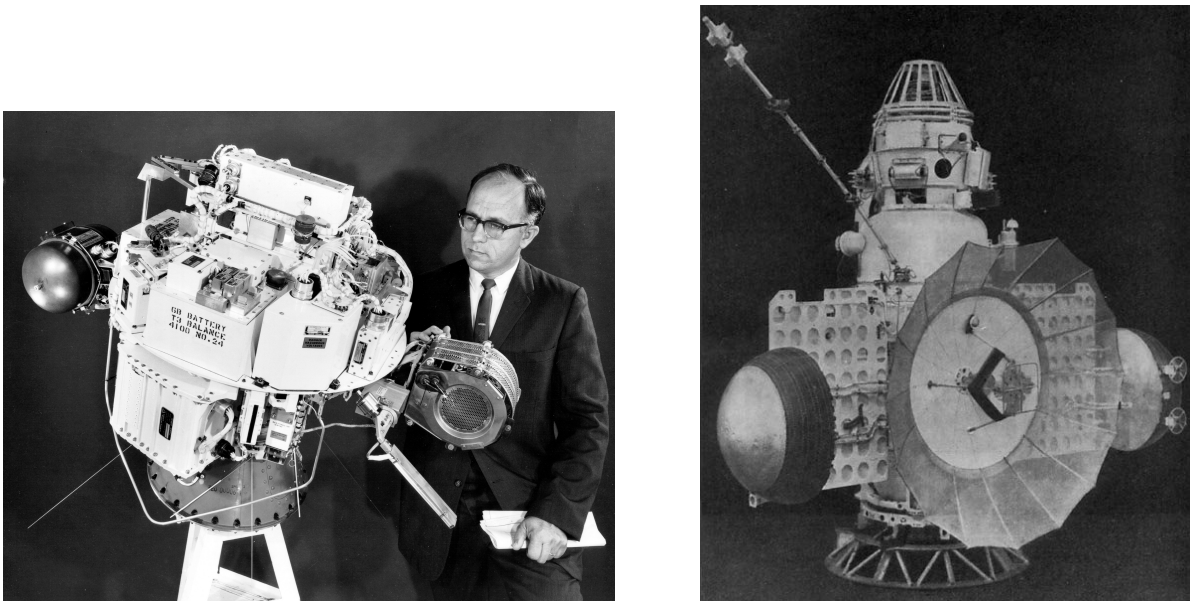

(a) **(b)**

Figure 1.1: Photographs of (a) NASA's SERT-1 (Space Electric Rocket Test) satellite alongside project manager Raymond J. Rulis and (b) Russia's Zond-2 satellite. Both spacecraft launched in 1964 and were their respective country's first probes to successfully navigate using EP.

magnetic, and electrostatic [87]. Electrothermal propulsion systems use electricity to heat a propellant, which is subsequently accelerated using a converging/diverging nozzle. Arcjets and resistojets are the most common forms of electrothermal thrusters and vary in the method of which they heat and accelerate propellants. Electromagnetic propulsion devices generate thrust through the interaction of both electric and magnetic fields with the propellant. These include pulsed plasma thrusters (PPTs) and magnetoplasmadynamic thrusters (MPDTs). PPTs use electric arcs to ablate a solid propellant into a plasma, which acts as a circuit between two electrodes and is subsequently accelerated by the force acting perpendicular to the current flow. MPDTs generate plasmas by ionizing a gaseous material, where the charged species are accelerated using either an applied or induced magnetic field through the Lorentz force. Finally, electrostatic propulsion systems are characterized by their use of

Table 1.1: Typical performance metrics and propellants utilized within various spacecraft EP systems.

EP System	I_{sp} [s]	Thrust [N]	Power [kW]	Propellant	Ref.
Electrothermal					
Arcjet	400–500	0.1	1	N_2H_4, NH_3	[40, 137]
Resistojet	100–300	0.2	0.1–1	N_2H_4, N_2, Xe	[129, 137]
Electromagnetic					
Hall thruster	1500	10^{-2}–1	0.2–20	Xe	[67, 106]
MPD thruster	1000-10000	0.5–50	10^2–10^3	Ar, H_2, Li	[59, 71]
Ablative PPT	500–1500	10^{-5}–10^{-2}	10^{-2}	PTFE	[2, 126]
Electrostatic					
Gridded ion engine	3000	10^{-3}–10^{-1}	0.1–5	Xe	[21, 119]
Electrospray	1000-5000	10^{-6}–10^{-4}	10^{-4}	EMI-BF_4, EMIM	[18, 68]

static electric fields between electrodes to accelerate charged species, where common examples include Hall-effect thrusters (HETs) and gridded ion thrusters (GITs). HETs utilize cross-field discharges that are defined by the Hall effect to both ionize a gas and accelerate the resulting plasma, while GITs operate by using a variation of techniques to initially generate a plasma that is exposed to a series of biased grids that eject the positively charged species. Another form of electrostatic propulsion—and the system that the remainder of this dissertation will focus upon—are electrospray thrusters, and is further described in the subsequent sections. Typical performance metrics and propellants utilized in the aforementioned EP systems can be found in Table 1.1.

1.2 Electrospray Thrusters

1.2.1 Characterization

Electrospray thrusters are EP devices where an electrostatic field is applied to a conductive liquid propellant, generating thrust with the extraction of droplets and/or ions from the surface [1]. These systems are generally available in one of three variations that are

characterized by the propellant used and emission modes they operate in. Colloid thrusters use electrolytic solutions such as doped glycerol as propellants [98] and operate almost exclusively in a droplet emission mode. Field emission electric propulsion (FEEP), also known as liquid metal ion sources, utilize liquid metals such as Cesium and Indium and operate predominantly in an ionic emission mode. Finally, ionic liquid ion sources (ILISs) are thrusters that use room temperature molten salts, known as ionic liquids, as propellant and can operate in both droplet and ion emission modes.

Since typical current levels emanating from a single emitter range from tens of nano-Amperes to several micro-Amperes [55, 56], electrospray thrusters are often operated in arrays of several hundred emitters to increase the performance capacity, a process known as multiplexing. Across all thruster types, emission is enabled by the application of a potential bias across two electrodes. Typically, one of these electrodes is the emitter itself and is often shaped into a needle-like structure to focus the applied field strength towards the tip and localize the site of emission. The means by which the emitter is wetted with propellant is dependent on the emitter architecture. Externally-wetted emitters employ solid needle tips that openly transport propellant over their external surface. These architectures are employed in LMIS thrusters, where emitters are heated to sustain the liquid state of the metal, and the large contact surface between the propellant and the emitter facilitates efficient heat transfer. However, such open architectures restrict the selection of propellant to those with low vapor pressures as to function in a vacuum environment. Capillary emitters, on the other hand, employ closed architectures where propellant is internally transported within thin tube electrodes, restricting exposure with the external environment to the free surface end. These geometries are well-suited to traditional colloid thrusters as they support pressurized flow-control systems, simultaneously enabling a wider range of applicable working liquids and higher mass flow rates that would otherwise be untenable with passive flow configurations. Lastly, porous emitters employ a hybrid of both open and closed architectures, transporting propellant passively through a porous material. A schematic of porous emitters operating

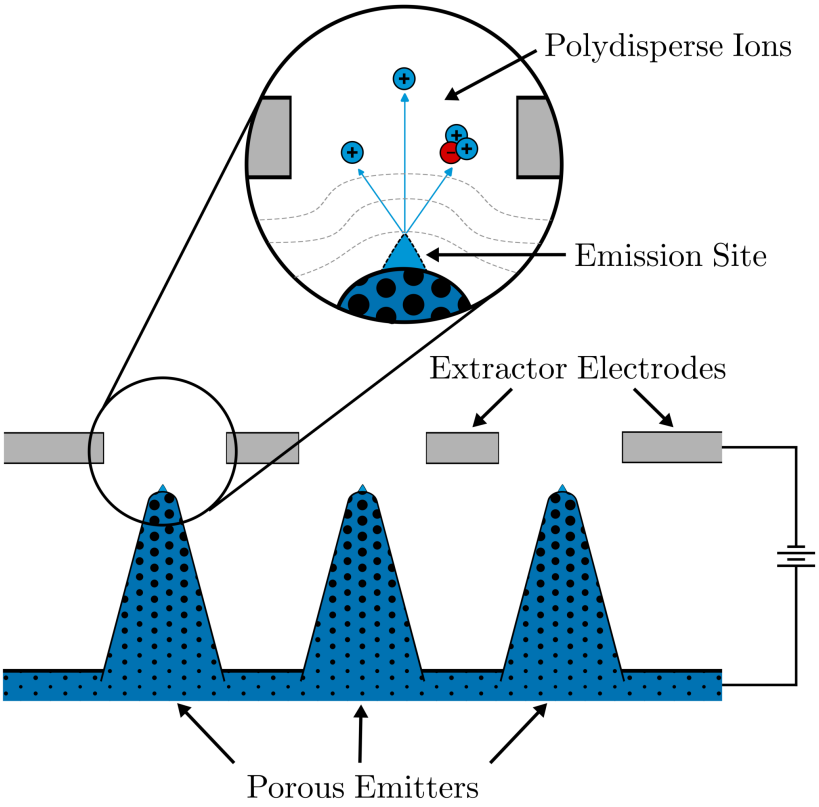

Figure 1.2: Schematic of porous electrospray emitters operating in a positive ionic emission mode. At the apex, an emission site is shown where several polydisperse ions emerge with varying degree of solvation.

within an ILIS configuration is presented in Fig. 1.2. The greater Laplace pressure induced by the porous geometry enables the hydraulic capability of closed architectures while still mitigating the challenges of clogging and overflow that is addressed by open architectures. These configurations are often employed in ILIS thrusters as the large hydraulic impedance is conducive to a purely ionic emission mode, further described in Chapter 2 where the physics governing all electrospray emission is presented.

1.2.2 Motivation

Electrosprays were studied extensively as propulsion systems in the mid-20th century through colloid thrusters [11, 84, 97, 104]. At the time, they were viewed as potential

alternatives to ion engines as the larger mass of the droplets enabled comparatively higher thrust densities and thus propulsive capability. Colloid thrusters developed during this period demonstrated performance metrics ranging approximately from 1–300 μN of thrust per emitter and 400–1,400 seconds of specific impulse [97]. Despite this initial success, interest in electrospray propulsion research gradually diminished in the ensuing decades as spacecraft continued to grow in size, and the microNewton-level thrust produced by these systems was no longer sufficient to meet the increasingly demanding requirements of missions.

After several decades, electrospray research experienced a renaissance beginning in the late 1990s as the demand for micropropulsion systems emerged with the onset of formation flying missions [98]. The former refers to a class of missions where several spacecraft are flown in a coordinated matter and maintain precise relative positions and orientations, often designed for scientific observations, satellite constellations, or interferometry. A notable example includes NASA's Laser Interferometry Space Antenna (LISA), a planned probe that would be the first dedicated space-based gravitational-wave observatory [134, 135]. Such a mission requires several satellites operating in a noise-free environment and capable of counteracting external disturbances on the order of 100 nano-Newtons. In 2015 the LISA Pathfinder was launched, equipped with eight colloidal thrusters developed by Busek in collaboration with the Jet Propulsion Laboratory as a technology demonstration mission [136]. Once reaching the Sun-Earth Lagrange Point 1, the thrusters were operational for approximately 2,500 hours and successfully met all of the mission criteria. The success of the LISA Pathfinder mission validated the feasibility of electrospray propulsion for precise spacecraft maneuvers, paving the way for its integration into missions with similar requirements.

At the same time, the shrinking of instrumentation and increased accessibility to space at the turn of the 21st century led to a proliferation of small satellites [74]; thus, necessitating a propulsive device that can be scaled down to accommodate this new class of spacecraft. Electrospray thrusters are uniquely suitable for micropropulsion relative to other EP systems for several reasons. Firstly, the micron-scale of emitters are desirable for the stringent volume

and mass limitations of small satellites. ILISs in particular utilize low vapor pressure ionic liquids that are passively-fed via capillary action, precluding the need for pressurization or flow control systems that further act to increase the compactness. Secondly, electrosprays lack an active ionization process, which, in traditional EP devices, imposes significant constraints on miniaturization. The heating associated with ionization in traditional EP systems become increasingly inefficient at smaller scales, leading to performance losses [102]. By contrast, electrospray thrusters operate without this limitation, reducing the overall thermal load and making them inherently more scalable for small satellite applications. Finally, advancements in micromachining/microelectromechanical systems (MEMS) fabrication methods have enabled the efficient packing of hundreds of emitters into small packages [75], simultaneously increasing thrust density and minimizing device volume.

Henceforth, the focus of this dissertation will be on ILIS thruster configurations. In addition to their aforementioned applicability in micropropulsion, they uniquely offer the highest specific impulses across electrospray thruster technologies. This is due to their pure-ion emission mode, made possible by the combination of ionic liquid propellant and a porous emitter architecture. A full description of the physics governing ion emission in ILIS thrusters and how this relates to greater propellant efficiency is presented in Chapter 2.

1.2.3 Life-Limiting Mechanisms

Electrosprays hold immense potential as scalable and efficient EP devices but have yet to realize their full potential due to various failure modes that have precluded their wide deployment across miniturized spacecraft [20, 124]. Specifically within ILIS thrusters, there exists several challenges that have prevented successful operation on the order of thousands of hours as was demonstrated by the colloid thruster flown on NASA's LISA Pathfinder mission. One significant roadblock is the progressive electrochemical degradation of the thruster at liquid-electrode interfaces as a result of chemical non-neutrality. At these interfaces, the Coulombic nature of ionic liquids results in the emergence of a double layer (DL) as the free

charges within the propellant act to screen the surface charge of opposite polarity present on the electrode. During operation the DLs within a given emitter grow in magnitude as the bulk ionic liquid is no longer quasi-neutral and current is lost during the field-evaporation process. If left unaddressed, the potential gradient across the DL will grow and act analogously to a capacitor, eventually manifesting as discharge current that not only decomposes the propellant and corrodes the electrode, but can result in short circuits where the failure of a single emitter in a grid can hinder the operation of an entire multiplexed array [19]. It can been shown that using voltage alternation, where the polarity of the emitter is switched at frequencies of approximately 1 Hz, the DL can be maintained under its electrochemical window limit and undesired electric reactions can be mitigated [80].

However, electrochemical reactions are only one of several first-tier mechanisms that influence the lifetime of electrospray thrusters. First-tier mechanisms directly emerge from the fundamental design geometry, operation, and material and propellant selection of the thruster [124]. How the thruster is designed and operated may also lead to other first-tier mechanisms such as grid overspray, where emitted propellant impinges on a downstream electrodes instead of accelerating past it. These processes may lead to additional, secondary mechanisms that ultimately result in failure of the device's power processing unit (PPU) and thus overall thruster operation. For example, continued overspray over a porous electrode will eventually result in saturation that would curtail the applied field strength, reducing emitter efficiency. Excessive saturation may even screen out the surface charge completely in localized areas of the grid, resulting in propellant pooling that repels incoming ions back in the upstream direction, a secondary mechanism known as backspraying that only accelerates the lifetime reduction of the thruster.

Electrode overspray is considered the primary mechanism of concern in electrospray design [135, 136] and is the failure mode that the work of this dissertation will focus upon. Generally, overspray can be partitioned into one of two submechanisms, distinguished by the upstream processes that initiate the failure mode. The first, direct overspray, occurs when

emitted propellant flux impinges directly onto the extractor or accelerating electrode rather than passing cleanly through the grid aperture. This phenomenon is primarily dictated by the geometric configuration of the thruster, emitter-electrode alignment, and the operating conditions under which the device is run, such as applied voltage and upstream flow rate in actively-fed thrusters. The second submechanism arises from physics governing the plume evolution downstream of the emitter. In this case, overspray results from the radial expansion of charged species due to Coulombic repulsion or the fragmentation of solvated ion clusters, where neutral byproducts from dissociation are generated with trajectories that deviate from the applied electric field streamlines. Because neutrals are unaffected by electrostatic forces, they propagate along ballistic paths dictated by their initial fragmentation momentum, contributing to unintended deposition on downstream components. The cumulative effect of either submechanism can lead to progressive electrode contamination and saturation, ultimately diminishing the operational lifespan and performance of the thruster. Consequently, understanding and mitigating both forms of overspray are critical to ensuring the long-term viability of electrospray systems.

Characterizing the onset overspray is particularly well-suited to computational modeling. Various simulations could be executed in parallel for exploring design/operational configuration spaces and can be used to identify conditions under which direct overspray is likely to occur. By leveraging simulations, one can rapidly evaluate a wide range of geometric and operational parameters that would otherwise be impractical or prohibitively expensive to test experimentally. Furthermore, simulations serve as a valuable complement to experimental efforts by helping refine testing parameters, ensuring that laboratory studies focus on the most relevant regions of the operational space. Beyond direct overspray, numerical models are also advantageous for investigating secondary overspray mechanisms such as radial plume expansion. Unlike experiments, simulations offer precise control over physical processes, enabling the isolation of Coulombic repulsion and fragmentation effects by selectively enabling or disabling them in the model. This allows for a quantifiable assessment of each contribution

to plume divergence, offering insights into the fundamental physics that govern overspray behavior. By integrating computational modeling with experimental validation, a more comprehensive understanding of mechanisms contributing to overspray can be achieved, informing design strategies that mitigate failure modes and enhance the long-term reliability of electrospray thrusters.

1.3 Review of Ionic Liquid Ion Source Modeling

Higuera [62] was the first to model the electrokinetics and ionic evaporation process within the meniscus of ionic liquid, building upon his earlier work where he simulated cone-jet emission [60]. He accomplished this by implementing the leaky-dielectric model (LDM), a simplified framework on the electrohydrodynamics of fluids with small but finite conductivities in response to an applied field. LDM was first introduced by Taylor et al. [122] and later expanded by Melcher and Taylor [92], where a complete review of the model is offered by Saville [110]. LDM addresses the unique electrokinetics of fluids with poor conductivities as they do not demonstrate the level of conductance observed in traditional conductors with free charge distributions but also do not have the level of resistivity observed in traditional insulators. Instead, when an external field is applied to a leaky dielectric fluid, free charges within the bulk travel in finite timescales on the order of the charge relaxation time, defined as the ratio of the fluid relative permittivity to the conductivity. When this fluid shares an interface with another dielectric or an insulator, the imbalance in conduction results in a net surface charge. The result is that the bulk fluid can be assumed absent of free charge, and the interface is subject to boundary conditions that enforce the normal component of the electric displacement jump. The interfacial charges interact with the applied electric field to generate forces that can deform the interface and drive fluid motion. LDM addresses this by reducing the full Maxwell stress equations to a tractable set that captures the essential physics of “leaky” conductors and can be applied as interfacial boundary conditions.

Higuera implemented the LDM framework to model the response of a fixed volume of

liquid in vacuum resting on a metallic plate and under a uniform electric field. The physical domain was partitioned into three numerical regimes that encapsulate the liquid droplet, the vacuum, and the interfacial meniscus. A Laplacian model of the electric potential was used within the liquid and vacuum domains and a Stokes model was used for the liquid hydrodynamics. These choices were justified using a scaling law analysis that demonstrated, to first order, the effects of space charge are negligible and do not need to be accounted for in the potential model. This behavior is unlike what is observed in liquid metal ion sources where significant space charge effects are present, however in ILISs this current is bounded by the finite conductivity of the ionic liquid. Additionally the scaling law analysis found that the meniscus hydrodynamics were dominated by the liquid viscosity and that the relative internal forces from the evaporated mass flux were negligible in comparison, resulting in the Stokes flow approximation.

Compared to the original Taylor analysis, Higera's numerical model did not assume an initial meniscus morphology, and steady-state solutions were found through a pseudo-timestepping routine via a Runge-Kutta method in conjunction with boundary element methods to solve the Laplace and Stokes problems. Two emission cases were explored, one where the liquid volume was fixed and another where the flow was controlled by an upstream feeding line. In the fixed-volume simulations, Higuera found the emission current had a functional dependence on the electric field and qualitatively demonstrated the empirically-observed phenomena of a starting voltage. The current profiles revealed negligible emission regimes with low fields and a conduction-driven emission regime at higher field strengths.

In the feeding flow case, the input flow rate was assumed proportional to the combination of an upstream reservoir pressure and the force exerted by the ionic liquid on the metallic plate. The resulting traces of the emission current and field behavior were found to be very sensitive to the hydraulic impedance and feed pressure, likely due to the feeding model. For example, the force exerted on the plate by the ionic liquid likely is not present in capillary or porous emitter architectures. These limitations were addressed by Coffman [31][30], where they

built upon Higuera's model by expanding the simulated parameter space, included a more rigorous feeding architecture, and introduced the effects of Ohmic heating. Their simulations unfolded additional equilibrium meniscus structures that emerge when the meniscus size is large relative to the characteristic emission length scale localized at the apex. Within this parameter space, the meniscus morphology was found to be predominantly a function of the applied potential gradient and that, in accordance with Higuera, the emission characteristics are heavily dependent on the feeding flow architecture. In the operational space of relatively high applied fields and large menisci, the meniscus regularizes and the emission current appears to be bounded to the order of the characteristic emission current. As the feeding conditions are passive in an ILIS and are governed by the emission characteristics, the authors were also able to quantify the relative bounds of the upstream pressure corresponding to the aforementioned current limit.

EHD modeling of ILIS menisci continued to evolve with simulations conducted by Gallud and Lozano [47] that further expanded the operational space by which stable menisci geometries were sought, better elucidating the bounds of stability and range of emission characteristics across meniscus sizes, hydraulic impedances, and applied field strengths. The capability of the EHD model was also improved by including the effects of bulk free charge within the ionic liquid that arise from thermal gradients that in turn produce conductivity gradients. This broad parameter space exploration allowed the authors to characterize emission and menisci behavior into four broad regions, three of which resulted in stable menisci geometries. The first stable region corresponds to a low field strength and little to no emission is observed, similar to the low field regimes described earlier by Higuera and Coffman. The second stable region corresponds to large menisci, similar to that explored by Coffman et al. [30], and are characterized by a minimum hydraulic impedance and an emission current that is bounded to the order of the characteristic current size. The additional considerations of the study allowed the authors to further categorize this region into two subregions, where at higher field strengths the meniscus is prone to several uncharacterized

instabilities such as bifurication that may be numerical or physical in nature. An additional region was also identified at smaller meniscus sizes, where the interfacial pressure drop from emission plays a larger role in the meniscus stability. The authors found that the field strength threshold at which instability occurs in this region decreases as the hydraulic impedance is increased. The additional temperature dependence introduced in the EHD model also allowed the authors to investigate the role of energy transport, as neglecting this may result in an underapproximation of current. The authors found that ohmic heating was largely dissipated via conduction across the meniscus in all stable regimes. They found agreement with the assumptions made in previous literature that pure ion emitting electrosprays largely run cold as the thermal diffusivity of the emitter electrodes is significantly larger than that of the ionic liquid propellant.

Complete ILIS thruster modeling must, of course, account for the downstream ion dynamics of the plume that occur subsequent to the field emission process. Various studies have been conducted that focus solely on high-fidelity simulation of the ionic plume with minimal emphasis placed upon the initializing conditions [4, 14, 15, 33, 41, 79, 82, 89–91, 133]. For this reason, these works are largely outside the scope of this dissertation and are not reviewed here for the sake of brevity. More interestingly, recent studies have begun exploring multiscale frameworks that resolve both nanoscale emission phenomena and millimeter scale plume dynamics [3, 100].

One such study of particular interest to this dissertation is that of Petro et al. [105], where the EHD model built by Coffman and expanded by Gallud is coupled with a kinetic plume model. Ion trajectories are initialized on the steady-state meniscus and are advected downstream and radially by the applied electric field and intermolecular Coulombic repulsion. The background field is provided by the EHD model and the space charge field is explicitly calculated in the particle trajectory time integration using Coulomb's law. The ion trajectories are initialized using the spatial distribution of current density across the meniscus, and their initial velocities correspond to the normal velocity of the fluid at their interfacial location. The

explicit time-stepping coupled with the Coulombic space charge calculation requires refined timestepping, so the authors partition the computational domain of the plume into several regions where the rate at which inter-particle force calculations are made is progressively relaxed. The authors also included a subroutine within the plume that accounts for the fragmentation of solvated ion clusters. This fragmentation occurs in response to both the large internal energy of ion clusters and the applied field that reduces the working function that governs the dissociation process. The authors utilize both empirical data and high-fidelity molecular dynamics results to approximate fragmentation rates for the most commonly observed species in ILIS plumes and validate the energy distribution of their simulated beam against retarding potential analyzer measurements. Collisions are not explicitly accounted for in their model and collision rates were approximated using steady-state density and velocity profiles of each emitted species. The multiscale nature of this work represents a remarkable milestone in single emitter ILIS modeling, and paves the way for additional domain expansion and simulation of multiplexed emitter arrays. However, the n-body numerical approach implemented in their study is computationally expensive with a time complexity of $\mathcal{O}(n^2)$, becoming exponentially prohibitive with longer simulation times. For this reason simulations of the multiscale model were bounded to 20 nanoseconds or less, reducing the length scale at which plume phenomena can be studied and the feasibility of expanding into multi-emitter domains. These limitations invite the formulation of an alternative end-to-end framework that more efficiently resolves the ion dynamics within the plume without the cost of fidelity, enabling simulation time scales on the order of microseconds or longer.

1.4 Scope and Outline of Dissertation

The scope of this dissertation is the development and numerical implementation of a novel end-to-end single emitter model for ILIS electrospray thrusters and demonstration of how simulations can assist in the mitigation of select failure mechanisms via design space exploration and sensitivity analyses. This end-to-end emitter model requires an emission

submodel to resolve the total emission current from a steady-state interface that emerges from the balance between electrohydrodynamic phenomena within the conductive propellant and the applied electric field from the extractor electrodes. An additional plume submodel is required whose initial conditions are specified by the output of the emission model. The plume submodel would then resolve the trajectories of the evaporated ions subject to an applied electric field, inter-species Coulombic repulsion, and fragmentation of larger clusters into neutral and non-neutral species. Once established, the end-to-end model is used within a design space exploration and for sensitivity analysis using response surfaces to quantify how spatial characteristics of the plume respond to select geometric and operational conditions. To provide a structured discussion of this work, the following chapters outline the theoretical development, implementation, and analysis of the end-to-end emitter model in detail.

Chapter 2 establishes the fundamental physics underlying electrospray thruster emission across all operational modes. It begins with the formation of a canonical structure known as a Taylor cone that emerges when a conductive fluid is exposed to an applied potential gradient and occurs due to the balance between hydrostatic pressure, capillary forces, and electrostatic stresses. The chapter derives key scaling laws that lead to the universal Taylor cone angle and elucidates how these relationships govern the cone-jet emission mode, including expressions for the characteristic jet diameter, emission current, and droplet size. The analysis continues with the transition from a cone-jet emission mode to a mixed ion-droplet emission mode and ultimately a purely ionic emission mode that is characteristic of ILIS thrusters. Emphasis is given on the physics of pure ion emission, as the chapter reviews the mechanics of ion evaporation using ionic fluids and develops additional scaling laws that link thruster performance to fundamental properties of the working liquid. Overall, the chapter lays the mathematical and physical foundation of electrospray emission that underpins the numerical models that are presented in the subsequent chapters.

Chapter 3 introduces a comprehensive electrohydrodynamic (EHD) meniscus model for simulating steady-state ionic emission. It formulates a two-phase physics-based model

by coupling Laplace's equation for the electric potential in the vacuum and liquid domains, the Stokes equations for the hydrodynamics within the liquid, and various electrokinetic and surface charge boundary conditions at the liquid–vacuum interface. The chapter details the derivation of interfacial stress balances, including the projection of Maxwell and fluid stress tensors, and presents the numerical implementation using a two-phase finite element method within the DUNE library framework. A global coupling algorithm is presented that iteratively perturbs the meniscus shape to achieve convergence towards a steady-state morphology. Verification test cases for the Laplace and Stokes solvers are introduced to validate the approach, and simulation results are compared with established literature, with discussions on numerical challenges and areas for future refinement.

Chapter 4 extends the meniscus-level simulations from the previous chapter into a full end-to-end framework for modeling single-emitter ionic emission by coupling a kinetic plume model that extends into the far-field downstream from the extractor electrode. A semi-empirical emission model trained on AFRL's AFET-2 thruster is introduced that substitutes the capability of the original EHD model in certain operating conditions and is used due to numerical challenges in the EHD model that precluded simulations from finding steady-state meniscus configurations across operational conditions. The emission-plume coupling is implemented as a one-way boundary condition that approximates the number density of ionic species using the total emitted current. These species number densities initialize the kinetic model, which combines Direct Simulation Monte Carlo (DSMC) for tracking rarefied gas dynamics with a Particle-In-Cell (PIC) method tailored to single-polarity ionic plumes. Key enhancements are made to the original kinetic model to account for single-polarity ionic plumes, including a direct Poisson solver for non-quasineutral conditions and a field-free fragmentation model to simulate the dissociation of solvated ion clusters. Finally, simulation results for emission current, thrust, and plume spatial characteristics are evaluated against experimental measurements from the AFET-2 thruster.

Chapter 5 demonstrates an example of how the end-to-end framework could be imple-

mented to inform future ILIS design. Specifically, the chapter investigates how variations in operational and geometric conditions affect spatial characteristics of the plume. A two-dimensional case is conducted where extractor voltage and tip-to-extractor distances are perturbed and their relative influence on plume width, sharpness, and tilt are studied using super-Gaussian parameterizations of current density and beam intensity profiles. Surrogate models are established to efficiently map the relationship between the design space and plume characteristics, as well as enable sensitivity analysis studied. The chapter extends this analysis with a three-dimensional case that studies the influence of translational and rotational misalignments on plume characteristics, mimicking manufacturing variations of ILIS emitters during thruster fabrication. Ultimately, the surrogate-based exploration provides actionable insights for optimizing future ILIS thruster designs.

Chapter 6 concludes this dissertation, beginning with a summary of the work and findings from each previous chapter. The chapter enumerates the novel contributions of the conducted research, including the unique formulations of the EHD model, the development of a modular finite element solver, the introduction of a semi-empirical ionic emission model calibrated with experimental data, the extension of a DSMC/PIC solver to handle single-polarity plumes with fragmentation, and the application of surrogate models for efficient sensitivity analyses. Finally, the chapter presents recommendations for future work, including improvements in implemented numerical methods, stronger coupling between emission and plume solvers, enhanced fragmentation models, expanded design spaces, and multi-emitter simulations.

Chapter 2

Governing Physics of Electrospray Emission

This chapter explores the underlying mechanisms that dictate the formation and behavior of Taylor cones, the emergence of various emission modes from them, and the critical parameters that characterize their performance. By establishing these foundational principles, this chapter provides the theoretical groundwork necessary for the numerical models derived in subsequent chapters.

2.1 Taylor Cones

The fundamental characterization of all electrosprays is that the source of their emission emerge from the apices of Taylor Cones. Taylor cones occur when the interface between a conductive fluid and an insulator (normally air or a vacuum, but dielectric liquids have been used as well [8]) are electrically stressed past a critical threshold of stability. Sub-critical stressing of the meniscus from an initial, rounded shape has been shown to follow the behavior (to first order) of an inviscid, conductive liquid on a planar surface charged by a uniform electric field [70, 120, 131, 132] known as a Frenkiel instability. Once the instability threshold is met, the smooth and continuous interface is transformed into a novel structure with conical features. Although other metastable structures may exist prior to this transformation assuming an initial spheroidal morphology [69], this transition is often viewed as an instantaneous process.

A schematic of this snap-off process for a capillary electrospray source is presented in

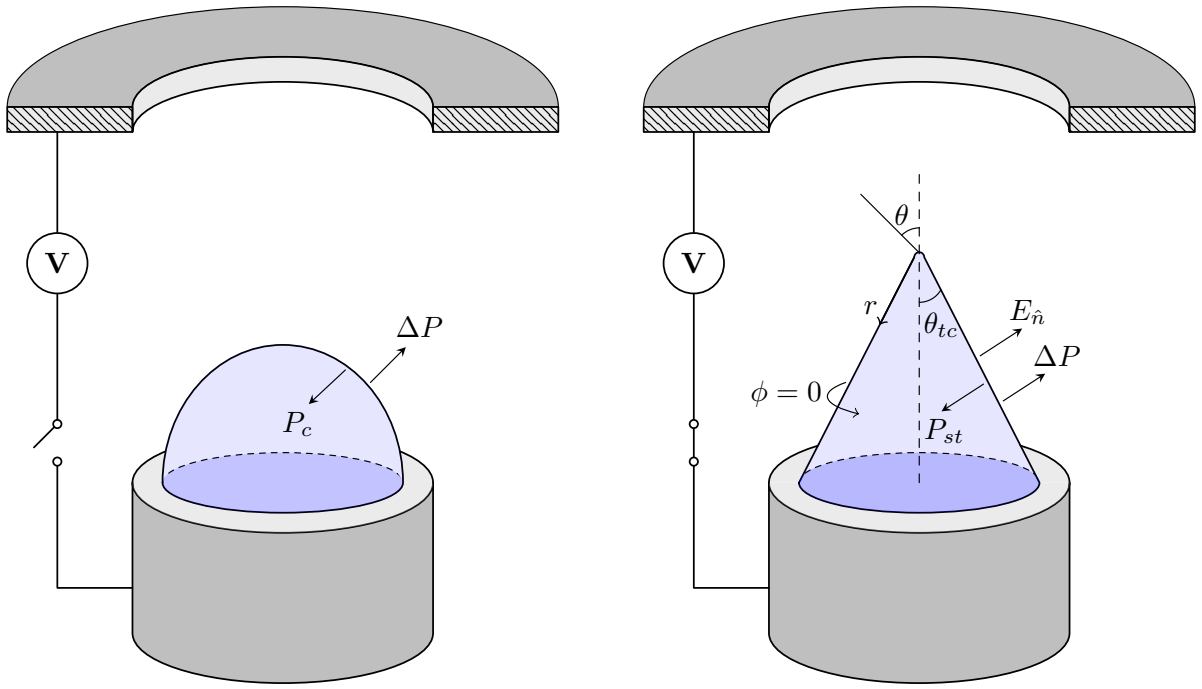

(a) **(b)**

Figure 2.1: Schematic of Taylor cone formation within a capillary-based electrospray configuration. In (a) where no potential gradient is applied, a spheroidal droplet is formed that balances the interfacial pressure jump across the meniscus, ΔP, from upstream inlet conditions and the capillary pressure, P_c. Application of a potential gradient in (b) results in an equipotential cone-like structure that balances the interfacial pressure jump ΔP, the electric field traction normal to the surface E_n, and the surface tension pressure from the working liquid P_{st}.

Fig. 2.1. Initially, before a potential gradient is applied between the capillary and electrode shown in Fig. 2.1a, the conductive liquid at the free surface will form into a spheroidal structure. The resultant topography emerges from the force balance between the hydrostatic pressure jump across the meniscus, ΔP, and the capillary pressure, P_c. ΔP is set based on the feeding mechanism and thus is dependent on the electrospray configuration utilized. However, the value of the interfacial pressure gradient can be generally determined using

$$\Delta P = P_B - QZ, \tag{2.1}$$

where P_B is the back pressure set by the feeding mechanism, Q is the flow rate of the working liquid, and Z is the hydraulic impedance. The QZ term represents the pressure loss of the propellant as it travels from the reservoir to the emitter. In capillary geometries, P_B is often prescribed using active control systems and is set such that the meniscus is fastened, preventing the potential loss of excess propellant. When no external field is applied, this is accomplished by balancing ΔP with the capillary pressure,

$$P_c = \frac{2\gamma}{r_c}, \tag{2.2}$$

where γ is the surface tension coefficient of the working liquid, and r_c is the internal radius of the capillary tube.

In ILIS electrosprays that utilize porous configurations, a passive flow control mechanism is implemented and the back pressure P_B is instead determined statically. Assuming operation in vacuum, P_B for ILISs is equal to the Laplace pressure,

$$P_B = -\frac{4\gamma}{D_R}, \tag{2.3}$$

where D_R is the reservoir pore size. As a result, ΔP is enforced via the design of porous emitters and reservoirs, where varying the pore size distribution has been shown to influence both emission mode and stability [32].

To understand how the Taylor cone structure depicted in Fig. 2.1b emerges with the introduction of an applied potential gradient, we consider the balance between capillary and electrostatic stresses at the fluid-dielectric interface,

$$\gamma \nabla \cdot \hat{\mathbf{n}} - \frac{1}{2}\epsilon_0 (E_n)^2 = \Delta P, \tag{2.4}$$

where $\hat{\mathbf{n}}$ is the unit vector normal to the interface directed toward the dielectric medium, ϵ_0 is the vacuum permittivity, and E_n is the electric field component normal to the meniscus. The first term on the left hand side of Eqn. (2.4) is the surface tension pressure and is a function

of the interfacial curvature, $\nabla \cdot \hat{\mathbf{n}}$, while the second term is the surface traction applied from the electric field. The difference of these terms is equal to the aforementioned interfacial pressure jump, ΔP. We initially study the case where $\Delta P = 0$, in alignment with Taylor's classical analysis [121], seeking a solution that satisfies Eqn. (2.4) and is independent of the feeding mechanism used. Rearranging the terms of Eqn. (2.4) results in an equation that describes how the normal field component on the cone changes with respect to the surface curvature,

$$E_n = \sqrt{\frac{2\gamma}{\epsilon_0} \nabla \cdot \hat{\mathbf{n}}}. \tag{2.5}$$

Next, Eqn. (2.5) is parameterized using a spherical coordinate system, where the origin is placed at the cone apex as shown in Fig. 2.1b. From the Young-Laplace equation, the interfacial curvature $\nabla \cdot \hat{\mathbf{n}}$ is equal to $(R_1^{-1} + R_2^{-1})$, where R_1^{-1} and R_2^{-1} are the principal radii of curvature. For a cone, these would correspond to the curvatures acting normal and tangential to the surface, where the latter orientation is equivalent to r. Along the cone generator (i.e., r-direction), the curvature is zero and the remaining normal curvature is henceforth denoted as $1/R_n$. Expressing R_n as a function of r and θ is possible using Meusnier's theorem [5] from differential geometry, which states that the curvature of a circle C_n with radius R_n passing through some point P is equivalent to the the curvature of another circle C also passing through P, provided that both circles share the same tangent line at P. This is visualized in Fig. 2.2, where a hypothetical force acting in the $\hat{n}$ direction is shown with curvature $1/R_n$. Below, an additional circle orthogonal to the center axis, C_b, is shown with curvature $1/R_b$. If the circles defined by R_n and R_b meet at the same point along r, then the curvature $1/R_n$ can be expressed as a function of R_b through the trigonometric relation,

$$\frac{1}{R_n} = \frac{\cos\theta}{R_b}. \tag{2.6}$$

R_b itself can be expressed using spherical coordinates via $R_b = r\sin\theta$. Substituting this

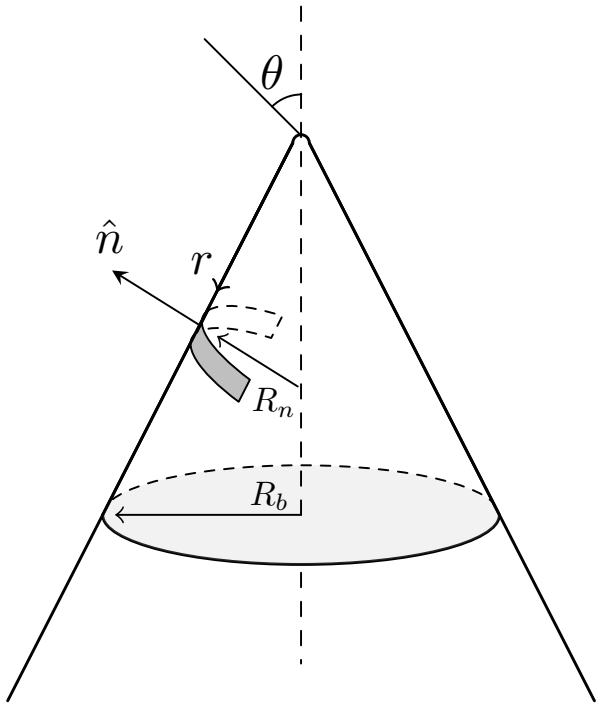

Figure 2.2: Schematic of Meusnier's theorem relating the normal curvature along a cone with spherical coordinates r and θ.

relation into Eqn. (2.6) yields the equation for the normal curvature as a function of the spherical system,

$$\nabla \cdot \hat{\mathbf{n}} = \frac{\cos\theta}{r\sin\theta} = \frac{\cot\theta}{r}. \tag{2.7}$$

Substituting Eqn. (2.7) into Eqn. (2.5) returns an updated equation describing how the normal field evolves in the coordinate system of interest,

$$E_n = \sqrt{\frac{2\gamma\cot\theta}{\epsilon_0 r}}. \tag{2.8}$$

Equation 2.8 can then be paired with Laplace's equation, $\nabla^2\phi = 0$, to formulate a boundary value problem whose solution describes the equipotential surface of Taylor cones. Laplace's equation in spherical coordinates with azimuthal symmetry takes the form

$$\frac{\partial}{\partial r}\left(r^2\frac{\partial\phi}{\partial r}\right)+\frac{1}{\sin\theta}\frac{\partial}{\partial\theta}\left(\sin\theta\frac{\partial\phi}{\partial\theta}\right)=0, \tag{2.9}$$

where it should be noted the internal potential domain is outside of the cone as shown in Fig. 2.1b. Applying separation of variables on Eqn. (2.9) results in Legendre's equation whose general solution is

$$\phi(r,\theta)=\sum_{n=0}^{\infty}A_n r^n P_n(\cos\theta)+\sum_{n=0}^{\infty}B_n r^{-(n+1)}P_n(\cos\theta), \tag{2.10}$$

where P_n is the Legendre function of the first kind. While the Legendre function of the second kind, Q_n, is also a solution of Eqn. (2.10), its singularity at $\theta = 0$ precludes its physical viability. The coefficients A_n and B_n are found by applying Eqn. (2.8) as a Neumann condition for fixed Taylor cone angle θ_{tc},

$$\begin{aligned} E_n = E_\theta = -\frac{1}{r}\frac{\partial\phi}{\partial\theta} &= -\sum_{n}^{\infty}\left(A_n r^{n-1}+B_n r^{-(n+2)}\right)\frac{d}{d\theta}P_n(\cos\theta) \\ &= \sqrt{\frac{2\gamma\cot\theta_{tc}}{\epsilon_0 r}} \end{aligned} \tag{2.11}$$

Equation 2.11 is valid solely at $n = 1/2$, where $B_{1/2} = 0$ and $A_{1/2}$ is a constant. Thus, our updated potential field is

$$\phi(r,\theta)=A_{1/2}r^{1/2}P_{1/2}(\cos\theta). \tag{2.12}$$

Nontrivial equipotential solutions of Eqn. (2.12) require that $P_{1/2}(\cos\theta) = 0$. This Legendre function is plotted against θ and presented in Fig. 2.3, where it can be seen the root corresponds with a Taylor cone half-angle of

$$\theta_{tc}=180^\circ-130.71^\circ=49.29^\circ. \tag{2.13}$$

Taylor's famous result in Eqn. (2.13) offers several important takeaways. The most remarkable of which is that his solution is not dependent on any properties of the conductive liquid nor the voltage of the extracting electrode, suggesting that Eqn. (2.13) is a universal

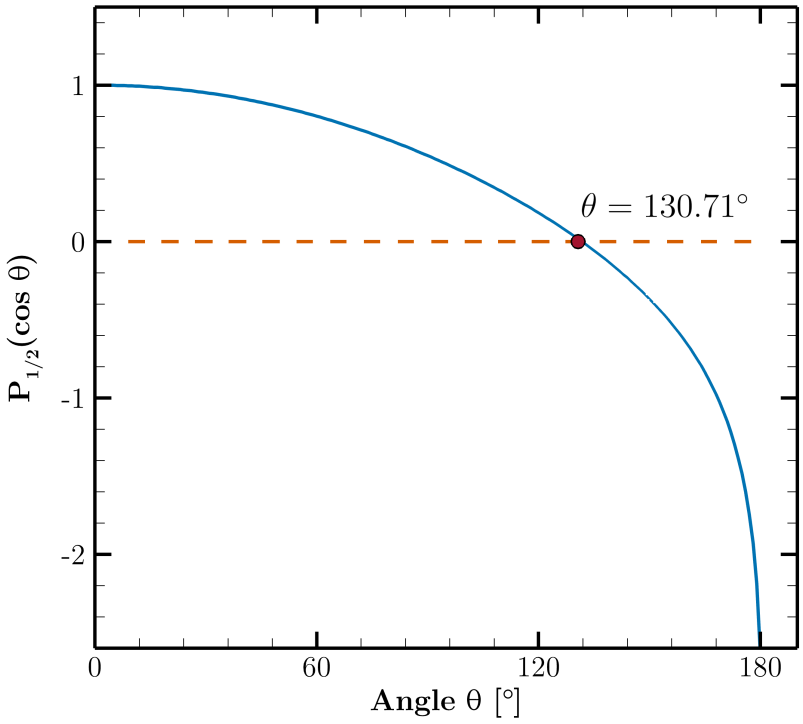

Figure 2.3: Legendre function of the first kind P_n of degree $n = 1/2$ versus spherical coordinate θ.

phenomenon. This fact has been experimentally verified [121], provided that space charge effects are not significant and the geometric configuration enables Eqn. (2.12) as a valid potential distribution.

Additionally, the potential solution at the interface Eqn. (2.12) is valid local to the cone and, once established, is resilient to far-field perturbations of the electric field. This suggests that the near-cone potential is governed by the local force balance of Eqn. (2.5). Nevertheless, it should be expected that this idealized morphology may not hold when other forces are introduced into the stress balance, such as an interfacial pressure gradient originating from a feeding mechanism denoted in Eqn. (2.4) or during emission at the apex. Such perturbations have been shown to influence the cone morphology [42]. Another disparity between ideal and observed Taylor cone structures can be seen in the normal field distribution of Eqn. (2.8),

where $E_n \propto 1/\sqrt{r}$ and thus $E_n \to \infty$ as $r \to 0$. This suggests that in the idealized structure, the electric field becomes unbounded at the apex as it is applied over an infinitesimally small region. Of course, this is not physically feasible in reality. When increasingly stronger fields at the apex can no longer be supported by the liquid surface tension, the cone morphology is locally broken and one of several possible emission modes emerge that each carry their own unique characteristics. Their incipience is a function of both operating conditions and properties of the working fluid and is described further in the subsequent section.

2.2 Cone-Jet and Mixed Emission Modes

Emission from Taylor cones have been studied and classified across a wide range of operational and geometric regimes [25–28, 35, 44, 45, 58, 60, 61]. The regime of particular interest to ILIS electrosprays is the purely ionic emission mode, where high localized field strengths yield the direct evaporation of ions from the meniscus. To understand the physical basis from which this occurs, we begin first with analysis of the simplest and most studied emission regime, the steady cone-jet. A schematic of each emission regime, including the aforementioned and the intermediate mixed mode, is presented in Fig. 2.4.

Cone-jets, as the name implies, are characterized by the continuous formation of a liquid jet that is expelled from the cone apex, eventually breaking down into the formation of electrically charged droplets. The jet and the cone can be studied separately when the former's length scale is considerably smaller than that of the meniscus, a condition that is met with highly conductive working fluids in the range of 0.001–1 S/m. In this case, the cone can be largely treated as an infinitely conductive, hydrostatic structure. However, the liquid emission at the apex precludes the same assumption to be made in this region, known as the cone-jet transition region, r^*_{cj}. The presence of hydrodynamics near r^*_{cj} indicates that equipotentiality is no longer adhered to. This occurs when the time scale of the liquid passage, ${r^*_{cj}}^3/Q$, where Q is the jet flow rate, is of comparable order to the charge relaxation time, $\epsilon\epsilon_0/K$, where ϵ is the relative permittivity of the liquid and K is the conductivity. This

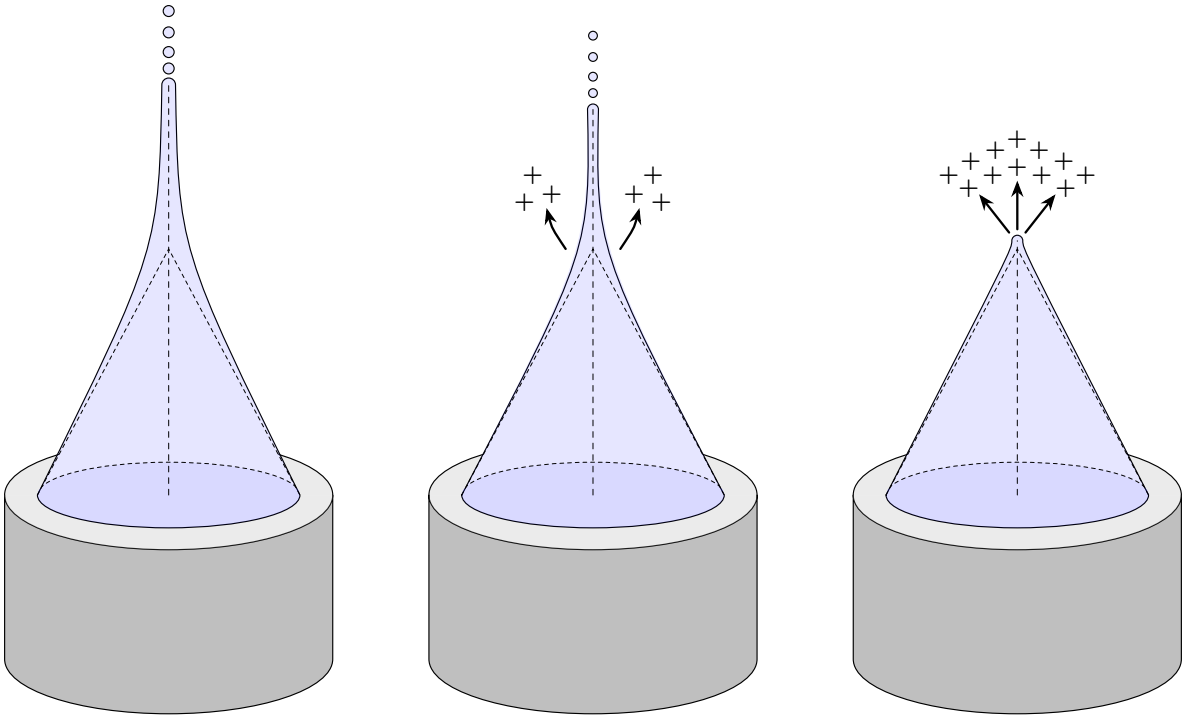

Figure 2.4: Schematic of electrospray emission modes: (a) cone-jet consisting of an elongated jet protruding from the cone apex that breaks into droplets, (b) mixed cone-jet where reducing the flow rate acts to reduce the jet and introduce field evaporation of ions at the cone-to-jet transition region, and (c) purely ionic emission where further reduction of the flow rate completely suppresses the jet and emission consists solely of ions evaporating from a closed meniscus.

condition enables us to quantify the characteristic length scale of the cone-jet transition region,

$$r_{cj}^{*} = \left(\frac{\epsilon \epsilon_0 Q}{K} \right)^{1/3} . \tag{2.14}$$

What Eqn. (2.14) demonstrates, and what will be continually demonstrated throughout this dissertation's analytical analysis of electrosprays, is that scaling laws are the fundamental tool used to understand the order of magnitude of governing phenomena across each emission mode. Continuing the analysis, the assumptions used to derive Eqn. (2.14) can also be used

to derive the approximate emission current transported by cone-jet electrosprays. Near r^*_{cj}, it can be assumed that the majority of charge transport will be convected by the jet while the surface is simultaneously relaxed, i.e. the surface charge distribution arises in response largely to the normal electric field component, E_θ. Given the system geometry, the cone-jet emission current I_{cj} obeys

$$I_{cj} = 2\pi(r^*_{cj}\sin\theta_{tc})\,\sigma u_{cj}, \tag{2.15}$$

where σ is the surface charge distribution and u_{cj} is the liquid velocity. From Eqn. (2.8), the surface charge can be shown to equate to

$$\sigma = \epsilon_0 E_n = \epsilon_0 E_\theta = \epsilon_0\sqrt{\frac{2\gamma\cot\theta_{tc}}{\epsilon_0 r}}. \tag{2.16}$$

Similarly, the liquid velocity can be shown to follow

$$u_{cj} = \frac{Q}{2\pi(1-\cos\theta_{tc}){r^*_{cj}}^2}. \tag{2.17}$$

Using Eqns. (2.16) and (2.17), Eqn. (2.15) can be rewritten as

$$I_{cj} \approx \frac{\sqrt{2\cos\theta_{tc}\sin\theta_{tc}}}{1-\cos\theta_{tc}}\sqrt{\frac{\gamma K Q}{\epsilon}}, \tag{2.18}$$

where the constant coefficient of Eqn. (2.18) is approximately 2.86. The emission behavior suggested by Eqn. (2.18) has been experimentally validated [60, 96, 103] where the constant coefficient of Eqn. (2.18) is replaced by an empirical factor $f(\epsilon)$. Similar to the universal Taylor cone angle of Eqn. (2.13), Eqn. (2.18) is remarkable in that it suggests the cone-jet current is independent of the applied voltage, electrode geometry, and fluid viscosity.

Downstream from the cone-jet transition region, the axially extending jet is characterized by its diameter, which has also been shown to approach [96]

$$d_{cj} = g(\epsilon)\left(\frac{\epsilon\epsilon_0 Q}{K}\right)^{1/3}, \tag{2.19}$$

where $g(\epsilon)$ is another empirical factor related to $f(\epsilon)$ and is also a function of the liquid relative permittivity. Once at the limit prescribed by d_{cj}, the jet breaks down into a stream of charged droplets. Although the balance between surface tension and the normal field is broken at the cone-jet transition region, it is reasonable to postulate that this equilibrium condition is still generally valid downstream within the jet and droplet emergence regions as $E_\theta \gg E_r$. This enables the stress balance of Eqn. (2.4) to be repeated in the context of an emitted droplet,

$$\frac{2\gamma}{R_d} = \frac{1}{2}\epsilon_0 (E_n)^2, \tag{2.20}$$

where R_d is the droplet radius. Assuming a spherical droplet with a relaxed surface charge,

$$\sigma_d = q_d / 4\pi R_d^2 = \epsilon_0 E_n \qquad \rightarrow \qquad E_n = \frac{q_d}{4\pi\epsilon_0 R_d^2}, \tag{2.21}$$

where σ_d is the droplet surface charge and q_d is the total charge within the droplet. Substituting the right-most equation of Eqn. (2.21) into Eqn. (2.20) enables calculation of the maximum charge $q_{d,max}$ a droplet can support before instability

$$q_{d,max} = 8\pi\sqrt{\epsilon_0 \gamma}\, R_d^{3/2}. \tag{2.22}$$

Equation (2.22) is known as the Rayleigh limit [43] at which the addition of further charge or, more commonly expected in cone-jet emission, perturbations in the morphology results in an instability that fragments the initial droplet into smaller, spheroidal droplets. Normalizing the Rayleigh limit charge with the droplet mass $m_d = 4/3\pi R_d^3 \rho$, where ρ is the liquid mass density, results in a maximum charge-to-mass ratio of

$$\left(\frac{q}{m}\right)_{cj,max} = \frac{6\sqrt{\epsilon_0 \gamma}}{\rho R_d^{3/2}}. \tag{2.23}$$

Maximizing the charge-to-mass ratio, or specific charge, is critical in the context of electrospray micropropulsion as it is directly proportional to the exhaust velocity (and thus specific impulse

I_{sp}) through the relation

$$I_{sp} = \frac{1}{g}\sqrt{2V_a\left(\frac{q}{m}\right)}, \tag{2.24}$$

where g is the acceleration due to gravity, and V_a is the accelerating potential. Equation (2.24) indicates that increasing the specific charge results in a thruster that more efficiently utilizes its propellant to change the momentum of its spacecraft. Equivalently, increasing the specific charge reduces the acceleration potential required for a targeted specific impulse.

In practice, droplets emitted from steady cone-jets do not exhibit specific charges near the maximum specified by Eqn. (2.23) due to their proclivity to fragment. Jets with characteristic lengths d_{cj} have been observed [35] to emit droplets with specific charges that follow

$$\left(\frac{q}{m}\right)_{cj} = \frac{f(\epsilon)}{\rho}\sqrt{\frac{\gamma K}{Q}}, \tag{2.25}$$

which is distinct from Eqn. (2.23) through its dependency on the liquid conductivity K and flow rate Q. As such, Eqn. (2.25) is a function of different fluids and flow conditions but is typically within the range of $10^2 - 10^4$ C/kg.

Equations (2.24) and (2.25) together suggest that the cone-jet specific impulse is proportional to the ratio of the liquid conductivity to its flow rate, $I_{sp} \propto (K/Q)^{1/4}$. Simultaneously, increasing this relation acts to reduce the jet thickness d_{cj} as stated by Eqn. (2.19) ($d_{cj} \propto (K/Q)^{-1/3}$). Therefore, in principle, a high specific charge can be achieved for a given working liquid by continually decreasing the flow rate Q, albeit at the cost of current shown by Eqn. (2.18). In practice, the validity of this relationship is limited by the emergence of one of several phenomena.

The first of these phenomena include instabilities in the Taylor cone morphology that arise when a non-dimensional flow parameter η, given by

$$\eta = \sqrt{\frac{\rho K Q}{\gamma \epsilon \epsilon_0}}, \tag{2.26}$$

drops below some critical threshold. For traditional capillary geometries, the minimum value of η before instabilities arise is on the order of 0.5 [22, 50]. The underlying nature of this instability is still not well understood, although it is postulated that the specific charge cannot exceed the theoretical limit defined by the full dissociation of anions and cations in the working fluid [96].

The second of these phenomena is observed when the flow rate itself is lowered below a critical value, approximately when the jet thickness is on the order of 10^{-8} m. In this regime, the decreasing current is compensated for by the prevalence of a process known as ion or field evaporation. This evaporation process, where ions—often solvated such that one or several neutral molecules are attached to it—directly emit from the liquid surface, is mostly concentrated near the cone-jet transition region where the normal field E_θ is at its maximum. This operational regime defines the mixed droplet-ion emission mode, first discovered by Gamero-Castaño and Fernández de la Mora [49], and is visualized in Fig. 2.4b. This regime is of interest in the context of micropropulsion as the emitted mass is largely carried by droplets while a significant portion of the current is carried by ions, providing a balance between thrust and specific impulse unavailable in other emission modes.

2.3 Purely Ionic Regime

Continued reduction of the flow rate acts to simultaneously reduce the droplet emission while increasing the ion emission. While initially this results in a decrease of total current, a greater efficiency in charge transport by the ions eventually contributes to an overall increase in total emitted current. It should be expected then that an operational regime exists such that the jet is suppressed completely and the total charge is carried solely by ions evaporating from a closed meniscus. This emission mode exists under select conditions and is known as

the purely ionic regime, visualized in Fig. 2.4c.

2.3.1 Ionic Liquids

Purely ionic emission is not a universal operational regime and is enabled when the working propellant is an ionic liquid, defined as a chemical salt whose state is liquid at ambient conditions. In certain contexts, a stricter definition is used where the salt must have a melting point below 100°C [73]. This regime has yet to be observed using organic electrolytes, the other dominant branch of electrospray propellants, as they exhibit a minimum stable flow rate Q^{oe}_{min} of approximately

$$Q^{oe}_{min} \approx \frac{\epsilon\epsilon_0\gamma}{\rho K}, \tag{2.27}$$

although recent research has suggested that this minimum is also dependent on viscous phenomena [51]. Regardless, Q^{oe}_{min} is often much larger than what would be required to support pure ionic emission as these propellants succumb to the instabilities discussed in Section 2.2.

Several properties of ionic liquids distinguish them from standard electrolytes and thus enable their ability to support closed meniscus emission. Firstly, ionic liquids do not consist of any solvent which result in stronger Coulombic interparticle forces relative to Van der Waals forces that govern electrolytes. Despite these larger attractive forces, ionic liquids resist forming crystalline structures under ambient conditions and remain in a liquid state due to a unique combination of structural and energetic properties of the ions involved. These ions are usually large and asymmetrical, precluding them from efficiently packing into solid lattices and delocalizing their charge over a greater volume. As a result, ionic liquids exhibit low lattice energies that are overcome by their thermal energy at room temperature.

Secondly, ionic liquids often exhibit a wider electrochemical window, defined as the range of voltages over which a substance remains stable before undergoing significant electrochemical

decomposition. For many electrolytes the window is on the order of 1 V while ionic liquids can achieve windows on the order of 4-5 V. This broader operational range contributes to the ability of an ionic liquid to support a closed meniscus experiencing high local field strengths.

2.3.2 Emission Mechanics

The field evaporation of ions from the surface of a conductive fluid was first described by Iribarne and Thomson [66] and subsequently characterized [49, 78]. Initially, the exploration of an emission regime that consists predominantly of ions focused on systems where liquid metals were utilized as the working fluid [46, 130]. These are known as liquid metal ion sources (LMIS) and have conductivities that are significantly higher than standard electrospray ion sources. As a result, the effects of charge relaxation are not present and the electric field strength at the apex cannot be externally determined by the extractor electrode potential. The observation of pure ionic emission on a closed meniscus using ionic liquids is due to, in combination with the reasons mentioned in the aforementioned section, their high conductivities and high surface tensions. The lack of a jet allows ion evaporation to be modeled analogously to thermionic emission, as an activated process whose mathematical form is that of a modified Arrhenius equation [65],

$$\mathbf{j} \cdot \hat{\mathbf{n}} = \frac{\sigma k_b T}{h} \exp\left(\frac{-E_a}{k_b T}\right), \tag{2.28}$$

where $\mathbf{j}$ is the evaporated current density vector, σ is the surface charge density at the interface, T is the temperature of the working fluid, k_b is Boltzmann's constant, h is Planck's constant, and E_a is the activation energy. For many ionic liquids E_a is on the order of 1-2 eV [57] meaning that, in the absence of an externally applied field, significant ion emission would not occur unless the temperature T was on the order of 1,000 degrees Kelvin. Inducing ion emission thermally would require additional heating and load management subsystems, as well as likely introduce scaling related inefficiencies observed in other EP devices where high

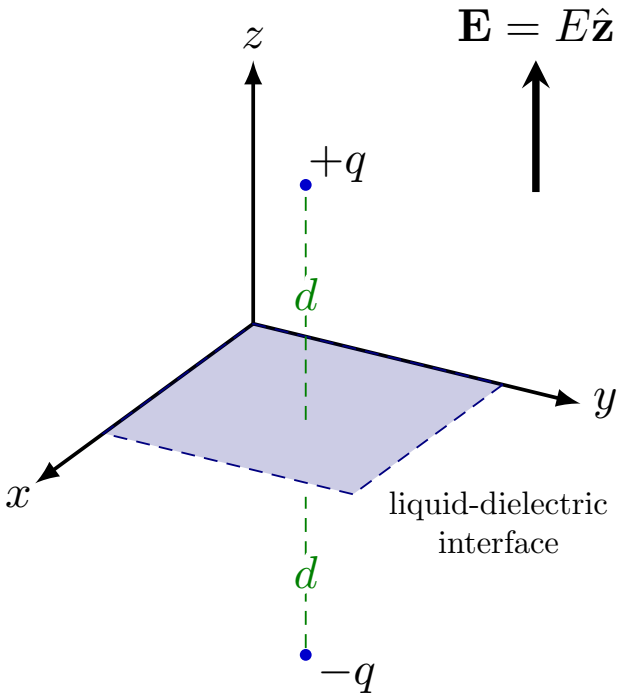

Figure 2.5: Schematic of evaporated ion q and hypothetical mirror charge $-q$, both a fixed distance d away from the liquid-dielectric interface. The method of image charges is used to determine the reduction in free energy of solvation $G(E)$ required to enable the field emission process in ionic liquids.

temperatures are required for ionization. Instead, and more simply, an externally applied electric field can be used to reduce this energy barrier.

Determining the value of E_a can be accomplished using the method of image charges [54], visualized on Fig. 2.5. An ion of charge q is shown at some fixed distance d away from the liquid-dielectric interface defined at the $x-y$ plane. It is assumed the length scale is sufficiently small such that the interfacial area shown has no curvature and is approximated as a flat plane. Relative to the interface, the ion q experiences a repulsive force due to the applied field equal to $F_E = qE$ and an attractive force from induced charge within the conductive liquid. The method of image charges states that this attractive force is equal to the force due to a hypothetical charge of opposite polarity $-q$ located at $z = -d$. From electrostatic theory this force is equal to $F_I = -q^2/4\pi\epsilon_0(2d)^2$. The total energy of the system

is determined by calculating the work W required to bring q from $z = \infty$ to $z = d$,

$$W(d) = \int_{\infty}^{d} F_E \, dz + \int_{\infty}^{d} F_I \, dz = \int_{\infty}^{d} qE \, dz - \int_{\infty}^{d} \frac{q^2}{4\pi\epsilon_0(2z)^2} \, dz. \tag{2.29}$$

It can be assumed that $E = 0$ at $z = \infty$, resulting in an energy of

$$W(d) = qEd + \frac{q^2}{16\pi\epsilon_0 d}. \tag{2.30}$$

When no external field is applied it can be shown that the derivative of Eqn. (2.30) is negative, indicating that ion q would always experience an attractive force towards the ionic liquid. Introducing the linear qEd term changes the gradient distribution, allowing q to experience a net repulsive force at distance d if the field strength E is sufficiently high. The minimum distance d_{min} at which this force balance occurs is the distance that equates F_I and F_E,

$$d_{min} = \sqrt{\frac{q}{16\pi\epsilon_0 E}}. \tag{2.31}$$

Substituting Eqn. (2.31) into Eqn. (2.30) yields the reduction in free energy of solvation $G(E)$ when applying a field of strength E,

$$W(d_{min}) \equiv G(E) = \sqrt{\frac{q^3 E}{4\pi\epsilon_0}}. \tag{2.32}$$

However, this is not equal to the activation energy E_a as $G(E)$ does not account for the initial energy barrier of the ion in the absence of an external field. In that case, we assume the ion q initially exists at some minimum distance d_i on the order of the ion length scale. This is known as the ion solvation energy ΔG [56] and is an experimentally determined value for W at $d = d_i$. The activation energy E_a is then equal to the difference between initial energy barrier ΔG and the energy reduction by the external field E,

$$E_a = \Delta G - G(E) \tag{2.33}$$

Using Eqns. (2.32) and (2.33), it can be shown that the minimum normal electric strength E_{min} required for significant ion emission must satisfy

$$E_{min} \geq \frac{4\pi\epsilon_0}{q^3}\Delta G^2, \tag{2.34}$$

which for standard ionic liquids is on the order of 10^9 V/m [48]. This exceeding high strength is only possible near the Taylor cone apex at length scales on the order of nanometers. This defines the emission regime and its value, alongside other regimes of interest during pure ionic emission, are obtained using scaling laws further described in the subsequent section.

2.3.3 Scaling Laws

Approximation of the length scale of emission r^* can be accomplished by revisiting the interfacial stress balance of Eqn. (2.4) in the context of an ionic liquid meniscus undergoing pure ionic emission. Firstly, we know from Eqn. (2.34) that the critical normal field for significant ion emission is $E^* \approx E_{min}$. Next, the interfacial pressure jump is again neglected and the electric traction $\mathbf{T}^e$ is obtained via application of the unmagnetized Maxwell stress tensor [70]

$$\mathbf{T}^e = \frac{1}{2}\epsilon_0 \left(E^2 - \epsilon {E^l}^2 + (\epsilon - 1){E_t}^2 \right) = \frac{2\gamma}{r^*}, \tag{2.35}$$

where E^l is the normal electric field within the liquid and E_t is the tangential component of the electric field in the external dielectric domain. From the geometry it is expected that $E_t \to 0$ as $r \to 0$. An electric field within the ionic liquid E^l is expected initially in response to the external field E^* assuming full charge relaxation has yet to occur on the interface. To approximate the liquid electric field component, an Ohmic conduction model is assumed

$$j^l = KE^l, \tag{2.36}$$

where j^l is the current density normal to the interface within the liquid, in conjunction with a surface charge obtained from the interfacial jump condition

$$\sigma = \epsilon_0 E - \epsilon_0 \epsilon E^l. \tag{2.37}$$

Substituting Eqns. (2.36) and (2.37) into the ion evaporation law of Eqn. (2.28) allows one to solve for the normal liquid electric field component,

$$E^l = \frac{E/\epsilon}{1 + \tau \exp\left(\frac{1}{k_B T}\left[\Delta G - G(E)\right]\right)}, \tag{2.38}$$

where τ is a non-dimensional time scale and is equal to

$$\tau = \frac{hK}{\epsilon \epsilon_0 k_B T}. \tag{2.39}$$

τ in Eqn. (2.39) denotes the ratio of the time scale for charge emission with the time scale for charge relaxation. For typical ionic liquids at room temperature, where $K \approx 1$ S/m and $\epsilon \approx 10$, $\tau \ll 1$. At external fields near critical emission strengths E^*, the liquid normal field strength is approximately $E^l \approx E^*/\epsilon$. Substituting this approximation into Eqn. (2.35) allows one to solve for the characteristic length scale at which significant ion emission is expected,

$$r^* \approx \left(\frac{\epsilon}{\epsilon - 1}\right) \frac{4\gamma}{\epsilon_0 E^{*2}} = \left(\frac{\epsilon}{\epsilon - 1}\right) \frac{q^6 \gamma}{4\pi^2 \epsilon_0^3 (\Delta G)^4}. \tag{2.40}$$

Equation (2.40) can also be used to determine the characteristic emission current I^*, assuming the evaporation surface morphology is a spherical cap of radius r^*. It should be expected that the characteristic emission scaling obeys $I^* \sim A_e j^l$, where A_e is the emission area whose scaling follows $A_e \sim \pi r^{*2}$. Expressed in terms of the critical field and properties of the liquid, the characteristic emitted current is approximately

$$I^* \approx \frac{\epsilon}{(\epsilon - 1)^2} \frac{32\pi K \gamma^2}{\epsilon_0^2 E^{*3}} = \frac{\epsilon}{(\epsilon - 1)^2} \frac{q^9 K \gamma^2}{2\pi^2 \epsilon_0^5 (\Delta G)^6}. \tag{2.41}$$

It should be noted that both Eqns. (2.40) and (2.41) demonstrate strong sensitivities to the solvation energy ΔG. For an ionic liquid where $K = 1$ S/m, $\gamma = 0.05$ N/m, $\epsilon = 10$, $\Delta G = 1$ eV, the emitting radius would be approximately $r^* \approx 52$ nm with a total current of $I^* \approx 1000$ nA. Using an ionic liquid with a solvation energy of $\Delta G = 1.5$ eV instead would result in an emission radius and current of 10 nm and 1000 nA, respectively. This range of currents is comparable to what is experimentally observed in ionic liquids with similar characteristics [56, 107].

2.4 Summary

This chapter examined the governing physics of electrospray emission, providing a framework for understanding the mechanisms underlying Taylor cones, emission regimes, and the scaling laws that dictate their behavior. Beginning with the classical formation of Taylor cones, the analysis demonstrated this phenomenon originates from the balance between surface tension, capillary forces, and electrostatic stresses at the liquid-dielectric interface. Subsequently, the universal Taylor cone angle was derived and noted for its independence from specific fluid properties or geometric constraints under idealized conditions.

Subsequent sections explored emission regimes, with particular attention to the steady cone-jet mode and the transition to purely ionic emission. For cone-jet operation, scaling laws for the cone-jet transition region, emission current, and jet diameter revealed the dependence of these phenomena on key liquid properties, including conductivity, surface tension, and flow rate. These relationships offer insight into the trade-offs between stability, thrust, and specific charge in electrospray propulsion systems.

Reduction of the flow rate in a cone-jet enables the purely ionic regime when ionic liquids are used as the working fluid. The analysis of this emission mode included the derivation of a critical electric field for ion evaporation and the use of scaling laws to approximate emission radius and current. The results reinforce the unique suitability of ionic liquids for

ILIS applications, where their high surface tension and conductivity, combined with low solvation energies, enable emission at length scales and field strengths unattainable with traditional electrolytes.

These theoretical insights form the foundation for the numerical models derived in subsequent chapters. The equations and scaling relationships developed here provide the necessary constraints and boundary conditions for the implemented computational methods, ensuring that the models developed accurately capture the physical phenomena governing electrospray ionic emission.

Chapter 3

Electrohydrodynamic Meniscus Model

This chapter presents a physics-based model of an electrohydrodynamic (EHD) meniscus undergoing steady-state ionic emission, designed to capture the multiscale phenomena inherent in field emission from an ionic liquid under the diverse geometric and operational conditions typical of electrospray thruster operation. As discussed in Chapter 2, the physical processes governing this system span several spatial orders of magnitude—from the nanometer-scale emission dynamics to the micron-scale meniscus geometry to the macroscopic electrical and fluid dynamic fields—requiring a multiscale modeling approach. The EHD meniscus model integrates the Taylor–Melcher leaky dielectric framework with a phenomenological ion evaporation law to describe the current density distribution and the resulting ion emission at the liquid–vacuum interface. This interfacial balance accounts for the electrostatics from externally applied electric fields and the fluid mechanics of the conductive working liquid. The former phenomenon is modeled using Laplace's equation while the latter is captured via the incompressible Navier–Stokes equations in the low–Reynolds number regime, ensuring that viscous stresses and capillary forces are appropriately balanced at the meniscus.

The numerical implementation of this model employs a two-phase finite element framework, partitioning the physical domain into two computational subdomains whose intersection defines the EHD meniscus. To resolve the coupled Laplace and Stokes problems in the bulk domains, the chapter details a global algorithm that enforces the interfacial boundary conditions for a given meniscus morphology and iteratively perturbs the interfacial shape until

a steady-state configuration is found. Particular emphasis is given to the challenges of mesh deformation and numerical stability, which are addressed using interfacial perturbation techniques and a stability analysis of the implemented framework.

The chapter is organized as follows. In Section 3.1, the computational domain is defined, including detailed descriptions of both the macroscopic emitter configuration and the sub-scale region surrounding the meniscus. Section 3.2 develops the theoretical model formulation, presenting the governing equations for electrostatics, fluid dynamics, and interfacial stress balance. Section 3.3 outlines the numerical implementation strategy, detailing the finite element discretization, global coupling algorithm, and methods for handling interfacial perturbations and internal mesh deformation. In Section 3.4, simulation results are presented and compared with established literature, highlighting both the strengths and limitations of the implemented approach.

3.1 Computational Domain

The computational domain implemented in this work is similar to that in [105], and is presented in Fig. 3.1. The global domain, shown in Fig. 3.1a, includes a single two-dimensional emitter affixed to a flat plate, denoted by Γ_{emi}. The radius of the emitter tip is $x_{emi} = 25$ μm and the distance from the emitter center to the domain boundary is $x_{dom} = 150$ μm. The emitter profile is a function of the equation

$$y(x) = \eta_0 \sqrt{\frac{a^2}{4} + \frac{x^2}{1 - \eta_0^2}}, \tag{3.1}$$

where a is the linear eccentricity of the hyperbola and η_0 is a non-dimensional parameter governing the profile's asymptote. The linear eccentricity is given by

$$a = 2d_{emi} \sqrt{1 + \frac{r_c}{d_{emi}}}, \tag{3.2}$$

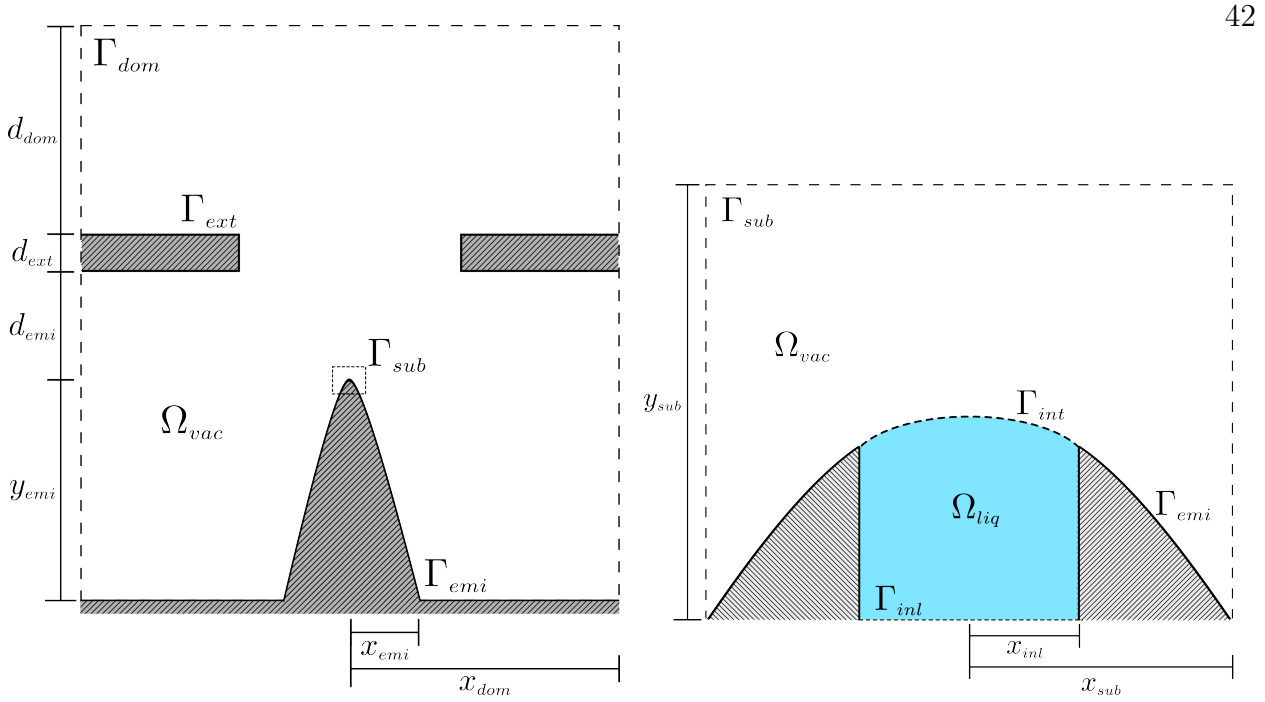

(a) Macro-scale, two-dimensional domain of a single emitter tip below two extractor electrodes. A voltage differential is applied between the emitter and electrodes to induce electric fields strengths on the order required for direct ion evaporation at the propellant free surface. Field emission at the interface is numerically treated within a separate sub-scale domain at the emitter apex, and is coupled to the macro-scale domain via the Γ_{sub} intersection

(b) Sub-scale domain of an emission site at the emitter apex presented in Fig. 3.1a. Steady, open channel flow is assumed for the propellant in Ω_{liq}, where a fully-developed velocity profile is imposed at the Γ_{inl} inlet boundary. Geometry of the EHD meniscus, Γ_{int}, is numerically perturbed to find configurations that satisfy mechanical equilibrium, a necessary prerequisite before solving steady-state emission characteristics

Figure 3.1: Computational domain of the EHD meniscus solver

where d_{emi} is the distance between the emitter apex and extractor electrode, and r_c is the radius of curvature at the emitter apex. The non-dimensional η_0 parameter is defined as

$$\eta_0 = \frac{1}{\sqrt{1 + r_c/d_{emi}}}, \tag{3.3}$$

where $r_c = 11$ µm and $d_{emi} = 100$ µm. The extractor electrode thickness is $d_{ext} = 25$ µm, the distance from the extractor electrodes to the domain ceiling is $d_{dom} = 100$ µm, and the distance from the emitter base to the tip is $y_{emi} = 200$ µm.

Within the subscale domain at the emitter apex, shown in Fig. 3.1b, an open fluid channel of radius $x_{inl} = 20$ nm is formulated at the tip center to account for upstream conditions contributing to ion emission at the EHD meniscus, Γ_{int}. A fully developed velocity profile is assumed at the channel inlet Γ_{inl}, as well as a channel length sufficiently longer than the meniscus length. The centerline distance of the subscale domain is $x_{sub} = 100$ nm, with a height of $y_{sub} = 100$ nm.

3.2 Model Formulation

The EHD meniscus model solves for current density across a steady–state free surface undergoing field emission. It accomplishes this by solving the EHD conditions in the liquid and vacuum domains Ω_{liq} and Ω_{vac}, respectively. An iterative routine then perturbs the shape of the interface until an equilibrium solution has converged.

We begin by considering the electrostatic conditions that govern the two-phase system in Fig. 3.1a. As the space charge surrounding the evaporating surface is negligible [63], no charge density is considered within the vacuum domain Ω_{vac}. Within the conductive bulk fluid, EHD phenomena are modeled using the Taylor–Melcher leaky dielectric model [110], where the volumetric charge is also considered negligible. Therefore, Laplace's equation is solved within each phase domain while enforcing continuity at their interface,

$$\nabla^2 \phi_l = 0 \qquad \text{in } \Omega_{liq}, \tag{3.4}$$

$$\nabla^2 \phi_v = 0 \qquad \text{in } \Omega_{vac}, \tag{3.5}$$

$$\phi_l = \phi_v \qquad \text{on } \Gamma_{int}, \tag{3.6}$$

where ϕ_l and ϕ_v are the liquid and vacuum electric potentials, respectively. A potential gradient is applied from the emitter Γ_{emi} and extractor electrodes Γ_{ext} such that

$$\phi_l = 0 \qquad \text{on } \Gamma_{emi} \cup \Gamma_{inl}, \tag{3.7}$$

$$\phi_v = V_0 \qquad \text{on } \Gamma_{ext}, \tag{3.8}$$

where V_0 is the voltage of the extractor electrodes. In the leaky dielectric model, poorly conducting liquids are described as dielectric materials with uniform, non–zero Ohmic conductivities. As a result, only conductive charge transport is considered and the current density obeys

$$\mathbf{j} = -K\nabla\phi_l \qquad \text{in } \Omega_{liq}, \tag{3.9}$$

where $\mathbf{j}$ is the current density, and K is the electrical conductivity. It should be noted that this system of charge transport implicitly enforces charge continuity $\nabla \cdot \mathbf{j} = 0$, in the bulk fluid, since the divergence of Eqn. (3.9) results in a scale factor of Eqn. (3.4). In the meniscus, a phenomenological kinetic law originally described by Iribarne [65] is used for the evaporated ion current,

$$\mathbf{j} \cdot \hat{\mathbf{n}} = \frac{\sigma k_b T}{h_c} \exp\left(\frac{-1}{k_b T}\left[\Delta G - \sqrt{\frac{-\nabla\phi_v \cdot \hat{\mathbf{n}}}{4\pi\varepsilon_0/q^3}}\right]\right) \qquad \text{on } \Gamma_{int}, \tag{3.10}$$

where $\hat{\mathbf{n}}$ is the unit vector normal to the interface, k_b is the Boltzmann constant, h_c is the Planck constant, T is the temperature, σ is the surface charge density at the interface, ΔG is the solvation energy of the evaporated ions, q is the elementary charge, and ε_0 is the vacuum permittivity.

Viscous stress contributions to the EHD meniscus are accounted for in part by incompressible Navier–Stokes equations at the low–Reynolds limit,

$$\mu\nabla^2\mathbf{u} - \nabla p = 0 \qquad \text{in } \Omega_{liq}, \tag{3.11}$$

$$\nabla \cdot \mathbf{u} = 0 \qquad \text{in } \Omega_{liq}, \tag{3.12}$$

where μ is the dynamic viscosity, $\mathbf{u}$ is the fluid velocity, and p is the pressure. Inertial effects are neglected due to an order–of–magnitude analysis by Higuera [63], where he demonstrated that viscous forces are dominant in this spatial regime. While Eqn. 3.12 enforces mass continuity in the bulk fluid, an additional condition at the interface is required to enforce mass conservation of evaporated ions,

$$\mathbf{u} \cdot \hat{\mathbf{n}} = \frac{m}{\rho q} \mathbf{j} \cdot \hat{\mathbf{n}} \qquad \text{on } \Gamma_{int}, \tag{3.13}$$

where m is mass of the evaporating species and ρ is fluid density. The interfacial pressure jump across the meniscus is given by

$$p_{int} = p_{res} - QZ \qquad \text{on } \Gamma_{int}, \tag{3.14}$$

where p_{int} is the interfacial pressure jump, p_{res} is the pressure at the propellant reservoir, Q is the inlet flow rate, and Z is the hydraulic impedance of the propellant. As vacuum conditions are assumed, $p_{res} = 0$ and the remaining equation is used to enforce a fully developed velocity profile at the inlet Γ_{inl}.

Another characteristic of the leaky dielectric model is how it modifies the interfacial conditions of dielectric materials. Instead of electric displacement continuity, a condition of interfacial current continuity is enforced. The inevitable jump in electric displacement from this modified condition is accounted for by an interfacial surface charge density distribution given by

$$(\varepsilon \nabla \phi_l - \nabla \phi_v) \cdot \hat{\mathbf{n}} = \frac{\sigma}{\varepsilon_0} \qquad \text{on } \Gamma_{int}, \tag{3.15}$$

where ε is the relative permittivity of the propellant. Surface charge continuity at the meniscus is enforced via a steady-state transport equation,

$$\mathbf{u} \cdot \nabla \sigma = (\sigma \hat{\mathbf{n}} \cdot \nabla \mathbf{u} - K \nabla \phi_l - \mathbf{j}) \cdot \hat{\mathbf{n}} \qquad \text{on } \Gamma_{int}. \tag{3.16}$$

Equation 3.16 describes the evolution of surface charge as a function of the rate charge is conducted to the surface and the rate charge is evaporated from the surface.

Finally, we consider the interfacial stress balance. When projected in the normal and tangential directions relative to the meniscus, it yields the form:

$$\hat{\mathbf{t}} \cdot (\mathbf{T}_l - \mathbf{T}_e) \cdot \hat{\mathbf{n}} = 0 \qquad \text{on } \Gamma_{int}, \tag{3.17}$$

$$\hat{\mathbf{n}} \cdot (\mathbf{T}_l - \mathbf{T}_e) \cdot \hat{\mathbf{n}} = -\gamma \nabla \cdot \hat{\mathbf{n}} \qquad \text{on } \Gamma_{int}, \tag{3.18}$$

where $\hat{\mathbf{t}}$ is the unit vector tangent to the interface, $\mathbf{T}_l$ is the Newtonian fluid stress tensor, $\mathbf{T}_e$ is the electrostatic Maxwell stress tensor, and γ is the surface tension coefficient.

3.2.1 Normal and Tangential Projections of Stress Tensors

Before Eqns. (3.17) and (3.18) can be enforced as interfacial boundary conditions, the liquid and electric stress tensor projections must be expressed as functions of the system variables so that they can be implemented within the solver. The normal and tangential projections of the interfacial Maxwell stress tensor are given by the leaky dielectric model [110]

$$\hat{\mathbf{t}} \cdot \mathbf{T}_e \cdot \hat{\mathbf{n}} = -\sigma \nabla \phi_v \cdot \hat{\mathbf{t}} \qquad \text{on } \Gamma_{int}, \tag{3.19}$$

$$\begin{aligned} \hat{\mathbf{n}} \cdot \mathbf{T}_e \cdot \hat{\mathbf{n}} = {} & \frac{1}{2}\varepsilon_0 \left((\nabla \phi_v \cdot \hat{\mathbf{n}})^2 - \varepsilon (\nabla \phi_l \cdot \hat{\mathbf{n}})^2 \right) + \\ & \frac{1}{2}\varepsilon_0 \left((\varepsilon - 1)(\nabla \phi_v \cdot \hat{\mathbf{t}})^2 \right) \qquad \text{on } \Gamma_{int}. \end{aligned} \tag{3.20}$$

Projections of the liquid stress tensor are not provided by the leaky dielectric model and are subsequently derived using continuum mechanics of viscous flows. Generally, the stress tensor can be expressed as a combination of two terms,

$$\mathbf{T}_l = -p\mathbf{I} + \boldsymbol{\tau}, \tag{3.21}$$

where p is the hydrostatic pressure defined by Eqn. (3.14), $\mathbf{I}$ is the identity matrix, and $\boldsymbol{\tau}$ is the deviatoric stress tensor. For a Newtonian viscous fluid,

$$\boldsymbol{\tau} = 2\mu\mathbf{E}, \tag{3.22}$$

where μ is the dynamic viscosity coefficient and $\mathbf{E}$ is the strain rate tensor of the form

$$\mathbf{E} = \frac{1}{2}(\nabla\mathbf{u} + \nabla\mathbf{u}^{\mathrm{T}}). \tag{3.23}$$

Equation 3.23 is defined as the symmetric component of the liquid velocity gradient $\nabla\mathbf{u}$. Combining Eqns. (3.21) to (3.23) results in a final stress tensor

$$\mathbf{T}_l = -p\mathbf{I} + \mu\left(\nabla\mathbf{u} + \nabla\mathbf{u}^{\mathrm{T}}\right). \tag{3.24}$$

The first projection of Eqn. (3.24) onto the interfacial normal direction $\hat{\mathbf{n}}$ can be shown to equate to

$$\begin{aligned} \mathbf{T}_l \cdot \hat{\mathbf{n}} =& [-p\mathbf{I} + \mu\left(\nabla\mathbf{u} + \nabla\mathbf{u}^{\mathrm{T}}\right)] \cdot \hat{\mathbf{n}} \\ =& -p\hat{\mathbf{n}} + \mu(\nabla\mathbf{u}\cdot\hat{\mathbf{n}} + \nabla\mathbf{u}^{\mathrm{T}}\cdot\hat{\mathbf{n}}). \end{aligned} \tag{3.25}$$

Expansion of the $\nabla\mathbf{u}\cdot\hat{\mathbf{n}}$ and $\nabla\mathbf{u}^{\mathrm{T}}\cdot\hat{\mathbf{n}}$ terms yield

$$\nabla\mathbf{u}\cdot\hat{\mathbf{n}} = \begin{bmatrix} \dfrac{\partial u_{\hat{\mathbf{n}}}}{\partial\hat{\mathbf{n}}} & \dfrac{\partial u_{\hat{\mathbf{t}}}}{\partial\hat{\mathbf{n}}} \\ \dfrac{\partial u_{\hat{\mathbf{n}}}}{\partial\hat{\mathbf{t}}} & \dfrac{\partial u_{\hat{\mathbf{t}}}}{\partial\hat{\mathbf{t}}} \end{bmatrix} \begin{bmatrix} \hat{\mathbf{n}} \\ 0 \end{bmatrix} = \begin{bmatrix} \dfrac{\partial u_{\hat{\mathbf{n}}}}{\partial\hat{\mathbf{n}}} \\ \dfrac{\partial u_{\hat{\mathbf{n}}}}{\partial\hat{\mathbf{t}}} \end{bmatrix} = \begin{bmatrix} \hat{\mathbf{n}}\cdot\nabla\mathbf{u}\cdot\hat{\mathbf{n}} \\ \\ \hat{\mathbf{t}}\cdot\nabla\mathbf{u}\cdot\hat{\mathbf{n}} \end{bmatrix}, \tag{3.26}$$

$$\nabla\mathbf{u}^{\mathrm{T}}\cdot\hat{\mathbf{n}} = \begin{bmatrix} \dfrac{\partial u_{\hat{\mathbf{n}}}}{\partial\hat{\mathbf{n}}} & \dfrac{\partial u_{\hat{\mathbf{n}}}}{\partial\hat{\mathbf{t}}} \\ \dfrac{\partial u_{\hat{\mathbf{t}}}}{\partial\hat{\mathbf{n}}} & \dfrac{\partial u_{\hat{\mathbf{t}}}}{\partial\hat{\mathbf{t}}} \end{bmatrix} \begin{bmatrix} \hat{\mathbf{n}} \\ 0 \end{bmatrix} = \begin{bmatrix} \dfrac{\partial u_{\hat{\mathbf{n}}}}{\partial\hat{\mathbf{n}}} \\ \dfrac{\partial u_{\hat{\mathbf{t}}}}{\partial\hat{\mathbf{n}}} \end{bmatrix} = \begin{bmatrix} \hat{\mathbf{n}}\cdot\nabla\mathbf{u}^{\mathrm{T}}\cdot\hat{\mathbf{n}} \\ \\ \hat{\mathbf{t}}\cdot\nabla\mathbf{u}^{\mathrm{T}}\cdot\hat{\mathbf{n}} \end{bmatrix}, \tag{3.27}$$

where $u_{\hat{\mathbf{n}}}$ and $u_{\hat{\mathbf{t}}}$ are the respective normal and tangential components of the liquid velocity. The second projection of Eqn. (3.24) across each direction is found by substitution of Eqns. (3.26) and (3.27) into Eqn. (3.25),

$$\hat{\mathbf{n}} \cdot \mathbf{T}_l \cdot \hat{\mathbf{n}} = -p + 2\mu \frac{\partial u_{\hat{\mathbf{n}}}}{\partial \hat{\mathbf{n}}} \qquad \text{on } \Gamma_{int}, \tag{3.28}$$

$$\hat{\mathbf{t}} \cdot \mathbf{T}_l \cdot \hat{\mathbf{n}} = \mu \left(\frac{\partial u_{\hat{\mathbf{n}}}}{\partial \hat{\mathbf{t}}} + \frac{\partial u_{\hat{\mathbf{t}}}}{\partial \hat{\mathbf{n}}} \right) \qquad \text{on } \Gamma_{int}. \tag{3.29}$$

Equations (3.28) and (3.29) represent the liquid stress tensor projections as a function of the flow velocity, enabling the implementation of interfacial boundary conditions Eqns. (3.17) and (3.18) within the EHD meniscus solver.

Once a steady-state meniscus morphology is found, the current density is integrated along the interface to find the total emitted current,

$$I = \int_{\Gamma_{int}} \mathbf{j} \cdot \hat{\mathbf{n}} \; d\Gamma_{int}, \tag{3.30}$$

where I is the current emitted from the interface.

3.3 Numerical Implementation

Solutions of Eqns. (3.4)–(3.17) are found for a fixed meniscus shape Γ_{int} using finite element methods implemented within the Distributed and Unified Numerics Environment (DUNE), an open source, modular C++ library for solving partial differential equations using grid-based methods [10, 13, 37].

The curvature of the initial meniscus is unlikely to satisfy the normal component of the boundary condition of interfacial stress of Eqn. (3.18), resulting in a non-zero residual. This residual is minimized using a pseudo-timestep routine that slowly perturbs the interfacial morphology until Eqn. (3.18) is satisfied. Once the interface is perturbed, an additional routine is required to deform the internal mesh nodes as well. The implemented interfacial propagation and internal mesh deformation are described in Subsections 3.3.2 and 3.3.4.

3.3.1 Laplace and Stokes Solvers

We begin by considering the multi-domain boundary value problem of Eqns. (3.4)–(3.6) and Eqn. (3.15). These equations state that within each subdomain Ω_{liq} and Ω_{vac}, Laplace's equation is solved with continuity of the electric potential and a jump condition for the electric potential gradient at the interfacial boundary. A monolithic routine is implemented to solve the coupled Laplace problem simultaneously across both subdomains. This is accomplished by discretizing the multi-domain boundary value problem using the Symmetric Interior Penalty Galerkin (SIPG) method [38]. To do so, we begin by defining the finite element space

$$S^k \coloneqq \{\varphi \in L_2(\Omega_{liq} \cup \Omega_{vac}) \quad : \quad \varphi|_T \in \Pi_k \; \forall T \in \mathcal{T}\} \tag{3.31}$$

where L_2 denotes the set of square–integrable functions and $\mathcal{T}$ is the set of elements in the multi–grid domain of $\Omega_{liq} \cup \Omega_{vac}$. Unlike traditional Galerkin methods, the functions of this space are not necessarily continuous at element boundaries and can hold multiple values. If we define Γ_T as the intersection of two adjacent elements T_{in} and T_{out}, then for a function $\varphi \in S^k$ we can define the jump across Γ_T as

$$[\![\varphi]\!]_\Gamma(x) \coloneqq \varphi^{\text{in}}(x) - \varphi^{\text{out}}(x) \qquad \forall x \in \Gamma_T. \tag{3.32}$$

Similarly, the average value on a given intersection can be defined

$$\{\varphi\}_\Gamma(x) \coloneqq \frac{1}{2}(\varphi^{\text{in}}(x) + \varphi^{\text{out}}(x)) \qquad \forall x \in \Gamma_T. \tag{3.33}$$

Using these definitions the multi-domain Laplace problem is recast into its weak formulation, a necessary prerequisite for discretization within the finite element method, of which the full derivation is provided in Appendix A. Applying the SIPG method requires the weak formulation to be recast into a residual formulation,

$$\text{Find } \varphi \in S^k \quad : \quad r^{\text{SIPG}}(\varphi, \theta) = 0 \qquad \forall \theta \in S^k, \tag{3.34}$$

where

$$
\begin{aligned}
r^{\mathrm{SIPG}}(\varphi,\theta) = &\int_{\Omega_{liq}} \nabla\varphi\cdot\nabla\theta \; d\Omega_{liq} + \int_{\Omega_{vac}} \nabla\varphi\cdot\nabla\theta \; d\Omega_{vac} \\
&- \int_{\Gamma_{int}} \{\langle\nabla\varphi,\hat{\mathbf{n}}\rangle\}[\![\theta]\!] \; d\Gamma_{int} - \int_{\Gamma_{int}} \{\langle\nabla\theta,\hat{\mathbf{n}}\rangle\}[\![\varphi]\!] \; d\Gamma_{int} \\
&+ \kappa \sum_{\Gamma\in\Gamma_{int}} \frac{1}{h_\Gamma} \int_{\Gamma} [\![\varphi]\!][\![\theta]\!] \; d\Gamma_{int} \\
&- \int_{\Gamma_{int}} [\![\langle\nabla\varphi,\hat{\mathbf{n}}\rangle]\!][\![\theta]\!] \; d\Gamma_{int},
\end{aligned}
\tag{3.35}
$$

is minimized. $\langle\cdot,\cdot\rangle$ denotes the inner product, κ is a penalty term, and h_Γ is the characteristic length scale of an arbitrary intersection Γ. The first two terms on the right-hand side of Eqn. (3.35) represent the volumetric residual within each subdomain, while the following two terms couple the subdomains by penalizing the interfacial jump in potential and enforcing continuity. The final term corresponds to an interfacial jump in the potential gradient, whose value is set by Eqn. (3.15). A slight reformulation of this equation yields

$$
[\![\langle\nabla\phi^{i+1},\hat{\mathbf{n}}\rangle]\!] = \left(\nabla\phi_l^{i+1} - \nabla\phi_v^{i+1}\right)\cdot\hat{\mathbf{n}} = \frac{\sigma^{i+1}}{\varepsilon_0} + (1-\varepsilon)\,\nabla\phi_l^{i}\cdot\hat{\mathbf{n}},
\tag{3.36}
$$

where ϕ_l^i denotes the liquid electric potential from the current iteration in the global solver routine. This formulation is required to enforce the final term, as the differing relative permittivity of the materials preclude Eqn. (3.15) from being expressed as a function of the difference between electric potentials. To overcome this, an identical term is added across each side of the equation.

An iterative routine is required to enforce the interfacial electric displacement condition of Eqn. (3.36) as the enforced value is a function of the solution itself. A solution to Eqns. (3.34)–(3.35) is found using a Dirichlet-Neumann fixed-point iteration, solving the problem within each subdomain using boundary data from the solution in the other subdomain. A detailed description of this routine can be found in [128].

Next, implementation of the Stokes problem described by Eqns. (3.11)–(3.12) is discussed. A complete formulation of the boundary value problem requires one to explicitly define the boundary conditions as functions of the solution variables $\mathbf{u}$ and p, and is provided by Eqns. (3.28) and (3.29). Only the tangent projection of the interfacial traction, Eqns. (3.17) and (3.29), is enforced in the finite element formulation of the Stokes boundary value problem, as the normal projection is handled by the interfacial and internal mesh deformation routines described in Subsections 3.3.3 and 3.3.4.

Equations (3.28) and (3.29) are used to specify a Neumann condition tangent to the interface within the weak formulation of the Stokes problem. The value said condition corresponds to is the applied tangential stress by the external electric field, given by Eqn. (3.19). Normal to the interface, the Dirichlet condition specified in Eqn. (3.13) is weakly enforced via a penalty method [9]. The no-slip and no-penetration conditions are enforced on the channel walls Γ_{emi}, while a zero Neumann condition is used at the inlet Γ_{inl}. The complete weak formulation is provided in Appendix B, where the boundary value problem is subsequently discretized and the linear system is solved iteratively using the generalized minimal residual method (GMRES) [108] with no preconditioner.

3.3.2 Global Algorithm

As the Laplace and Stokes routines are the primary modules of the EHD meniscus solver, we continue by describing the global algorithm that couples both routines to return a converged solution for the current density distribution across the steady-state interface. The EHD routine begins by solving Laplace's equation in each domain with the condition of potential continuity at the interface, Eqns. (3.4)–(3.6). An additional enforced interfacial boundary condition includes the discontinuity of the electric displacement of Eqn. (3.36), where during the initial iteration a value must be established for the surface charge density σ and the interfacial liquid potential ϕ_l. The surface charge density is found by reformulating the ion emission law of Eqn. (3.10) as a function of σ,

$$\sigma^{i+1} = \frac{h_c}{k_b T} \exp\left(\frac{1}{k_b T}\left[\Delta G - \sqrt{\frac{-\nabla\phi_v^i \cdot \hat{\mathbf{n}}}{4\pi\varepsilon_0/q^3}}\right]\right)\left(-K\nabla\phi_l^i - j_{conv}^i\right) \qquad \text{on } \Gamma_{int}, \tag{3.37}$$

where j_{conv} is the current density convected at the interface. On the right hand side of Eqn. (3.37), $\mathbf{j}\cdot\hat{\mathbf{n}}$ is decomposed as the sum of current conducted from the liquid and current convected tangent to the interface due to the applied electric traction. j_{conv} is found by reformulating the surface charge conservation of Eqn. (3.16),

$$\mathbf{j}\cdot\hat{\mathbf{n}} = \underbrace{\sigma\left(\hat{\mathbf{n}}\cdot\nabla\mathbf{u}\cdot\hat{\mathbf{n}}\right) - \mathbf{u}\cdot\nabla\sigma}_{j_{conv}} - K\nabla\phi_l \qquad \text{on } \Gamma_{int}. \tag{3.38}$$

Then, for a given iteration, the convected current at the interface is

$$j_{conv}^{i+1} = \sigma^i\left(\hat{\mathbf{n}}\cdot\nabla\mathbf{u}^i\cdot\hat{\mathbf{n}}\right) - \mathbf{u}\cdot\nabla\sigma^i \qquad \text{on } \Gamma_{int}. \tag{3.39}$$

Thus, to completely specify the boundary conditions for the Laplace solver we need interfacial values for ϕ_l, ϕ_v, and j_{conv}. These parameters are initialized to zero for the first iteration, where their values from the previous iteration are used thereafter. The Laplace solver is repeated until the integral of the square residual of the liquid and vacuum potential gradients normal to the interface are below a certain threshold,

$$R_l = \int_{\Gamma_{int}} \left[\nabla\phi_l^{i+1}\cdot\hat{\mathbf{n}} - \nabla\phi_l^i\cdot\hat{\mathbf{n}}\right]^2 \, d\Gamma_{int} < \epsilon_l, \tag{3.40}$$

$$R_v = \int_{\Gamma_{int}} \left[\nabla\phi_v^{i+1}\cdot\hat{\mathbf{n}} - \nabla\phi_v^i\cdot\hat{\mathbf{n}}\right]^2 \, d\Gamma_{int} < \epsilon_v. \tag{3.41}$$

Once this inner convergence is met, the electric potentials are used to specify interfacial boundary conditions for the Stokes solver. The Dirichlet condition normal to the interface is calculated using Eqn. (3.13), where the current density is recalculated using the ion emission law of Eqn. (3.10). For a given iteration, this takes the form

$$\mathbf{u}^i \cdot \hat{\mathbf{n}} = \frac{\sigma^i k_b T}{\rho(q/m)h_c} \exp\left(\frac{-1}{k_b T}\left[\Delta G - \sqrt{\frac{-\nabla\phi_v^i \cdot \hat{\mathbf{n}}}{4\pi\varepsilon_0/q^3}}\right]\right) \qquad \text{on } \Gamma_{int}. \tag{3.42}$$

The Neumann condition tangential to the interface is specified by a combination of Eqns. (3.17), (3.19) and (3.29). Again, for a given iteration, this takes the form

$$\hat{\mathbf{t}} \cdot \nabla\mathbf{u}^i \cdot \hat{\mathbf{n}} = \frac{-\sigma^i}{\mu}\nabla\phi_v^i \cdot \hat{\mathbf{t}} \qquad \text{on } \Gamma_{int}. \tag{3.43}$$

Once the Stokes problem is solved for the fluid velocity and pressure, the integral of the square residual of the surface charge is checked if below a certain threshold,

$$R_\sigma = \int_{\Gamma_{int}} \left[\sigma^{i+1} - \sigma^i\right]^2 \, d\Gamma_{int} < \epsilon_\sigma. \tag{3.44}$$

If this criteria is not met, the solver restarts using the new fluid velocity $\mathbf{u}$ to initialize the convected current at the interface j_{conv}. Otherwise, we continue to the final equilibrium condition where the residual of Eqn. (3.18) is checked. As previously mentioned, the right hand side of Eqn. (3.18) corresponds to the surface tension and therefore the shape of the meniscus. As such, any residual can only be minimized by perturbing the geometry of the interface Γ_{int}.

A flow chart summarizing the global algorithm is presented in Fig. 3.2. Steady-state solutions of the boundary value problem return the spatial distribution of current density across the interface, which, when integrated, is equal to the total emitted ion current. In Chapter 4, the EHD meniscus model is used to initialize injection number densities within a DSMC-PIC solver where the characteristics of the resulting plume are studied.

3.3.3 Interfacial Perturbation

The interfacial perturbation method presented is adapted from the work of Coffman [31]. Shown in Eqn. (3.14), the pressure drop at the interface is equivalent to the difference between

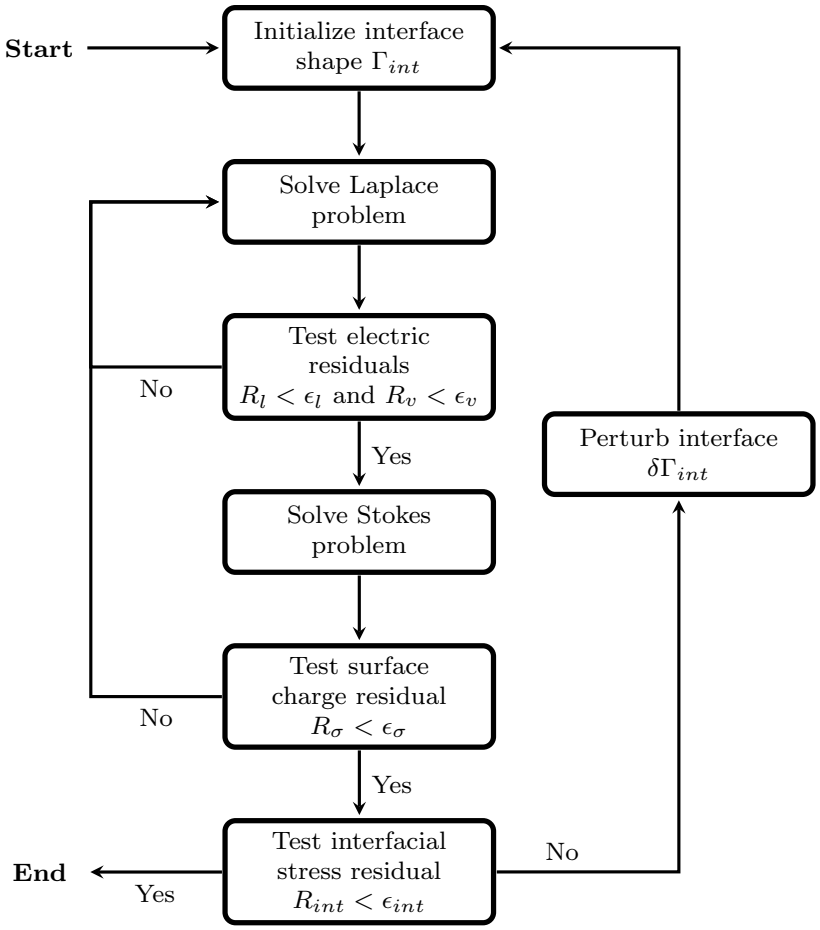

Figure 3.2: Global algorithm of the EHD meniscus solver

the reservoir pressure of the propellant and the pressure lost due to the flow rate of ions at the meniscus. The pressure drop between the channel input of the computational domain Γ_{inl} and the meniscus is considered small relative to the pressure contributions aforementioned and is neglected. At the end of an iteration, the normal stress balance at the interface of Eqn. (3.18) will not be satisfied unless it is in equilibrium, resulting in a residual term of the form

$$\hat{\mathbf{n}} \cdot (\mathbf{T}_l - \mathbf{T}_e) \cdot \hat{\mathbf{n}} + \gamma \nabla \cdot \hat{\mathbf{n}} = P_{int} \qquad \text{on } \Gamma_{int}, \tag{3.45}$$

where P_{int} can be interpreted as a transient pressure contribution that dynamically alters the interfacial shape at later timesteps. Given that the EHD solver seeks steady solutions, we must implement a pseudo–timestepping routine such that the transient pressure contributions are redistributed into the surface tension term $\gamma\nabla\cdot\hat{\mathbf{n}}$, thus perturbing the interfacial shape Γ_{int}.

Redistributing the pressure contributions requires a mapping between the surface tension term and the interfacial profile. It can be shown that for a two–dimensional Cartesian geometry, the surface tension term satisfies the given second–order, nonlinear ordinary differential equation,

$$P_\gamma = -\gamma\nabla\cdot\hat{\mathbf{n}} = -\gamma\frac{y''(x)}{[1+y'(x)^2]^{3/2}}, \tag{3.46}$$

where P_γ is the pressure contribution of the surface tension, and $y(x)$ is the spatial profile of intersection Γ_{int}. Reformulating Eqn. (3.46) into its homogeneous form results in

$$y''(x) + \frac{P_\gamma}{\gamma}[1+y'(x)^2]^{3/2} = 0. \tag{3.47}$$

By solving Eqn. (3.47) using standard methods for ordinary differential equations, we now have a means of obtaining a spatial profile of the interface Γ_{int} given an arbitrary surface tension pressure. This allows us to update the P_γ at the end of every iteration with a portion of the transient pressure contribution P_{int}, resulting in a new interfacial profile that progressively minimizes this residual once Eqn. (3.47) is solved again. The surface tension pressure for the $i+1$ iteration is given by

$$P_\gamma^{i+1} = P_\gamma^i + \beta P_{int}^i, \tag{3.48}$$

where $\beta\in(0,1]$ is an arbitrary relaxation parameter governing the rate at which the interface is perturbed. The ideal value of β is a function of the spatial profile stability during the current iteration. If the applied field is not stressing the interface such that a significant

perturbation is required to reach equilibrium for a given iteration, then β can be set to near unity. However, this is most likely not the case during ion emission due to the high nonlinearities of the coupled system and necessitates that $\beta \ll 1$ for the algorithm to stably approach an equilibrium configuration. The interfacial perturbation method is repeated until the integral of the square residual of the transient pressure is below some threshold value,

$$R_{int} = \int_{\Gamma_{int}} \left[P_{int}^{i+1} - P_{int}^{i}\right]^2 \, d\Gamma_{int} < \epsilon_{int}. \tag{3.49}$$

As redistribution of the interfacial nodes can cause instabilities in the surrounding elements within the fluid and vacuum domains Ω_{liq} and Ω_{vac}, due to potentially high distortions, an addition mesh moving method is required. A routine is sought that evolves the mesh while minimizing the likelihood of full or partial remeshing due to computational cost and is described in the subsequent section.

3.3.4 Internal Mesh Deformation

Once the meniscus is numerically perturbed, an additional interpolation function is required to map the boundary displacements to the internal mesh nodes. For unstructured grids, the radial basis function (RBF) interpolation method [34, 111] is an efficient scheme that generates high-quality meshes by solving a linear system that depends solely on the boundary nodes. As a result, the algorithm is capable of efficiently handling large mesh deformations, as in this case the time complexity would scale with the size of the interface instead of the liquid and vacuum meshes. In addition, information on grid connectivity is not required and the method preserves orthogonality near the deformation sites, minimizing the skewness introduced to interfacial cells due to a numerically evolving meniscus.

The implementation of RBF begins with the interpolating function $s_i(\mathbf{x}_k)$, which describes the displacement in direction i ($i = x, y, z$) at node $\mathbf{x}_k = [x_k, y_k]$, and is approximated as a weighted summation of basis functions φ and low-order polynomial $p(\mathbf{x}_k)$

$$s_i(\mathbf{x}_k) = \sum_{j=1}^{n_b} \alpha_j \varphi\Big(||\mathbf{x}_k - \mathbf{x}_j||\Big) + p(\mathbf{x}_k), \quad \text{for } \; k = 1 \ldots n_d \tag{3.50}$$

where n_b and n_d are the number of boundary and domain nodes, respectively. The polynomial $p(\mathbf{x})$ is also expressed as a weighted sum of additional polynomials $q(\mathbf{x})$ with degrees less than or equal to $p(\mathbf{x})$

$$p(\mathbf{x}) = \sum_{l=1}^{n_p} \beta_l q_l(\mathbf{x}), \tag{3.51}$$

where n_p is the number of polynomials $q(\mathbf{x})$. The weights α_j and polynomial coefficients β_j are determined using the interpolation conditions at the boundary. The first of which is

$$s_i(\mathbf{x}_j) = d_i(\mathbf{x}_j) \quad \text{for } \; j = 1 \ldots n_b, \tag{3.52}$$

where $d_i(\mathbf{x}_j)$ is the known displacement in direction i at boundary node $\mathbf{x}_j$. The second is an orthogonality condition on the weights α_j that acts to minimize the difference between the known displacements $d_i(\mathbf{x}_j)$ and the polynomial interpolation. In the implemented case where a linear polynomial is used, this condition takes the form

$$\sum_{j=1}^{n_b} \alpha_j = \sum_{j=1}^{n_b} \alpha_j x_j = \sum_{j=1}^{n_b} \alpha_j y_j = 0. \tag{3.53}$$

Combining Eqns. (3.52) and (3.53) into a linear system results in

$$\begin{bmatrix} \mathbf{\Phi}_\mathrm{b} & \mathbf{P}_\mathrm{b} \\ \mathbf{P}_\mathrm{b}^\mathrm{T} & \mathbf{0} \end{bmatrix} \begin{bmatrix} \boldsymbol{\alpha} \\ \boldsymbol{\beta} \end{bmatrix} = \begin{bmatrix} \mathbf{d}_{\mathrm{b}i} \\ \mathbf{0} \end{bmatrix}, \tag{3.54}$$

with $\boldsymbol{\alpha}$ and $\boldsymbol{\beta}$ respectively containing the coefficients for α_j and β_l. $\mathbf{\Phi}_\mathrm{b}$ is a $(n_b \times n_b)$ matrix whose entries at indices (j, k) contain the basis function evaluation $\varphi\Big(||\mathbf{x}_j - \mathbf{x}_k||\Big)$. $\mathbf{P}_\mathrm{b}$ is a $n_b \times n_p$ matrix where, in the linear polynomial case where $n_p = 3$, row j is given by $[1 \; x_j \; y_j]$. Explicit solutions of vector coefficients $\boldsymbol{\alpha}$ and $\boldsymbol{\beta}$ are given by

$$\boldsymbol{\alpha} = \boldsymbol{\Phi}_{\mathrm{b}}^{-1}(\mathbf{d}_{\mathrm{b}i} - \mathbf{P}_{\mathrm{b}}\boldsymbol{\beta}) \tag{3.55}$$

$$\boldsymbol{\beta} = (\mathbf{P}_{\mathrm{b}}^{\mathrm{T}}\boldsymbol{\Phi}_{\mathrm{b}}^{-1}\mathbf{P}_{\mathrm{b}}^{\mathrm{T}})^{-1}\mathbf{P}_{\mathrm{b}}^{\mathrm{T}}\boldsymbol{\Phi}_{\mathrm{b}}^{-1}\mathbf{d}_{\mathrm{b}i}. \tag{3.56}$$

Several choices of basis functions are available when solving Eqns. (3.55) and (3.56). Within the EHD solver, an RBF known as a thin plate spline is implemented of the form $\varphi(x) = x^2\log(x)$. This choice gives rise to a dense matrix $\boldsymbol{\Phi}_{\mathrm{b}}$ that is more computationally expensive to solve but generally leads to greater accuracy relative to RBFs that produce a sparse $\boldsymbol{\Phi}_{\mathrm{b}}$ [34]. Once the meniscus has evolved during a given iteration, the displacement of perturbed interfacial nodes defining the vector $\mathbf{d}_{\mathrm{b}i}$ and Eqns. (3.55) and (3.56) are calculated using standard linear solving methods. The displacements of the vacuum and liquid mesh nodes $d_i(\mathbf{x}_k)$ are then found by evaluating the original interpolation function of Eqn. (3.50) at each internal grid point

$$s_i(\mathbf{x}_k) = d_i(\mathbf{x}_k) \quad \text{for} \;\; k = 1 \ldots n_d, \tag{3.57}$$

where each displacement is individually interpolated across each direction and later superimposed to calculate the final position of an internal mesh node after the interface is perturbed

$$\mathbf{x}_k^{m+1} = \mathbf{x}_k^m + \sum_{i=1}^{2} d_i(\mathbf{x}_k^m) \quad \text{for} \;\; k = 1 \ldots n_d \tag{3.58}$$

for iteration m.

3.3.5 Verification Test Cases

Two verification test cases are presented in this section that demonstrate the enforcement of several interfacial boundary conditions implemented across the Laplace and Stokes solvers.

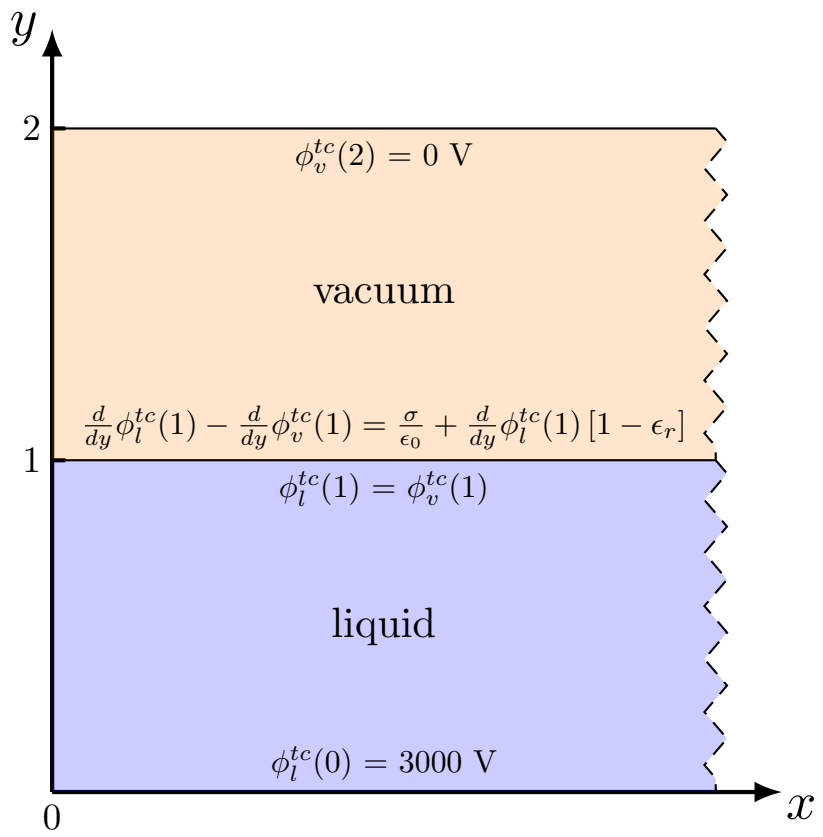

Figure 3.3: Simplified one-dimensional case to test implementation of multidomain Laplace solver.

3.3.5.1 Multidomain Potential Case

The first test case verifies the enforcement of the subdomain boundary conditions within the multidomain Laplace solver described in Subsection 3.3.1. Recall that the implemented routine solves for the potential distribution within separate liquid and vacuum subdomains whose solutions are coupled by conditions applied at a shared intersection. The global solution is found by iteratively solving the potential across each subdomain until the residual of Eqn. (3.35) is minimized. The boundary conditions of the intersection that are gradually enforced are the continuity of potential (the Dirichlet condition $\phi_l = \phi_v$) and the Neumann jump condition of Eqn. (3.36).

Enforcement of these conditions are demonstrated using a simplified domain and

comparing analytical solutions of Laplace's equation $\nabla^2\phi^{tc} = 0$ where ϕ^{tc} is the test case potential, against numerical simulation. The test problem, visualized in Fig. 3.3, consists of rectangular liquid and vacuum subdomains stacked on top of each other, each with a height of one unit and a length that extends infinitely. The electric potential varies solely in the y direction, Dirichlet values of 0 V and 3000 V are prescribed at the upper and lower boundaries respectively, and the aforementioned conditions are applied at their shared intersection. Given these values, it can be shown that the liquid potential ϕ_l^{tc} and the vacuum potential ϕ_v^{tc} are given by

$$\phi_l^{tc}(y) = \left(\frac{\sigma/\epsilon_0 - 3000}{\epsilon_r + 1}\right) y + 3000 \tag{3.59}$$

$$\phi_v^{tc}(y) = \left(\frac{\epsilon_r(\sigma/\epsilon_0 - 3000)}{\epsilon_r + 1} - \frac{\sigma}{\epsilon_0}\right)(y - 2). \tag{3.60}$$

The corresponding electric field magnitudes of Eqns. (3.59) and (3.60) are given by their negative gradients,

$$E_l^{tc}(y) = -\frac{d\phi_l^{tc}}{dy} = -\left(\frac{\sigma/\epsilon_0 - 3000}{\epsilon_r + 1}\right) \tag{3.61}$$

$$E_v^{tc}(y) = -\frac{d\phi_v^{tc}}{dy} = -\left(\frac{\epsilon_r(\sigma/\epsilon_0 - 3000)}{\epsilon_r + 1} - \frac{\sigma}{\epsilon_0}\right) \tag{3.62}$$

In this case, the surface charge is explicitly defined as $\sigma = 2000\epsilon_0$ and a relative permittivity of $\epsilon_r = 10$ is used. Substituting these values into Eqns. (3.59) to (3.62) at $y = 1$ results in an interfacial potential of $\phi_l^{tc} = \phi_v^{tc} = 2909$ V and electric field strengths $E_l^{tc} = 91$ V/m and $E_v^{tc} = 2909$ V/m. For comparison, the one-dimensional distribution of the same quantities from the numerical simulation is presented in Fig. 3.4. The numerical values are shown to match the analytical model throughout the domain, especially at the interface where the Dirichlet condition is not known a priori. As expected, the potential evolves at distinct linear rates across each subdomain and is continuous at their intersection. The corresponding electric field magnitude is a piecewise constant function demonstrating enforcement of the

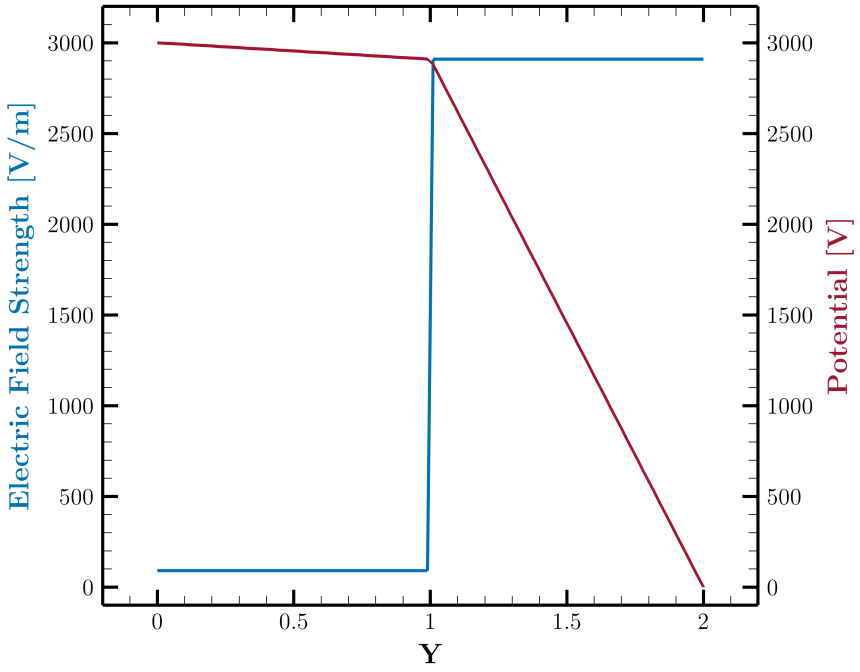

Figure 3.4: Numerical simulation of potential and electric field strength across the Laplace test domain.

jump condition Eqn. (3.15) at the center. It can be shown that the difference in the strengths of the analytical electric field across the interface is $E_v^{tc}(1) - E_l^{tc}(1) = 2818$ V/m, where the numerical simulation is again in agreement. In conclusion, Fig. 3.4 verifies that the implemented multidomain Laplace solver correctly determines the global potential distribution that enforces the Dirichlet and Neumann boundary conditions prescribed at the intersection of the subdomain.

3.3.5.2 Stokes Dual Boundary Condition Enforcement Case

A unique consideration of the boundary conditions in Eqns. (3.17) to (3.20) is required for the Stokes problem, and a test case is conducted to demonstrate its implementation. The simultaneous constraints of a normal-projected velocity and a tangent-projected viscous stress tensor at the interface require a dimensionally dependent enforcement of both a Dirichlet

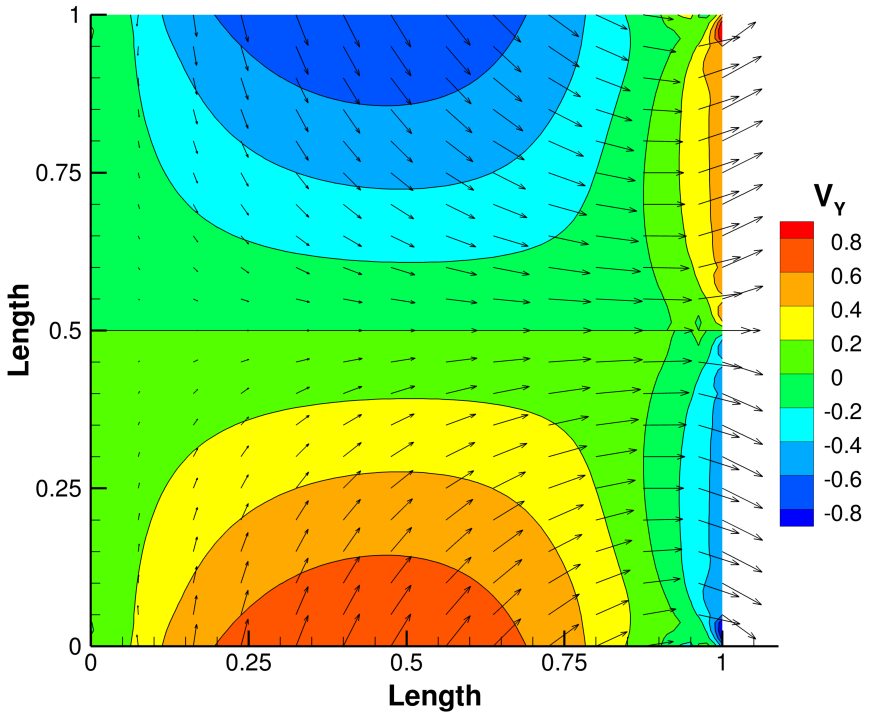

Figure 3.5: Test case of Stokes solver implementation demonstrating balance of dual normal-Dirichlet tangential-Neumann boundary condition at right outlet.

and a Neumann boundary condition. Physically, this corresponds to fluid flow normal to the meniscus due to ion emission, whereas viscous stresses act on the component of fluid moving tangentially to the free surface. While the Neumann condition naturally arises in the weak formulation of the Stokes problem, the Dirichlet condition requires weak enforcement using an added coercivity term. This term depends on an arbitrarily large penalty factor, α, which requires calibration such that the ratio of the boundary conditions is approximately unity; otherwise, the conditions are not enforced equally. As this penalty factor is problem dependent, a simple, qualitative test case is conducted to determine its value for viscous length scales, shown in Fig. 3.5. A square box with side length of unity is chosen, where zero-Neumann conditions are enforced at the top and bottom boundaries, a no-slip and no-penetration condition at the left boundary, and a dual normal-Dirichlet tangential-Neumann condition—both of magnitude unity—at the right boundary. The direction of the tangent

vector is mirrored in the horizontal center. Using the fluid properties of EMI-BF_4, Fig. 3.5 demonstrates quasi-equal enforcement of the directionally dependent boundary conditions.

3.3.6 Numerical Challenges

Despite the verification cases discussed in Subsection 3.3.5, several numerical challenges arose during the development of the EHD solver that precluded interfacial simulations from converging sufficiently and consistently towards a steady-state morphology for a given set of initial conditions. The source of these challenges is twofold: the linear solver implemented for the Stokes problem and the stability of the interfacial perturbation scheme, both of which are further described in the following sections.

3.3.6.1 Ill-Conditioned Stokes System

The Stokes problem of Eqns. (3.11) and (3.12) require specialized numerical methods to solve efficiency within a finite element formulation, especially relative to the Laplace system. This unique consideration comes from the variational form, of which the full derivation can be found in Appendix B. One complication in solving the system of Eqns. (3.11) and (3.12) arises due to unstable combinations of the pressure and velocity function spaces. The instability can be attributed to the incompressibility condition, $\nabla \cdot \mathbf{u} = 0$, which is a constraint to the velocity field within the momentum continuity equation Eqn. (3.11). Pressure, since it only appears within the momentum equation, effectively acts as a Lagrange multiplier to enforce the incompressibility condition. As a result, the function spaces of the solution $(\mathbf{u}, p)$ are coupled, and mixed velocity-pressure elements are required to solve the weak formulation of the problem. Once discretized, the block matrix system for the incompressible Stokes equations is given by

$$\begin{bmatrix} \mathbf{K} & \mathbf{G}^{\mathrm{T}} \\ \mathbf{G} & \mathbf{0} \end{bmatrix} \begin{bmatrix} \{\mathbf{u}\} \\ \{p\} \end{bmatrix} = \begin{bmatrix} \{\mathbf{f_u}\} \\ \{\mathbf{f_p}\} \end{bmatrix} \tag{3.63}$$

where $\mathbf{K}$ is the symmetric positive semi-definite matrix corresponding to the viscous term, $\mathbf{G}$ is the matrix corresponding to the divergence operator coupling the velocity and pressure, and $\mathbf{f}$ corresponds to the vector of source terms. The presence of the $\mathbf{0}$ matrix and coupled matrices $\mathbf{G}$ and $\mathbf{G}^{\mathrm{T}}$ characterizes the linear system of Eqn. (3.63) as a saddle-point problem that requires tailored numerical methods to solve effectively. Often this process begins by factorizing the saddle-point matrix as a block lower-upper system,

$$\begin{bmatrix} \mathbf{K} & \mathbf{G} \\ \mathbf{G}^{\mathrm{T}} & \mathbf{0} \end{bmatrix} = \begin{bmatrix} \mathbf{I} & \mathbf{0} \\ \mathbf{G}\mathbf{K}^{-1} & \mathbf{I} \end{bmatrix} \begin{bmatrix} \mathbf{K} & \mathbf{0} \\ \mathbf{0} & \mathbf{S} \end{bmatrix} \begin{bmatrix} \mathbf{I} & \mathbf{K}^{-1}\mathbf{G}^{\mathrm{T}} \\ \mathbf{0} & \mathbf{I} \end{bmatrix}, \tag{3.64}$$

where

$$\mathbf{S} = -\mathbf{G}\mathbf{K}^{-1}\mathbf{G}^{\mathrm{T}} \tag{3.65}$$

is known as the Schur complement matrix and is generally not explicitly available. The factorization of Eqn. (3.64) enables the use of separate linear solvers and preconditioners for the pressure and velocity components that are best suited for each system. Ideally, given the scale of the 2D EHD meniscus problem, an iterative Krylov method such as the generalized minimal residual method (GMRES) [108] combined with a block preconditioner that approximately inverts the velocity block $\mathbf{K}$ and approximates the pressure block $\mathbf{S}$ would be sufficient to reliably solve the system.

Unfortunately, dedicated Stokes solvers are not available within the DUNE numerics library used to develop the EHD solver, and incorporation of segregated schemes and preconditioners into the DUNE framework is outside the scope of this dissertation. Instead, a GMRES solver is implemented to solve Eqn. (3.63) without the addition of a block preconditioner. Generally, it is found that the absence of a suitable preconditioner leads to an ill-conditioned system with slow convergence times, high memory consumption, and poor scalability. This issue is exacerbated at the meniscus apex where mesh refinement is required to resolve the emission region, as the condition number of the saddle point matrix scales with

the grid resolution.

3.3.6.2 Interfacial Propagation Stability

The interfacial perturbation method of Subsection 3.3.3 is critical in determining the steady-state morphologies of the EHD meniscus. To ensure the interface is evolving towards an equilibrium solution, characterization of the conditions necessary for numerical and physical stability is required. We begin this process by reintroducing the normal interfacial stress balance of Eqn. (3.18) in the form of

$$T_e^{\hat{\mathbf{n}}} - T_l^{\hat{\mathbf{n}}} - P_\gamma = 0, \tag{3.66}$$

where $T_e^{\hat{\mathbf{n}}}$ and $T_l^{\hat{\mathbf{n}}}$ are the respective normal projections of the electric and liquid stress tensors and P_γ is the surface tension pressure. If a meniscus under the equilibrium condition of Eqn. (3.66) is perturbed, then each stress term can be decomposed into a steady and unsteady component such that $T = T_0 + \delta T$. The collective contribution of the unsteady terms would equate to a transient change in interfacial pressure δP_{int}, resulting in a modified normal stress balance

$$T_{e,0}^{\hat{\mathbf{n}}} - T_{l,0}^{\hat{\mathbf{n}}} - P_{\gamma,0} + \delta T_e^{\hat{\mathbf{n}}} - \delta T_l^{\hat{\mathbf{n}}} - \delta P_\gamma = \delta P_{int}. \tag{3.67}$$

The three left-most steady terms of Eqn. (3.67) are equal to those of Eqn. (3.66) and can be removed from consideration. When the remaining terms are normalized by the unsteady surface tension contribution δP_γ, it can be seen that

$$\frac{\delta T_e^{\hat{\mathbf{n}}}}{\delta P_\gamma} - \frac{\delta T_l^{\hat{\mathbf{n}}}}{\delta P_\gamma} - 1 = \frac{\delta P_{int}}{\delta P_\gamma}, \tag{3.68}$$

where $\delta P_{int}/\delta P_\gamma$ represents the ratio of the change in residual pressure to the change in surface tension. Physical stability of the evolving meniscus requires that the residual pressure

does not increase for a given perturbation in surface tension, i.e. $\delta P_{int}/\delta P_\gamma \leq 0$, resulting in the condition

$$\frac{\delta T_e^{\hat{\mathbf{n}}}}{\delta P_\gamma} - \frac{\delta T_l^{\hat{\mathbf{n}}}}{\delta P_\gamma} \leq 1 \tag{3.69}$$

to be satisfied at all points across the interface.

The condition required for numerical stability can also be determined by using a similar analysis. To illustrate this, we surmise a meniscus morphology that numerically satisfies Eqn. (3.66) for a given set of operating conditions during iteration $i-1$. During the next iteration, a perturbation is applied analogously to Eqn. (3.67) resulting in the numerical balance

$$\delta T_e^{\hat{\mathbf{n}},i} - \delta T_l^{\hat{\mathbf{n}},i} - \delta P_\gamma^i = \delta P_{int}^i. \tag{3.70}$$

Next the difference in the unsteady electric and liquid normal stress contributions is reformulated as a scalar multiple of the current surface tension perturbation, i.e. $\delta T_e^{\hat{\mathbf{n}},i} - \delta T_l^{\hat{\mathbf{n}},i} = \chi(\delta P_\gamma^i)$, enabling the residual pressure contribution to be expressed solely as a function of the surface tension pressure

$$(\chi - 1)\delta P_\gamma^i = \delta P_{int}^i. \tag{3.71}$$

Combining Eqn. (3.71) with the equation for the surface tension pressure during the $i+1$ iteration, Eqn. (3.48), allows us to determine the ratio of surface tension pressures between iterations as a function of numerical parameters

$$\frac{\delta P_\gamma^{i+1}}{\delta P_\gamma^i} = 1 + \beta(\chi - 1). \tag{3.72}$$

It can be seen from Eqn. (3.72) that when $\chi < 1$, $\delta P_\gamma^{i+1}/\delta P_\gamma^i < 1$ and the routine is physically stable. In turn, the numerical routine governed by β will act to suppress any perturbations. However, physical instability occurs when $\chi > 1$ which then acts to destabilize the numerical

routine as well. The coupling of physical and numerical stability results in a scheme that can be expected to converge when a steady-state solution exists and numerically diverge otherwise.

Such a routine may introduce challenges as seen in Subsection 3.3.6.1, where an ill-conditioned Stokes system is more likely to result in a difference between fluid and electrical stresses when $\chi > 1$, precluding the solver from finding stable equilibrium morphologies within a parameter space where a solution is expected. As a consequence, if a simulation does not converge, the user is unable to discern whether the source is inherently physical or numeric in nature. This issue may still occur regardless of the Stokes problem (e.g., if a simulation is initialized with a morphology that is significantly perturbed relative to the final steady-state configuration) and may be mitigated by implementing a scheme that decouples the physical and numerical stability conditions. Examples of such are demonstrated by Coffman [31] and Wohlhuter and Basaran [127], where their routines are capable of identifying unstable physical solutions at the cost of increased computational complexity.

3.4 Steady-State Meniscus Simulation

Simulations are performed to demonstrate the EHD model of Section 3.2 and its numerical implementation of Section 3.3. Numerical parameters and properties of the ionic liquid simulated are presented in Table 3.1. The characteristics of the resulting meniscus are compared with the simulations conducted by Gallud and Lozano [47] using a similar ionic liquid meniscus model undergoing steady ionic emission.

Comparisons are enabled by using similar physical properties of the working ionic fluid, and by using independent variables whose nondimensional values are consistent with those used in [47]. Namely, these nondimensional parameters are $\hat{E}_0, \hat{R}$, and $\hat{Z}$, which respectively correspond to the electric field, contact line radius, and hydraulic impedance of the liquid at the inlet. The non-dimensional external field is $\hat{E}_0 = E_0/E_c$, where $E_c = \sqrt{4\gamma/\epsilon_0 r_0}$ and r_0 is the contact line radius of the inlet channel. Calculating the electric field for a given

potential bias is found using $\Delta\phi = -Ez_0$, where z_0 is the distance between the emitter and extractor electrodes. The non-dimensional radius is $\hat{R} = r_0/r^*$, where r^* is the characteristic emission radius, and the non-dimensional hydraulic impedance is $\hat{Z} = Z/Z^*$, where Z^* is the characteristic impedance given by $Z^* = 2\gamma\rho(q/m)/KE^*r^{*3}$.

The meniscus morphology is initialized as an approximate Taylor cone with a half-angle of 48°, compared to the theoretical ideal of 49.29°. A lower angle is chosen to reduce the distance between the initial and final interfacial configurations, which in turn supports the numerical stability of the solver, as fewer mesh deformations are required. Evolution of the meniscus morphology across several iterations is presented in Fig. 3.6. Generally, larger displacements are observed throughout the pseudo-timestep procedure near the emitter centerline relative to the region near the contact line radius. This is especially apparent at the apex itself, where a circular cap emerges whose radius is expected to be on the order of the characteristic emission radius and is in agreement with similar literature [105]. The magnitude of interfacial displacement is observed to decrease with increasing iteration, indicating that the solver is converging towards a final morphology.

Table 3.1: Properties of the working ionic liquid and configuration parameters of EHD meniscus simulations

Parameter	**Value**
Ion Solvation Energy, ΔG	1.0 eV
Electric Conductivity, K	1.0 S/m
Viscosity, μ	0.037 Pa·s
Surface Tension, γ	0.05 N/m
Mass Density, ρ	1240 kg/m^3
Charge to Mass Ratio, q/m	10^6 C/kg
Relative Permittivity, ϵ_r	10
Voltage Bias, $\Delta\phi$	2104 V
Hydraulic Impedance, Z	5.3×10^{19} Pa·s/m^3
Reservoir Pressure, p_r	0 Pa
Channel Radius, r_0	1 μm
Emitter-Extractor Electrode Distance, z_0	20 μm

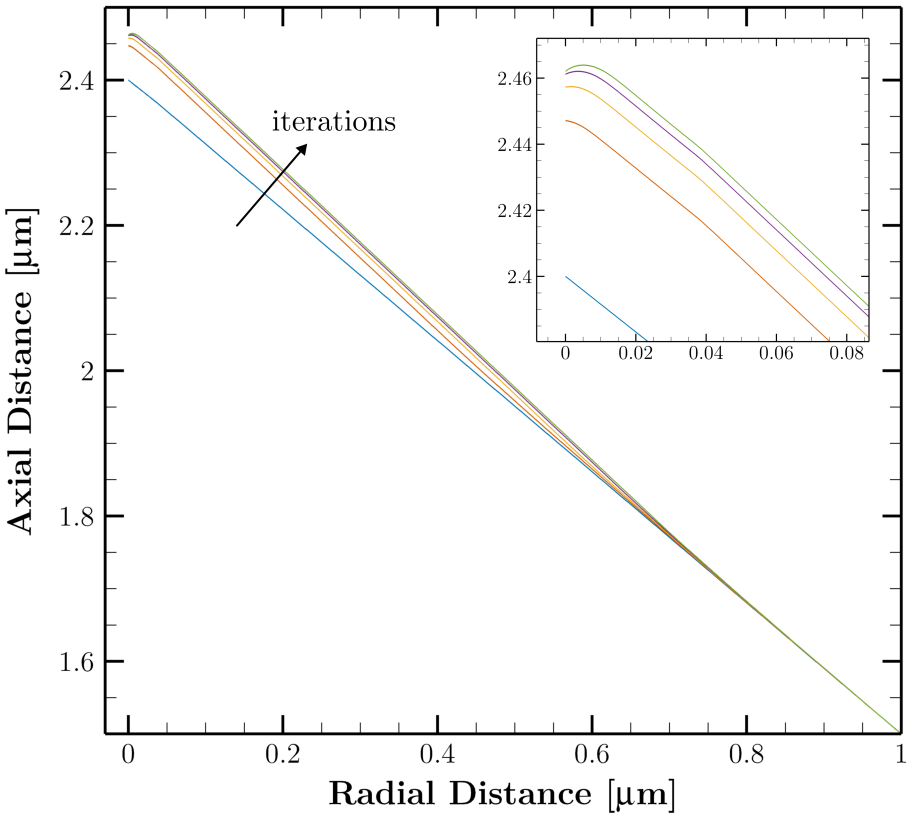

Figure 3.6: Evolution of meniscus morphology from an initial approximate Taylor cone configuration to subsequent configurations with each pseudo-timestep iteration. The inset provides a detailed view of the morphologies near the meniscus apex.

However, after a set number of iterations, even with RBF interpolation for internal deformation, the mapping from mesh to spatial coordinates becomes increasingly ill-conditioned with continued displacement—a property observed in cases where high curvature develops relative to the initial configuration. Consequently, the Laplace and Poisson linear systems also deteriorate with each iteration. These challenges are further exacerbated by the numerical issues discussed in Section 3.3. For instance, the absence of a preconditioner in the Stokes system limits solver performance, as the problem condition number grows with each interfacial perturbation. Ultimately, these challenges result in a subsequent interfacial morphology that

is unable to be solved due to the system instability. One of the roots in the interfacial stability problem lies in the Eulerian specification of the flow field that normally precludes handling of transient boundaries as physical quantities are mapped to fixed points in space. The implemented interfacial perturbation method attempts to overcome this by applying a separate Lagrangian update to the boundary between solver iterations and redistributes the internal mesh nodes via interpolation of the boundary deformations. Although this may be suitable for certain interfacial evolutions, the complete decoupling between the finite element formulation and the internal mesh node evolution often prevents the global solver from surpassing iteration counts on the order of 10 due to the eventual degradation of mesh quality. Extensive simulations show that while RBF interpolation can resolve some interfacial deformations, it often lacks the capacity to handle the magnitude needed for a transient EHD meniscus without extensive remeshing operations. For this reason, it is recommended that future studies consider the implementation of an arbitrary Lagrangian-Eulerian (ALE) formulation [64] to better address the strong distortions observed in the continuum domains. In the ALE description, the mesh evolution is integrated within the weak formulation of the multi-domain problem, handling both the deformation of the domain and the transport of quantities in a single, unified framework. Although this method would not entirely eliminate the need for remeshing in cases of extreme deformation, it would significantly extend the range of numerically stable perturbations before remeshing becomes necessary.

Despite these drawbacks, the final simulated meniscus shares characteristics with converged menisci observed in the literature [30, 47]. The demonstrated simulation falls within an operational regime defined by nondimensional contact line radii greater than $\hat{R} \approx 16$ and fields within the range $0.49 < \hat{E}_0 < 1.1$. Results from [47] indicate that static menisci in this regime have an emission region on the order of the non-dimensional size $r^*/r_0 = \hat{R}^{-1}$ and non-dimensional electric fields on the order of the non-dimensional critical field $E^*/E_c \sim \hat{R}^{1/2}$. In the simulation conducted, $r^*/r_0 \approx 0.018$ and is on the same order to $\hat{R}^{-1} \approx 0.047$, suggesting the solver under-approximates the emission region size. The nondimensional

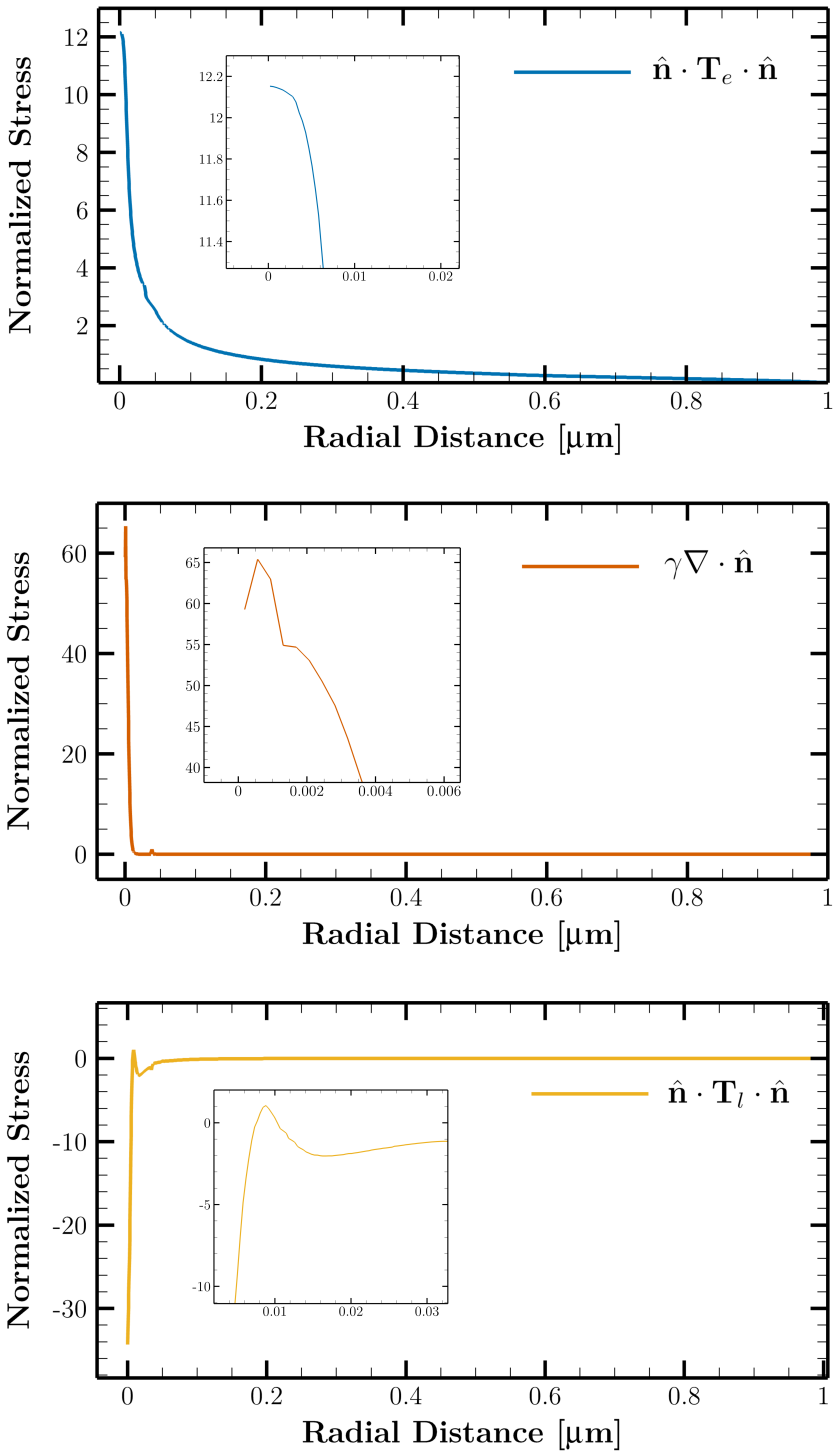

Figure 3.7: From top to bottom, normalized distributions of the (a) normal electric stress, (b) surface tension, and (c) normal liquid stress across the interface during the final stable iteration of the EHD meniscus solver.

field strength at the apex is $\hat{E} \approx 3.73$ and is on the order of the non-dimensional critical field $\hat{E}^* \approx 4.62$. The simulated meniscus emits a non-dimensional current $\hat{I} \approx 2.1$, which is about an order of magnitude larger than the analogous value from [47] of 0.15. The relative agreement in field strengths but disagreement in the emitted current suggest that the source of the discrepancy is likely in the numerical handling of the hydrodynamics.

As mentioned, prototypical equilibrium shapes in this regime appear qualitatively similar to a Taylor cone with a closed apex where emission is occurring [29]. The reason for this is demonstrated in Fig. 3.7, where the normal projections of the interfacial stresses of Eqn. (3.18) are plotted across the meniscus during the final stable iteration. Interfacial stresses are normalized by the inlet capillary pressure $P_c = 2\gamma/r_0 = 10^5$ Pa. Near the emitting region in the electric stress distribution of Section 3.4, strong electric fields on the order of E^* are balanced by high curvatures. However, it can be seen that the summation of each stress magnitude at the meniscus apex is non-zero, demonstrating that a large transient pressure P_γ is present within the system. Compared to the stress balance distributions in [47] within the same operational regime, the largest distinction is within the fluid stresses. In Section 3.4 the simulated fluid pressures are extraordinarily high relative to the capillary pressure, contradicting the behavior observed in the literature in which the inverse phenomenon occurs and local capillary pressures at the apex are dominant. Another distinction is observed in the velocity field near the emission region, where vortices are expected due to the advection of liquid toward the centerline and only a small fraction of the transported fluid undergoing evaporation. This qualitative behavior is observed during initial iterations of the EHD solver, but vanishes likely due to the continued ill-conditioning of the Stokes problem. These disagreements with the established literature suggest that the aforementioned numerical challenges likely manifest in the solution of the liquid velocity and pressure fields, whose errors ultimately propagate into the interfacial balance, resulting in an updated meniscus that becomes increasingly unstable.

3.5 Conclusions

In this chapter, a comprehensive EHD meniscus model was developed that incorporates both electrostatic and hydrodynamic stresses at the emitter apex to calculate field-induced ion emission. The model integrates a multiscale approach that resolves characteristics at the micron-scale meniscus while simultaneously accounting for the far-field interactions in the bulk fluid and vacuum domains. By employing the Taylor–Melcher leaky dielectric framework alongside a phenomenological ion evaporation law, the formulation successfully couples the electrostatic and fluid mechanical phenomena governing steady-state ionic emission of an ionic liquid.

The numerical implementation of the model was accomplished through a multi-domain finite element formulation within the DUNE framework that defines a bulk liquid and vacuum subdomain and a dynamic meniscus at their interface. Several boundary conditions are described and enforced at the meniscus, including continuity of the electric potential across subdomains and accurately imposed interfacial stress balance conditions. Verification test cases confirmed the solver's ability to reproduce analytical solutions for the Laplace problem and qualitatively enforce boundary conditions for the Stokes problem. Nonetheless, several numerical challenges were identified—most notably, the ill-conditioning of the Stokes system under high mesh refinement and the sensitivity of the interfacial perturbation scheme to large deformations. These challenges highlight the need for alternative numerical strategies, such as the integration of arbitrary Lagrangian–Eulerian formulations and tailored preconditioning techniques of the Stokes system, to improve mesh stability across iterations and global solver convergence.

Despite these limitations, the simulation results exhibit qualitative agreement with theoretical expectations and experimental observations. The emergent meniscus morphology, characterized by a near-Taylor cone shape with a closed apex, and the spatial distribution of interfacial stresses align with established literature. This work thus lays a robust foundation

for future investigations into ion emission dynamics, while also identifying key areas for numerical refinement and model extension to additional spatial and operational configurations.

Chapter 4

Coupled Kinetic Plume Model

This chapter presents the development and implementation of a coupled kinetic plume model for analysis of end-to-end behavior of a single-emitter ionic electrospray thruster. Building on the EHD meniscus simulations described in Chapter 3, a novel ionic emission model is presented and used to initialize a plume model at the emitter apex. Contrary to the continuum approaches taken when considering the meniscus dynamics, the plume model implements kinetic-based particle methods to simulate the downstream dynamics of ionic species within the beam. Axisymmetric simulations of the end-to-end model are compared against measurements of the porous-media electrospray thruster known as the Air Force Electrospray Thruster Series 2 (AFET-2), developed at the Air Force Research Laboratory (AFRL) [99].

The chapter begins with Section 4.1 by detailing the computational domain, designed to replicate the physical characteristics of the AFET-2 thruster's emitter and extractor geometry. In Section 4.2, the ionic emission model is derived and bridges the meniscus and plume regions through a one-way coupling. The model employs a reduced-order analytical framework to predict ionic emission currents based on electric field distributions at the meniscus, which are derived from the EHD solver. This is followed by the initialization of a direct simulation Monte Carlo (DSMC) and particle-in-cell (PIC) hybrid kinetic model in Section 4.3 to simulate the plume's spatial and temporal evolution. Several enhancements to the original PIC implementation are introduced, enabling the accurate treatment of single-polarity ionic

plumes, as well as the inclusion of a field-free fragmentation model to capture the dissociation dynamics of ion clusters.

Results from the simulations are validated against experimental data obtained from AFET-2 in Section 4.5, with analyses covering emission currents, thrust, and various spatial characteristics of the ion beam. The findings not only emphasize the importance of capturing meniscus-level physics but also highlight key challenges, such as fragmentation and neutral species effects, that impact thruster performance. The chapter concludes with insights into the model's implications for optimizing electrospray thruster designs and its potential for guiding future experimental investigations.

4.1 Computational Domain

The computational domain is designed to mirror the physical configuration of a single emitter within the multiplexed, porous-media electrospray thruster AFET-2 fabricated by Natisin et al. [99]. Shown in Fig. 4.1, the two-dimensional, axisymmetric domain consists of a single hyperboloidal emitter with the following geometric parameters: a base radius $r_{\text{emi}} = 80$ μm, height $z_{\text{emi}} = 400$ μm, and radius of curvature at the tip of $r_{\text{tip}} = 10$ μm. The emitter is positioned flush with the base of the extractor electrode, which itself extends a radial distance $r_{\text{ext}} = 254$ μm away from the emitter center, and has a thickness of $z_{\text{ext}} = 75$ μm. Surrounding the emitter and extractor electrode, the simulation boundary extends radially to $r_{\text{dom}} = 500$ μm and axially to a height of $z_{\text{dom}} = 1000$ μm.

At the tip of the emitter, an inlet channel is integrated into the domain to mimic the porous structure of the AFET-2 configuration. The channel, with a radius and length each set to $r_c = 1$ μm, replicates the pore size of P5 borosilicate glass used in the original fabrication by Natisin et al. [99]. Within the channel defines the liquid subdomain, and is bounded between the inlet boundary at the bottom and the interfacial meniscus. Beyond the meniscus defines the vacuum subdomain that contains both the emission and plume regimes. The meniscus itself is initialized with a quasi-Taylor cone morphology, with the primary

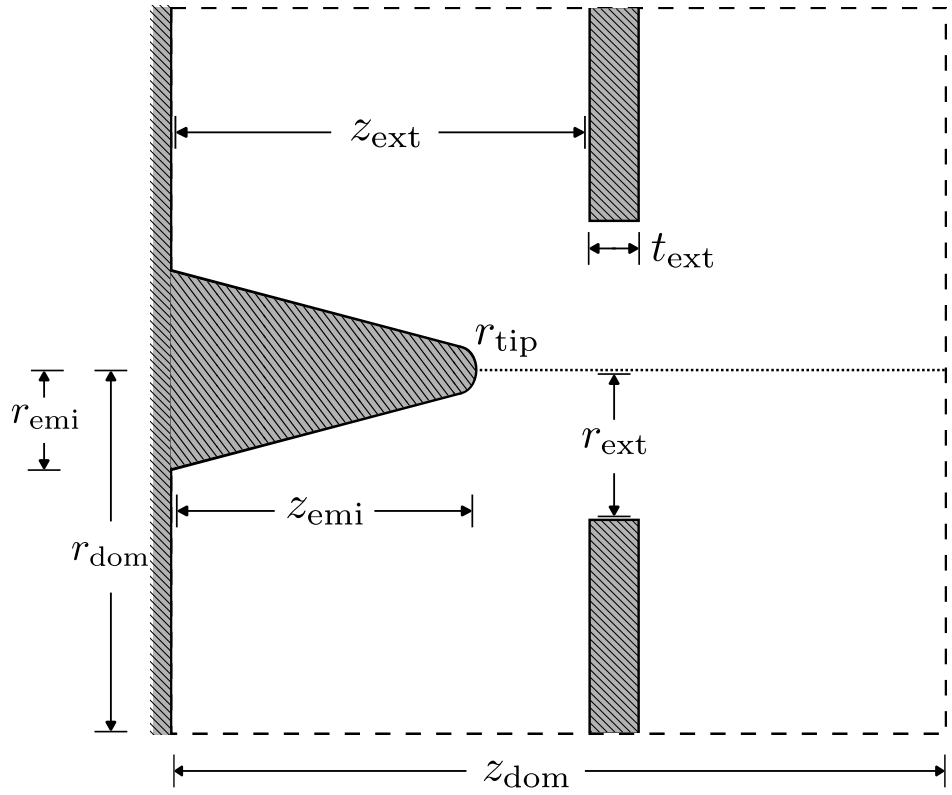

Figure 4.1: Single emitter simulation domain of the weakly-initialized kinetic plume model.

distinction being a rounded tip with a radius of curvature on the order of the characteristic emission radius r^*, which is a function of the ionic liquid propellant. A detailed description of the emission model is provided in Section 4.2.

4.2 Semi-Empirical Ionic Emission Model

An additional lower-fidelity ionic emission model is presented as a partial alternative to the EHD meniscus model described in Chapter 3. The emission model is not a complete substitute of the EHD model as it utilizes components of the original finite-element framework and is only applicable under a subset of operational conditions, described further in the subsequent sections. This alternative model—henceforth referred as the ionic emission model—is designed to calculate the number density of each evaporated species as a function

of the applied electric field at the site of emission. Broadly, it utilizes the EHD meniscus model of Chapter 3 to resolve the field distribution at the meniscus, and a semi-empii analytical model that utilizes the simulated field to approximate the total emission current for a given extractor voltage. From this current, the number densities of the evaporated species are calculated. These densities are subsequently used as a weak boundary condition to initialize a kinetic plume model. The derivation and description of the emission model are elaborated in the following paragraphs.

Initialization of the EHD model requires that the meniscus morphology be prescribed a priori. For this study, the meniscus shape is set to that of an idealized Taylor cone whose outer edge is pinned to an inlet channel of contact radius $r_c = 1\ \mu m$, which corresponds to a fixed contact angle of $\theta_c = 139.3°$. The meniscus apex is also rounded into a spherical cap whose radius matches that of the characteristic emission radius, r^*. This initial meniscus geometry is approximately in alignment with the literature [30, 47], suggesting that as the ratio of the contact radius to the emission radius decreases, the meniscus profile regularizes, reducing the tip sizing to a radius on the order of r^*. At this regularized state, high-fidelity simulations have suggested that the emitting current varies solely as a function of the applied electric field and is on the order of a characteristic emission current, I^*. This informs the basis of a simplified emission model first introduced by Gallud and Lozano [47], where the emitted current can be approximated solely as a function of the vacuum electric field strength near the meniscus apex. Physically, at this emission regime the high field strengths results in interfacial electric stresses that are balanced nearly completely by the surface tension. These stresses overcome the influence of viscous effects, the pressure differential from the reservoir, and temperature gradients from Ohmic dissipation. The effects of conduction drive the meniscus electrokinetics, such that variations in the electric field are linear with respect to the emission current up to a maximum value on the order of I^* and is bounded by the finite conductivity of the ionic liquid propellant [30].

Derivation of the analytical model begins with the kinetic process describing the rate

of ion evaporation from a conductive nonmetallic liquid [65],

$$j_e = \sigma \frac{k_B T}{h} \exp\left(-\frac{\zeta}{k_B T}\right), \tag{4.1}$$

where k_B is the Boltzmann constant, h is the Planck constant, T is the liquid temperature, σ is the surface charge density, and ζ is the activation energy of the species evaporation process. Using the Müller-Schottky field evaporation model for polar liquids, the activation energy can be modeled with the form [77],

$$\zeta = \Delta G - G(E_n^v) \quad \text{where} \quad G(E_n^v) = \sqrt{\frac{q^3 E_n^v}{4\pi\epsilon_0}}, \tag{4.2}$$

where ΔG is the solvation energy of the evaporated species, E_n^v is the normal component of the electric field on the vacuum side of the meniscus, q is the elementary charge, and ϵ_0 is the vacuum permittivity. Significant emission is not observed until the activation energy is sufficiently reduced past the solvation energy, $\zeta = \mathcal{O}(k_B T) \ll \Delta G$, and can be used to define a critical emission field $E^* \equiv 4\pi\epsilon_0(\Delta G)^2/q^3$.

Once activated, steady-state emission of species is only enabled when the charged meniscus is in mechanical equilibrium, i.e. the electrical traction from the applied field is balanced by the liquid surface tension. Assuming the emission region takes the form of a spherical cap with emission radius r^*, the stress balance can be approximated as $T_n^e = 2\gamma/r^*$, where T_n^e is the vacuum electric stress from the field normal to the meniscus and γ is the coefficient of surface tension. Expansion of the electric traction via the Maxwell stress tensor results in the balance equation,

$$\frac{1}{2}\epsilon_0(E_n^{v\,2} - \epsilon E_n^{l\,2}) = \frac{2\gamma}{r^*}, \tag{4.3}$$

where ϵ is the relative permittivity and E_n^l is the normal electric field on the liquid side of the meniscus. Equation (4.3) can be further modified when considering the behavior of ionic liquid menisci near room temperature. It has been shown that under steady emission, the

meniscus morphology normalizes such that $E_n^v \sim E^*$ [30, 31]. At these conditions, the ratio of the characteristic charge emission time is small relative to the characteristic charge relaxation time, limiting the amount of surface charge that can accumulate at the interface. The result is a meniscus whose behavior approaches that of a pure dielectric where $E_n^l \sim E_n^v/\epsilon$. Applying these approximations onto Eqn. (4.3) results in an updated stress balance,

$$\frac{1}{2}\epsilon_0 E^{*2}\left(\frac{\epsilon-1}{\epsilon}\right) = \frac{2\gamma}{r^*}. \tag{4.4}$$

For nominal ionic liquids where the factor $(\epsilon-1)/\epsilon$ is near unity, Eqn. (4.4) can be used to define the characteristic emission radius, $r^* \sim 4\gamma/\epsilon_0 E^{*2} \equiv q^6\gamma/4\pi^2\epsilon_0^3\Delta G^4$.

Within the bulk liquid, the characteristic flow velocity near the emission region is defined as

$$u^* = \frac{j^*}{\rho(q/m)}, \tag{4.5}$$

where ρ is the mass density of the ionic liquid, m is the mass of the evaporated species, and j^* is the characteristic emission current density. Values for this characteristic velocity range from 10^{-1}-10^{-2} m/s for many typical ionic liquids [109]. The hydrodynamic time scale can then be defined as r^*/u^*, which is nominally large relative to the charge relaxation time scale, $\epsilon\epsilon_0 K$. As a result, charge transport can be considered instantaneous relative to the meniscus hydrodynamics, enabling use of an Ohmic conduction model for the liquid electrokinetics,

$$j_e = KE_n^l, \tag{4.6}$$

where K is the electrical conductivity. Using the aforementioned relations, it can be shown that the characteristic emission current density is then $j^* \sim KE^*/\epsilon = 4\pi\epsilon_0 K(\Delta G)^2/q^3\epsilon$, and can be used to define a characteristic emission current $I^* = A_e j^* = A_e KE^*/\epsilon$, where A_e is the surface area of emission.

In the analytical model, the emission area is approximated as a spherical cap of radius

r_{cap}, where r_{cap} is on the order of the characteristic emission radius r^*, i.e. $A_e = 2\pi r_{\text{cap}}^2 \approx 2\pi r^{*2}$. Using the aforementioned scaling laws, the stress balance of Eqn. (4.3) can be approximated by reformulating the surface tension term as a function of the emission current density and emission current,

$$\frac{1}{2}\epsilon_0(E_n^{v\,2} - \epsilon E_n^{l\,2}) \approx 2\gamma\sqrt{\frac{2\pi j_e}{I_{\text{cap}}}}, \tag{4.7}$$

where I_{cap} is the total emission current under the spherical cap approximation. To express this current solely as a function of the vacuum electric field, Eqns. (4.1), (4.6), and (4.7) require closure of the surface charge density. This is achieved by considering the interfacial electrostatic boundary at the meniscus,

$$\sigma = \epsilon_0(E_n^v - \epsilon E_n^l). \tag{4.8}$$

It should be noted that Eqn. (4.8) is still valid within the steady emission regime (where $E_n^l \sim E_n^v/\epsilon$) as although the surface charge density is small relative to the electric displacements, its value remains nonzero. Equation (4.8) is used to remove the direct surface charge dependency of Eqn. (4.1). To do so, Eqn. (4.1) is first reformulated as a surface charge equation as a function of the emission current density and vacuum electric field,

$$\sigma = j_e F(E_n^v), \tag{4.9}$$

where

$$F(E_n^v) = \frac{h}{k_B T}\exp\left(\frac{\zeta}{k_B T}\right). \tag{4.10}$$

Using Eqns. (4.8), (4.9), and (4.10), we can derive an equation for the liquid electric field component as a function of the emission charge density and the vacuum electric field component,

$$E_n^l = \frac{\epsilon_0 E_n^v - j_e F(E_n^v)}{\epsilon_0 \epsilon}. \tag{4.11}$$

Eqn. (4.11) describes a closed form expression that expands upon the boundary condition of Eqn. (4.8) and utilizes the emission current density (instead of the surface charge) to bridge the field distributions across the meniscus interface. Its dimensionality can be further reduced due to the Ohmic conduction model of Eqn. (4.6), enabling the emission current density to be expressed solely as a function of the vacuum field distribution,

$$j_e = \frac{E_n^v}{(\epsilon/K) + (F(E_n^v)/\epsilon_0)}. \tag{4.12}$$

Finally, substituting Eqns. (4.11) and (4.12) into Eqn. (4.7) results in an expression where the emission current is approximated as a function of the vacuum electric field,

$$I_{\text{cap}} \approx \frac{2\pi E_n^v}{\left[\frac{\epsilon}{K} + \frac{F(E_n^v)}{\epsilon_0}\right]\left[\frac{\epsilon_0 {E_n^v}^2}{4\gamma}\left(1 - \frac{\epsilon}{\left[\epsilon + \frac{K}{\epsilon_0}F(E_n^v)\right]^2}\right)\right]^2}. \tag{4.13}$$

Emission characteristics of passively-fed porous electrosprays are inherently complex and unique to each thruster configuration. Consequently, the emission model presented in Eqn. (4.13) only provides an order-of-magnitude approximation to the emission current from a single emitter. Numerous factors, both numerical and physical, can introduce higher-order deviations in operational characteristics for a given thruster configuration. For instance, spatial non-uniformities have been observed in the emission of multiplexed emitter arrays, potentially caused in part by variance in pore sizing resulting in hydraulic coupling among emitters [23, 55]. To address these effects, a calibration factor C_f is introduced into the emission model, scaling the computed field distribution at the meniscus apex so that the predicted emission current from a single emitter matches the experimentally measured average current per emitter of the AFET-2 thruster array. Once calibrated with this factor C_f, the

emission model can serve as a surrogate for the specific thruster configuration, allowing for the initialization of plume simulations across a range of operational conditions consistent with the AFET-2 thruster.

In summary, the EHD meniscus model resolves the vacuum electric field profile across the interfacial meniscus, which then informs an analytic spherical cap emission model described by Eqn. (4.13). Due to inherent complexities in electrospray physics, this analytic approach is calibrated with an empirically derived scaling factor, C_f, ensuring the emission current approximates the experimentally measured average per emitter from the AFET-2 thruster. The calibrated emission current subsequently serves as a boundary condition for the initialization of the downstream plume model, described further in Section 4.3.

4.3 Plume Model

The plume model is used to simulate trajectories of the evaporated species from the emission site to the downstream exit plane via modification of an in-house particle solver, MPIC [24]. A description of MPIC as well as the changes made to account for single polarity ionic plumes are presented in Subsection 4.3.1. A fragmentation model for select evaporated species and its implementation is presented in Subsection 4.3.2. Lastly, details of the weak coupling between the emission and plume models are described in Subsection 4.3.3.

4.3.1 MPIC Overview and Modifications for Single Polarity Ionic Plumes

MPIC was developed by coupling the direct simulation Monte Carlo (DSMC) method for rarefied gas flow dynamics and the particle-in-cell (PIC) method that calculates inter-particle electrostatic forces as a result of applied and induced electric fields. It has been validated and implemented in several studies of plasma plumes [52, 94, 115]. The subsequent sections provide a description of each numerical method, how they are implemented within MPIC, and what modifications were made for its application to ILIS plumes.

4.3.1.1 Direct Simulation Monte Carlo Method

The first numerical method implemented in MPIC is DSMC. Proposed by Graeme Bird [12], the DSMC method simulates dilute gas flow where the molecular mean free path is of comparable order with respect to a characteristic length scale. This regime is characterized by the dimensionless Knudsen number (Kn),

$$Kn = \frac{\Lambda}{L}, \tag{4.14}$$

where Λ is the mean free path of a given molecule and L is a representative physical length scale of the system. When the Knudsen number is approximately near or greater than 0.01, then the continuum assumption underlying the Navier-Stokes equations may no longer be valid and a statistical approach is required to resolve the flow-field physics.

DSMC is one such probabilistic method, where rarefied flows are simulated using representative macroparticles that are individually tracked within a finite domain [16]. Macroparticles are often representative of many physical molecules, as only a small subset of total molecules require simulation for a sufficient molecular description of the flow field. At any given timestep, the position and velocity of each macroparticle defines the dilute gas state, where these quantities are used to advect the particles for subsequent timesteps. Additional probabilistic models govern how intermolecular collisions and molecule-surface collisions influence particle trajectories.

Within the plume model, every species is uniquely represented by its own macroparticle type. The DSMC component of MPIC is predominantly responsible for tracking each particle trajectory, with the governing forces affecting trajectories emerging from the electric field (which is calculated independently by the PIC routines) instead of local contact forces from other particles and domain boundaries. Repulsive Coulombic forces between ions in combination with low number densities result in a plume that is effectively non-collisional. A more in-depth calculation demonstrating the non-collisionality of the plume is presented in

Section 4.4. Trajectory influences from molecule-surface collisions are minimized as charged electrodes are the only boundaries with which species can interact. The applied field exerted by said electrodes alongside the geometric configuration of the emitter often result in a steady-state plume distribution where zero particles, at any point along their trajectory, have collided with an electrode surface.

Thus, no modifications are made to the DSMC component of MPIC. Despite the lack of collisionality, the method is still employed to calculate the rare occasion where such collisions do occur. Additionally, various routines such as the particle tracker are utilized to implement other numerical methods, such as PIC described in the subsequent section.

4.3.1.2 Particle In Cell Method

The second numerical method implemented within MPIC is the PIC method. PIC is a kinetic method used to simulate the motion of charged particles under the influence of electrostatic forces from both applied and induced electric fields [125]. The method is well established and has been widely implemented in the study of low temperature plasmas [36, 86], including the plumes of electric propulsion systems [17, 52].

The PIC algorithm functions by discretely tracking the position and velocities of each charged particle, and uses these values to calculate macroscopic properties such as number and charge densities. These macroscopic quantities are used to solve continuous field equations, which dictate the long range forces acting on the particles and guiding their trajectories. More formally, the PIC method solves the equation of motion of N particles governed by Newton's Second Law and the Lorentz force

$$\frac{d\mathbf{x}_i}{dt} = \mathbf{v}_i, \tag{4.15}$$

$$\frac{d\mathbf{v}_i}{dt} = \frac{q_i}{m_i}\Big(\mathbf{E}(\mathbf{x}_i) + \mathbf{v}_i \times \mathbf{B}(\mathbf{x}_i)\Big), \tag{4.16}$$

for $i = 1, ..., N$, where $\mathbf{x}$ is the particle position vector, $\mathbf{v}$ is the particle velocity vector, $\mathbf{E}$ is

the electric field, and **B** is the magnetic field. As the plumes within an ILIS are subject to electrostatic fields, $\mathbf{B}(x_i) = 0$.

Computationally, Eqns. (4.15) and (4.16) are spatially discretized within a domain and are solved for the current density and field distributions, where those values are prescribed at each mesh node. At any given time step, a particle's continuous position is within the bounds of a mesh cell that is defined by the surrounding nodes. For a given particle within a cell, the force acting upon it is calculated in terms of the the field values at the surrounding cell nodes. Similar to DSMC, the PIC method implements a particle mover and each simulated particle can be representative of many physical particles. For this reason, a single module handles both of these routines within MPIC. For the PIC implementation, an additional Poisson solver is required to resolve the field equations of Eqns. (4.15) and (4.16).

MPIC was designed to study plume flows for conventional electric propulsion systems, such as Hall thrusters. These plumes are modeled as conventional quasineutral plasmas that consist of neutral species, ions, and electrons. A hybrid approach is implemented where neutral and charged species are modeled discretely and a fluid model is implemented for the electrons. The species are handled differently due to the difference in collision frequencies between electrons and ions, where the former is nominally several orders of magnitudes larger than the latter. As a result, electrons are more quickly able to 'normalize' with respect to ions and thus can be approximated as a fluid.

Originally within MPIC, the Boltzmann model was implemented as the electron fluid model and is used to calculate the plasma potential. The Boltzmann model is derived from the electron momentum equation given a number of assumptions. These include that the electron fluid is isothermal, collisionless, the electron pressure obeys the ideal gas law, and that any contributions from magnetic fields are negligible. Given these, the Boltzmann model takes the form

$$\phi = \phi_r + \frac{kT_{ref}}{q} \ln\left(n_e/n_r\right) \tag{4.17}$$

where ϕ is the electric potential ϕ_r is the reference potential, T_{ref} is the reference temperature, k is the Boltzmann constant, q is the elementary charge, n_e is the electron number density, and n_r is the reference number density.

This model was expanded upon by Boyd and Yim [17], where the electrons are modeled as a fluid using the conservation equations of mass, momentum, and energy. This higher fidelity model, denoted the Detailed model, is solved to obtain fundamental electron properties such as velocity, temperature, and plasma potential. Of the three conservation equations, the one of most considerable interest—for reasons that will soon become apparent—is the momentum conservation given by

$$\frac{\partial}{\partial t}(m_e n_e \mathbf{v}_e) + m_e n_e (\mathbf{v}_e \cdot \nabla)\mathbf{v}_e = -q n_e \nabla\phi - \nabla p_e + \mathbf{R}, \tag{4.18}$$

where m_e is the electron mass, $\mathbf{v}_e$ is the electron velocity, p_e is the electron pressure, and $\mathbf{R}$ is a friction term. The Detailed model assumes that electrons behave as an ideal gas where $p_e = n_e k T_e$, and that the friction term is equal to

$$\mathbf{R} = \frac{q n_e \mathbf{j}}{K}, \tag{4.19}$$

where j is the current density and K is the electrical conductivity. If the flow is assumed steady state, Eqn. (4.18) can be reformulated as a generalized Ohm's law

$$\mathbf{j} = K\left(-\nabla\phi + \frac{1}{q n_e}\nabla(n_e K T_e)\right). \tag{4.20}$$

For a given $n_e, \mathbf{v}_e, T_e$ the plasma potential is obtained by solving Eqn. (4.20) under the charge continuity condition

$$\nabla \cdot \mathbf{j} = 0. \tag{4.21}$$

Substituting Eqn. (4.20) into Eqn. (4.21) results in a generalized Poisson equation for the electron potential,

$$\nabla \cdot (K\nabla\phi) = \frac{k}{e}\Big(K\nabla^2 T_e + KT_e\nabla^2(\ln n_e) + K\nabla(\ln n_e)\cdot\nabla T_e + T_e\nabla K\cdot\nabla(\ln n_e) + \nabla K\cdot\nabla T_e\Big). \tag{4.22}$$

In summary, Eqns. (4.18) and (4.22) are used to calculate the plume potential using the Boltzmann and Detailed electron models, respectively, within the PIC implementation of MPIC. For an ILIS plume, only ion and neutral species are considered and quasineutrality is no longer applicable, yielding the models implemented within MPIC for determining the potential invalid in the context of a single emitter electrospray model.

To correct this, a non-quasineutral approach is taken where the generalized Poisson equation of Eqn. (4.22) is modified into a direct Poisson equation where the source term is locally calculated at every cell using the charge density values defined at the surrounding nodes. The result is a Poisson solver that is not derived from any electron model and is capable of solving for the electric field distribution within a singularly polarized plume.

4.3.2 Fragmentation Model

Plumes of ionic electrosprays are polydispersive and consist of various ions and ion clusters that vary in their degree of solvation. For the ionic liquid propellant used in this study, 1-Ethyl-3-methylimidazolium tetrafluoroborate (EMI-BF_4), these ion clusters take the form [EMI-BF_4]$_n$ [EMI^+] when operating in a positive emission mode, where n corresponds to the number of neutrals present in each molecule. Measurements have shown that ion beams typically consist of single ions/monomers ($n = 0$), dimers ($n = 1$), and trimers ($n = 2$). Although rare, larger ion clusters such as tetramers ($n = 3$) are occasionally observed as well [72]. The relative composition of each species is dependent on the ionic liquid used as well as the operating conditions of the thruster. For reference, time of flight mass spectrometry data of the AFET-2 thruster, operating at an emitter current of 200 μA and extractor voltage of

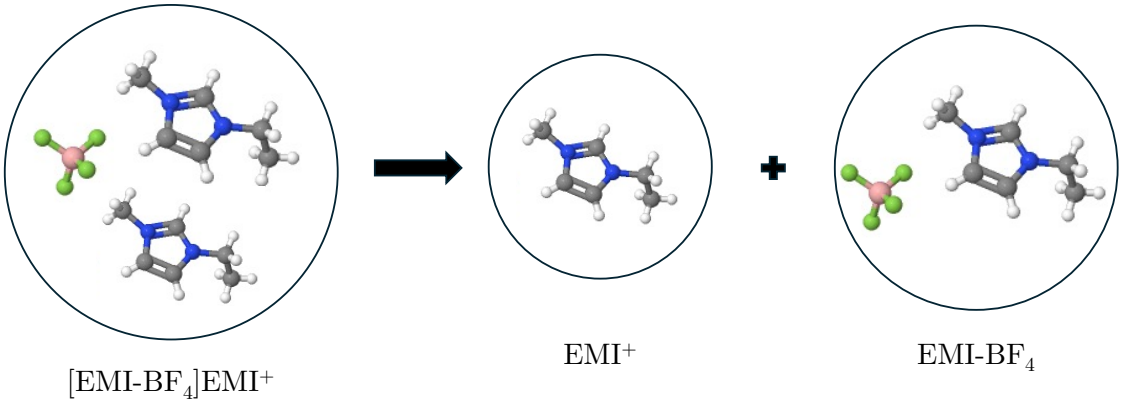

Figure 4.2: Fragmentation process of a positive EMI-BF_4 dimer.

1562 V, suggested a plume that consisted of approximately 45% monomers, 47% dimers, 6% trimers, and up to 2% tetramers [99].

Once evaporated, the ion clusters of electrospray beams are often unstable and may dissociate into smaller ion and neutral clusters. This dissociation process, known as fragmentation, increases the polydispersity of the ion beam and results in a decrease of overall electrospray thruster performance [81]. This is due to the fact that post-fragmented ions have lower kinetic energies than their pre-fragmented parent ions as a portion of the initial energy is lost to the neutral cluster. This results in a post-fragmented ion with a final kinetic energy less than that of the emitted potential and thus less efficient. Additionally, the neutral clusters, unaffected by the applied electric field, may contribute to other life limiting mechanisms such as pooling at the electrodes [124]. Therefore, it is imperative to consider the effects of fragmentation in an ionic electrospray plume model.

In this study, the single fragmentation process where [EMI-BF_4] [EMI^+] dissociates into an EMI^+ monomer and EMI-BF_4 neutral is considered. A schematic depicting this process is shown in Fig. 4.2. Measurements of the dissociation rates of dimers in the field-free region have been shown to follow the constant rate equation [95]

$$f_{dim}(t) = f_{dim,0} \exp\left(-t/\tau\right), \tag{4.23}$$

where f_{dim} is the current fraction of dissociated dimers, $f_{dim,0}$ is the current fraction of dimers that enter the field-free region, t is the simulation time, and τ is the inverse of the dissociation rate-constant, known as the mean lifetime. Fragmentation events upstream from the extractor in the acceleration region are not considered and will be suggested as an area of future study. As all emitted dimers eventually reach the field-free region, $f_{dim,0} = 1$. Using Eqn. (4.23), a distribution of fragmentation times can be formulated and is used as a basis to implement a fragmentation submodule into MPIC.

To do so, it must be first noted that previous work demonstrated a negligible velocity change in the post-fragmented species during the dissociation process [100]. This can be attributed to an average ion kinetic energy that is orders of magnitude larger than the solvation energy, allowing the negligence of higher-order effects from the fragmentation process itself. This allows for a simple numerical model where dimers, treated as point particles, are converted into monomer-neutral pairs at the site of fragmentation and are each assigned a velocity equal to that of the pre-event dimer. The process of determining whether a dissociation event occurs begins at particle injection, where each dimer is assigned a sampled fragmentation time relative to the global simulation time. The expression used to generate time samples is derived using the corresponding cumulative distribution function of Eqn. (4.23) and is given by

$$t_f = -\tau \ln\left(1 - R\right) + t_0, \tag{4.24}$$

where R is a random number sampled from the interval $[0, 1)$, t_0 is the global simulation time at particle injection, and t_f is the sampled fragmentation time. At every subsequent timestep, each dimer's assigned fragmentation time is compared against the global simulation time. If the simulation time is greater, then the condition for dissociation is met and the

dimer is numerically converted into a monomer-neutral pair.

4.3.3 Weak Coupling

The plume model is initialized by specifying the number density of each evaporated species at site of emission. In this study, only monomers and dimers of EMI-BF_4 when operating in a positive emission mode are considered. At each timestep, macroparticles, representations of real molecules, are injected into the computational domain at an inlet facet located at the emitter apex. Emitted ions are assumed to follow a Maxwellian distribution at 300 K, chosen as the approximate temperature when operated in room temperature and accounting for the slight self-heating contribution from Ohmic and viscous dissipation [83]. Upon injection the current fraction of each species is set to 50%, an approximation based off aforementioned time-of-flight mass spectrometry measurements by Natisin et al. [99].

The number densities of each monomer and dimer species at the injection site are found using the equations

$$\frac{1}{2}I_{\text{cap}} = A_e q\, n_m\, \hat{v}_m = A_e q\, n_d\, \hat{v}_d, \quad \text{where } \hat{v}_m = \sqrt{\frac{8k_BT}{\pi\, m_m}} \text{ and } \hat{v}_d = \sqrt{\frac{8k_BT}{\pi\, m_d}}, \tag{4.25}$$

where n_m is the monomer number density, n_d is the dimer number density, $\hat{v}_m$ is the monomer velocity, $\hat{v}_d$ is the dimer velocity, m_m is the monomer mass, and m_d is the dimer mass. Once injected, as mentioned in Subsection 4.3.1, the electric field and space charge densities are solved self-consistently at each node within the computational mesh using Poisson's equation and Newton's second law, where the force term is prescribed by the Lorentz equation,

$$-\nabla^2\phi = \frac{q}{\epsilon_0}(n_m + n_d), \tag{4.26}$$

$$\frac{d}{dt}(m_m\hat{v}_m + m_d\hat{v}_d) = q\hat{E}_v = -q\nabla\phi, \tag{4.27}$$

where ϕ is the electric potential.

4.4 Simulation Description

The simulations in this chapter are designed to closely replicate the operating conditions of experiments conducted by Natisin et al. [99], with select simulation parameters summarized in Table 4.1. A total of seven extraction voltages are simulated, where five are chosen as the focus of this study: 1426 V, 1562 V, 1639 V, 1748 V, and 1845 V. Specific parameters for each simulation case, including the particle count of each species and their corresponding number densities at the emission site, are presented in Table 4.2.

In each simulation, monomers and dimers are injected into the domain from a single cell located at the emitter apex, with each species contributing equally to the total current fraction. The number of particles generated at each timestep is a function of the source number density specified by the emission model, the timestep duration, and the size of the injection facet. The emission area of the injection cell is set to match the area used in the derivation of the reduced emission model, ensuring the correct number of ions are generated for the intended emission current. A macroparticle weighting of one is used, meaning each simulation particle is representative of a single physical molecule.

The simulations employ a timestep of 10 picoseconds, heuristically determined to resolve the ion trajectories near the emission site, over a total simulation time of 1.5 microseconds. For the fragmentation process, a mean lifetime of 0.1 microseconds is used, based on molecular dynamics simulations of EMI-BF_4 dimers conducted by Petro et al. [105].

Table 4.1: Global simulation parameters prescribed across all cases for the coupled continuum-kinetic single emitter simulations

Parameter	Value
Monomer Current Fraction	0.5
Dimer Current Fraction	0.5
Dimer Mean Lifetime	0.1 μs
Timestep	10 ps
Simulation Duration	1.5 μs
Macroparticle Weighting	1.0

Table 4.2: Initialization number densities of the monomer and dimer species for each applied voltage case across each coupled continuum-kinetic single emitter simulation. Current values are calculated from the steady-state species flux at the site of emission.

Voltage [V]	Current [nA]	Monomer Number Density [1/m^3]	Dimer Number Density [1/m^3]
1426	197	1.6×10^{21}	2.7×10^{21}
1562	366	3.0×10^{21}	5.0×10^{21}
1639	514	4.2×10^{21}	7.0×10^{21}
1703	678	5.5×10^{21}	9.3×10^{21}
1748	822	6.7×10^{21}	1.1×10^{22}
1790	980	8.0×10^{21}	1.3×10^{22}
1845	1229	1.0×10^{22}	1.7×10^{22}

4.4.1 Axisymmetric Mesh Criteria

Figure 4.3 presents the axisymmetric mesh used for the 1562 V simulation case, and is generally representative of the meshes utilized for the remaining cases. Figure 4.3a presents the mesh in the regime between the emitter and extraction electrode, where the symmetry is leveraged about the emitter centerline. Figure 4.3b illustrates a subset of Fig. 4.3a, highlighting the site of emission at the emitter apex. The boundary facet where monomer and dimer species are injected is denoted via the red arrow. To align with the initialization condition set by Eqn. (4.25), the injection facet length must be on the order of the characteristic emission radius, r^*. This can be approximated using the scaling laws derived in Section 4.2, where $r^* \sim q^6\gamma/4\pi^2\epsilon_0^3\Delta G^4$. Using prototypical values of $\gamma = 0.045$ N·m and $\Delta G = 0.8$ eV for EMI-BF_4, this would result in $r^* \sim 10^{-7}$ m.

Once injected, additional criteria must be considered for proper spatial resolution of the mesh. Grid size has shown to be influential on the electric field and extrusion physics of ILISs' [14]. Due to ILISs' similarities with plasmas, the Debye length is often used as a characteristic scale and metric determining to what extend a computational grid should be refined [3, 4, 33]. The Debye length is defined as the scale at which mobile charge carriers' electric field is screened in a charged solution,

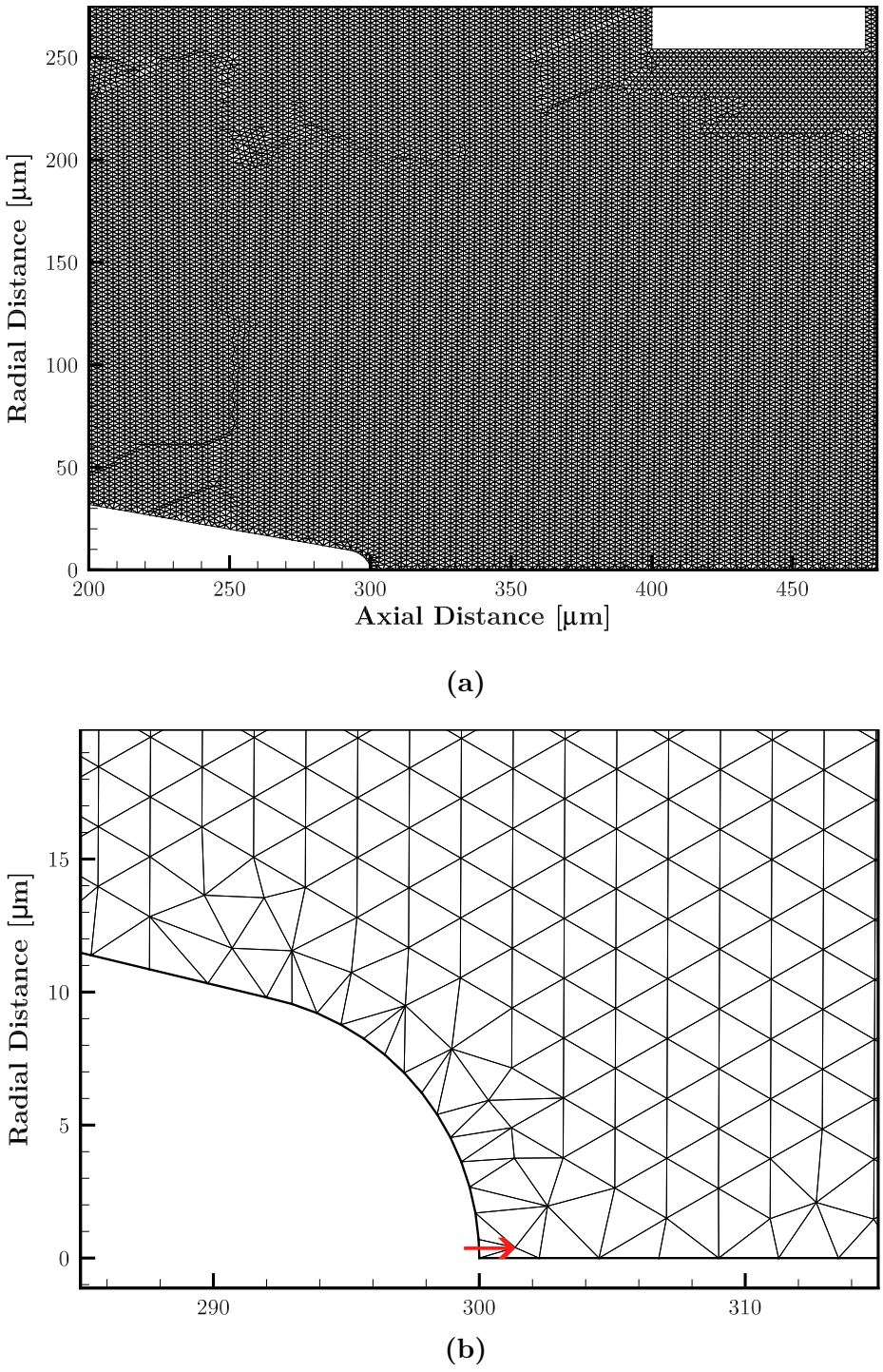

Figure 4.3: Axisymmetric mesh utilized for the 1562 V simulation case. The region between the emitter and extractor electrode is presented in (a) while the region immediately surrounding the site of emission is presented in (b). The red arrow in (b) denotes the facet where ion species are injected.

$$\lambda_D = \sqrt{\frac{\epsilon_0 k_B T}{nq^2}}. \tag{4.28}$$

It is particularly relevant in quasi-neutral plasmas where both positive and negative charges are present and can respond collectively to electric fields. An ILIS plume, however, by being singularly polar and breaking quasineutrality, lacks the rapid screening behavior characterized by the Debye length. The lack of any significant electron density with the plume (during positive emission) curtails any screening effect observed over the Debye length scale. As a result, electric fields and potential variations within the ion beam can persist over larger spatial scales than what the Debye scale would suggest. Thus, using the Debye length as a characteristic scale for refinement would likely result in a mesh that is overrefined, adding unnecessary computational cost on a given simulation.

Instead, the predominant factor in considering an appropriate mesh resolution lays within resolving gradients of the ion number densities. This gradient is likely on the order of the injection cell size near the emission site and quickly increases downstream as the ion beam expands. This motivates the mesh resolution chosen around the emission site shown in Fig. 4.3b, where the cell size is slightly larger but of comparable order to that of the injection cell. A relatively constant cell sizing is used throughout the computational domain to minimize the grid aspect ratio and thus minimize numerical instabilities within the Poisson solver. It has been shown that increased aspect ratios result in a higher condition number of the stiffness matrix [113], resulting in a higher likelihood of an ill-conditioned system that can result in numerical instability or loss of precision.

4.4.2 Collisionality

As discussed in Subsection 4.3.1.1, interparticle collisions are not a dominant factor in resolving the polydisperse plume. To demonstrate this, the mean free path for interparticle collisions is approximated using the injection ion number densities of the highest extraction

voltage case simulated, 1845 V. The ion densities within this emission region are the highest relative to any other axial location within the ILIS plume due to Coulombic expansion of the beam and the radial component of the electric field acting away from the centerline axis. As a result, the injection ion number density of the 1845 V case would correspond to the smallest collisional mean free path at any point within the domain across all simulation cases considered.

To calculate this mean free path, the plume is approximated as a gas composed of hard sphere particles in thermal equilibrium. Under these conditions the mean free path of dimers when considering dimer-dimer and dimer-monomer collisions is given by [16]

$$\lambda_{dim} = \left[n_{dim}\sigma_{dd}\sqrt{2} + n_{mon}\sigma_{dm}\sqrt{1 + \frac{m_{dim}}{m_{mon}}} \right]^{-1}, \tag{4.29}$$

where λ_{dim} is the dimer mean free path, n_{dim} and n_{mon} are the number density of the dimer and monomer species, respectively, m_{dim} and m_{mon} are the masses of the dimer and monomer species, respectively, σ_{dd} is the collision cross section of dimer-dimer collisions, and σ_{dm} is the collision cross section of dimer-monomer collisions. For hard-sphere collisions between a single species A, the collision cross section is given by

$$\sigma_{AA} = \pi d^2, \tag{4.30}$$

where d is the particle diameter. For hard-sphere collisions between differing particle species A and B, the collision cross section is

$$\sigma_{AB} = \frac{\pi}{4}(d_A + d_B)^2. \tag{4.31}$$

The diameter of an EMI^+ monomer is on the order of 7.6 $\mathring{A}$ [4]. The diameter of a [EMI-BF_4]EMI^+ dimer is approximated as a combination of two EMI^+ monomers and a single BF_4 monomer, where the latter is on the order of 5.2 $\mathring{A}$. These values result in dimer-dimer and dimer-monomer collision cross sections of approximately 1.3×10^{-19} m^2 and 0.6 $\times10^{-19}$

m^2, respectively. Using mass values of $m_{dim} = 309$ g/mol and $m_{mon} = 111$ g/mol and the 1845 V injection number densities of $n_{dim} = 1.7 \times 10^{22}$ m^{-3} and $n_{mon} = 1.0 \times 10^{22}$ m^{-3}, the dimer mean free path at the injection site is $\lambda_{dim} \sim 10^{-6}$ m. In comparison, the characteristic emission radius, r^*, is on the order of $r^* \sim 10^{-7}$ m. Thus, at its minimum point across each case, the collision mean free path is approximately an order of magnitude larger than the length scale at the site of emission, indicating that inter-particle collisions are not a governing factor within the plume dynamics. This scale differential is likely an underestimation as the influence of Coulombic repulsion is not accounted for in the collisional cross section calculations.

4.5 Plume Characteristics

4.5.1 Emission Current

Figure 4.4 illustrates the electric field streamlines and potential contours between the emitter and extractor grid for the 1562 V case, obtained by the EHD solver. Note the potentials are negative as the emitter is operating in a positive emission mode. Between the electrodes, the potential is unexpectedly monotonic while the field strength increases about the emitter tip due to its morphology and surface charge density at the emission site. From this solution, the normal component of the electric field across the meniscus is extracted and used as input for the emission model to approximate the total emission current. Figure 4.5 presents the resulting field distributions across the interface for all simulated voltages. A log scale is utilized on the y-axis to better differentiate between electric field distributions. Each extraction voltage exhibits a similar radial distribution until they converge towards the centerline, where they align to the same order as demonstrated in the inset.

To compare simulated emission currents with experimental measurements from the AFET-2 thruster, the simulated single-emitter currents are linearly scaled by the total number of emitters (576) employed in the experimental configuration. Fig. 4.6 presents a

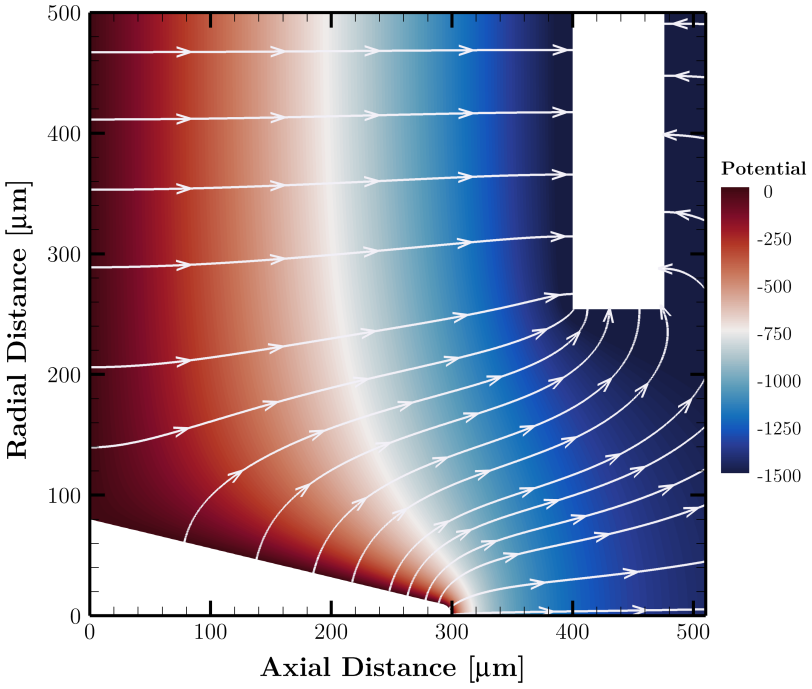

Figure 4.4: Potential contour and electric field streamlines within the extraction region for the 1562 V simulation case.

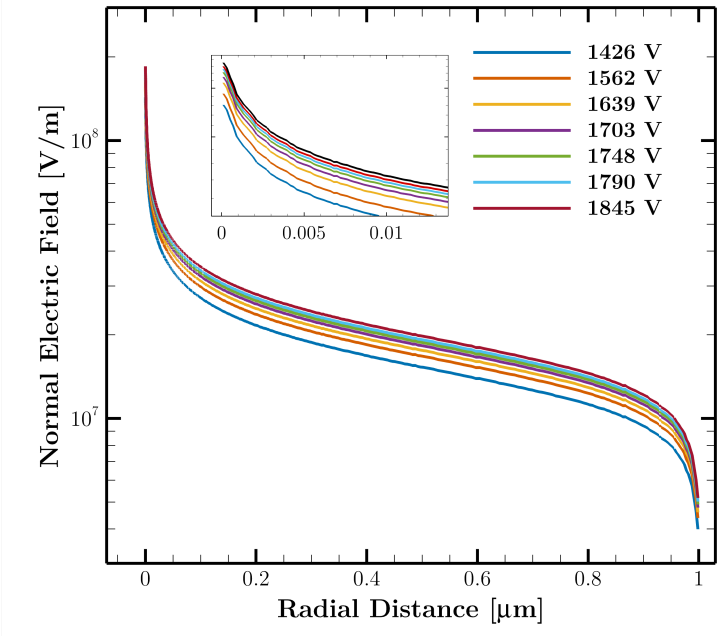

Figure 4.5: Vacuum electric field distribution normal to the meniscus across simulated extractor voltages. The inset provides a detailed view of the field distributions near the meniscus apex.

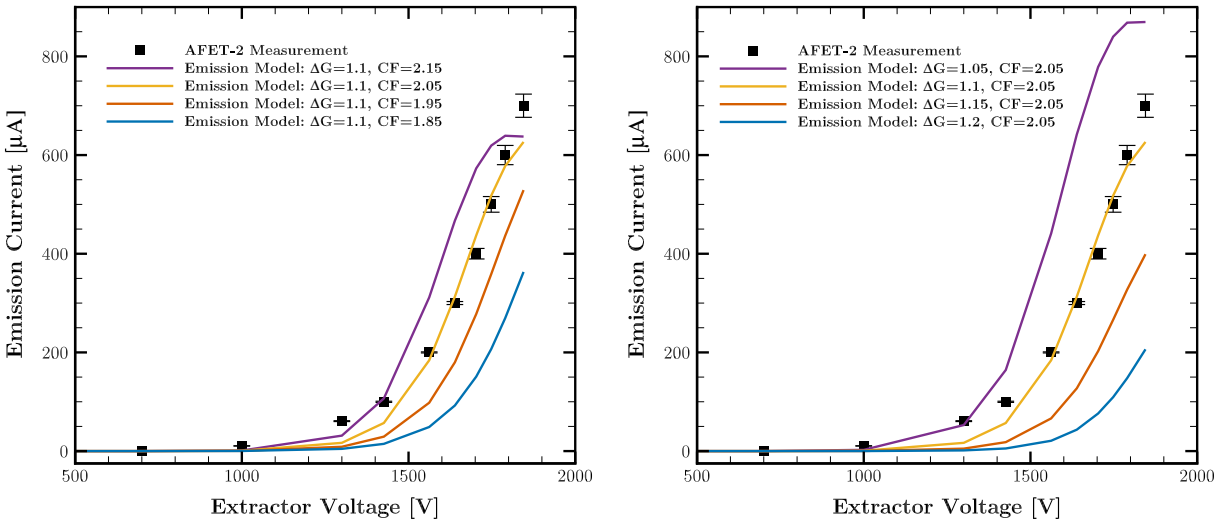

Figure 4.6: Linearly extrapolated emitter source currents calculated by the ionic emission model versus AFET-2 measurements [99] as a function of extractor voltage. In (a), the emission model is calculated at various calibration factors C_f at a fixed activation energy for evaporation ΔG and (b) showcases the model at various values of ΔG at a fixed C_f.

comparison between measured emission currents and various calculations from the emission model, illustrating the sensitivity of the model outputs to both numerical and physical factors. Specifically, numerical sensitivity is demonstrated in Fig. 4.6a through variation in the scaling parameter C_f at a fixed activation energy for evaporation ΔG, and physical sensitivity is illustrated in Fig. 4.6a by varying ΔG at a fixed value of C_f. The best agreement with experimental measurements were found at $C_f \approx 2.05$. It should be noted from Fig. 4.6a that increasing the numerical scaling parameter does not result in exponential growth in emission current; rather, at $C_f = 2.15$, the total emission current begins to plateau with increasing extraction voltage. This plateau behavior aligns with previous observations [30, 47] suggesting that, in this meniscus size regime relative to the contact radius, the current initially varies linearly with the electric field but eventually curtailed by the finite conductivity of

the propellant. Deviations observed between model predictions and experimental data at higher voltages in Fig. 4.6a may also be attributed to physical effects such as the emergence of multiple emission sites per emitter, which have been experimentally observed in arrays operated at elevated voltages [23, 39, 55].

In Fig. 4.6b, the emission model sensitivity to perturbations in the activation energy for evaporation ΔG is presented. From the scaling law analysis in Section 4.2, it can be shown that $I^* \sim (\Delta G)^6$, illustrating that even minor variations of the activation energy can significantly influence emission characteristics. The value of ΔG was chosen using the critical electric field strength E^* that follows $E^* \approx 4\pi\epsilon_0(\Delta G)^2/q^3$ [65]. Significant emission for the AFET-2 was observed beginning at approximately 1300-1400 V, which from Fig. 4.5 corresponds to an estimated field strength of slightly above 10^8 V/m for EMI-BF_4. This results in a value of $\Delta G \approx 1.1$ eV used in emission calculations that were later employed in the initialization of the downstream plume model.

4.5.2 Thrust

Consideration of the plume begins with the number density contours of the monomer, dimer, and neutral species from the 1562 V operational case, presented in Fig. 4.7. The monomer and dimer contours exhibit comparable particle distributions near the emitter, as expected by the fixed species ratio set at initialization. In contrast, a significant neutral population is not introduced into the plume until further downstream in the field-free region. This observation aligns with the mean lifetime value calculated by Ref. [105], as the fragmentation model does not assume a specific location for dissociation events. The distinction between the neutral and non-neutral densities can also be attributed to the fact that the neutral trajectories are set at the site of fragmentation, where they are subsequently unaltered as the plume is noncollisional and they are field-agnostic.

Emission thrust is calculated for each extractor voltage at several downstream axial distances spaced 50 microns apart, with the maximum distance considered being 900 microns,

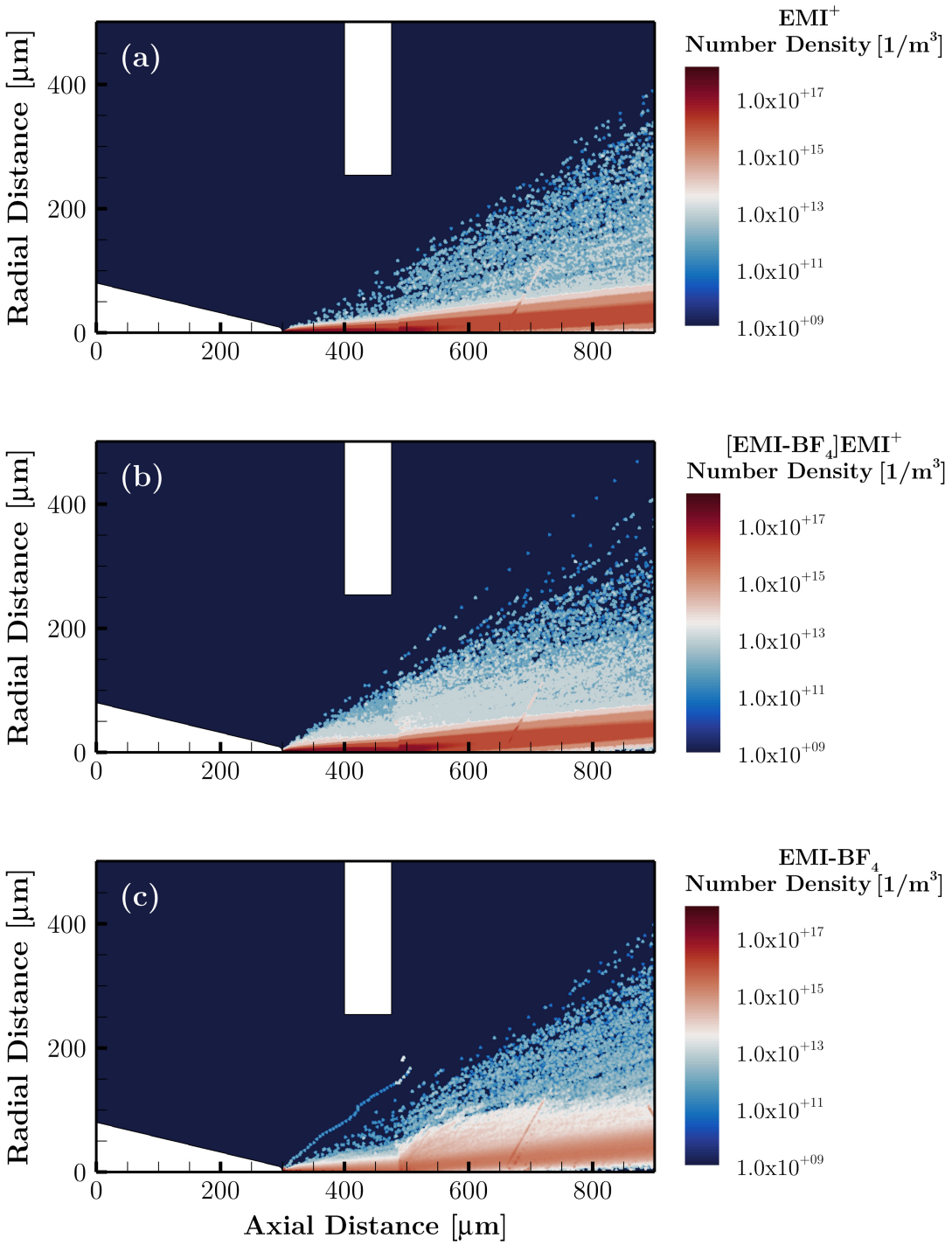

Figure 4.7: Number density contours of the (a) monomer, (b) dimer, and (c) neutral species for the 1562 V simulation case.

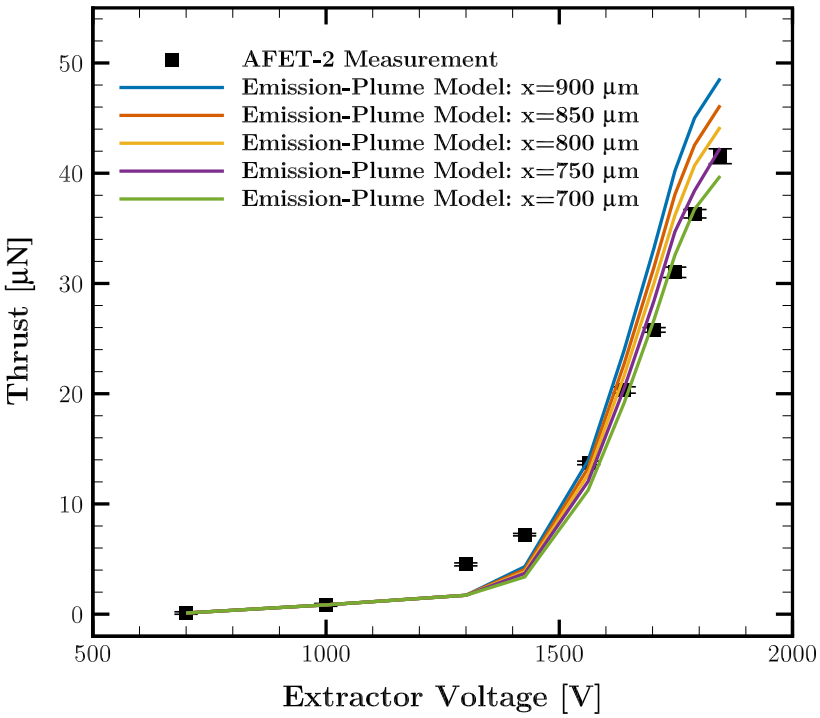

Figure 4.8: Linearly extrapolated emission thrusts calculated at select axial distances versus AFET-2 measurements [99] as a function of extractor voltage.

chosen to mitigate the influence of boundary-induced numerical effects. Similar to the emission current comparisons, single emitter thrust calculations are linearly extrapolated by the array size used for the AFET-2 and compared against experimental thrust measurements in Fig. 4.8, where the calibration factor used is $C_f = 2.05$. The axial distances of the exit planes used to calculate thrust are less than the centimeter-scale distances at which AFET-2 thrust measurements were experimentally made due to limitations in computational domain sizing arising from computational cost. Despite these differences, a general agreement in the trend is observed between simulated thrust calculations and measurements. Increasing the axial plane distance generally results in higher calculated thrust values, as thrust is proportional to the square of species velocity, and at these distances, the emitted species are still accelerating due to their initial momentum from the evaporation process. Once

significantly far from this acceleration region, emitted and fragmented species velocities are expected to plateau and possibly decrease depending on the background pressure. At lower extraction voltages, the underestimation of thrust by the model can be partially attributed to the corresponding under-prediction of emission current observed in Fig. 4.6. Conversely, at higher extraction voltages, plume simulations are found to overestimate thrust values at axial distances greater than 700 microns. Outside of the discrepancy associated with the different distances at which the thrust is compared, one possible reason that the model overestimates measurements at higher voltages may be due to inaccuracies in the assumed current fractions of monomers and dimers. Specifically, deviations from equal current fractions, especially at higher potential gradients, could result in an incorrect mass distribution within the plume that acts to overestimate the thrust.

4.5.3 Beam Divergence

Spatial characterization of the plume is also considered. Beam intensity and current density distributions are calculated at a radial distance of 250 microns from the emitter tip. The beam intensity, defined as the number of particles crossing the radial boundary per unit area and time, is normalized and plotted against the divergence angle for all simulation cases, presented in Fig. 4.9. The beam intensity distributions are normalized such that the total integral of the intensity over all divergence angles is equal to one, ensuring that each curve represents the relative intensity distribution as a function of divergence angle. For each distribution, values are sampled during the final 0.5 μs of simulation when the plume has reached steady-state and an angular discretization of 1° is used. To quantify an effective divergence angle, the ion count is integrated along the radial boundary and solved for the angle at which 80% and 99% of all species have crossed, presented in Table 4.3. The resulting plume divergences exhibit a negligible dependence on the extractor voltage, aligning with simulations conducted by Petro et al. [105].

Experimentally, plume distributions in electrosprays are known to exhibit super-

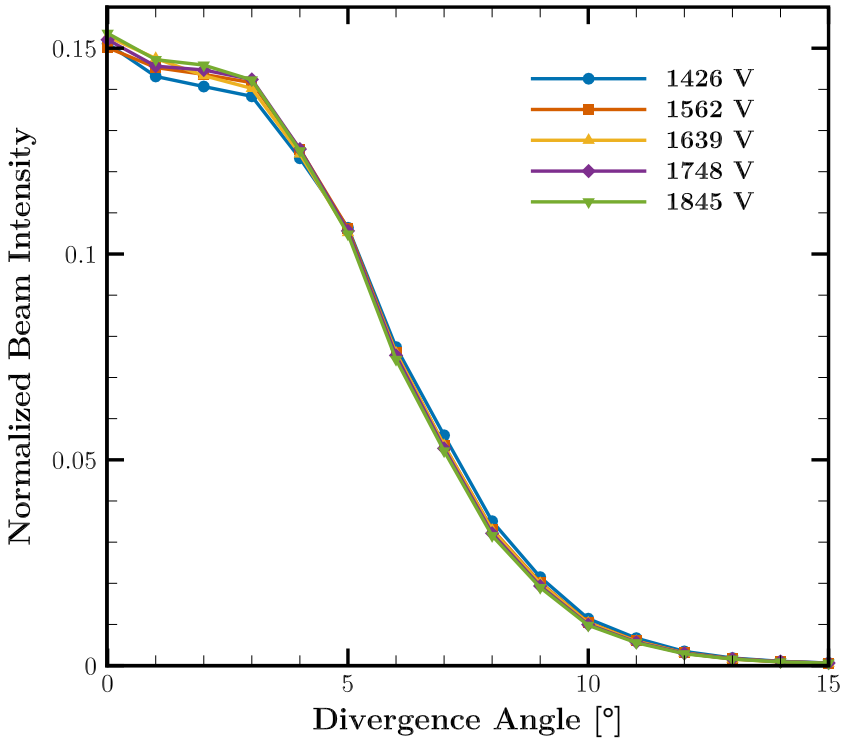

Figure 4.9: Divergence angle versus normalized beam intensity across extractor voltages 250 μm from the emitter.

Gaussian distributions. Following the model of Thuppul et al. [124], the current density and intensity distributions are parameterized using a super-Gaussian profile,

Table 4.3: Divergence angles for the two confidence intervals at 250 μm from the emitter.

Voltage [V]	80%	99%
1426	6.0°	11°
1562	6.0°	11°
1639	6.0°	11°
1703	6.0°	11°
1748	6.0°	11°
1845	6.0°	11°

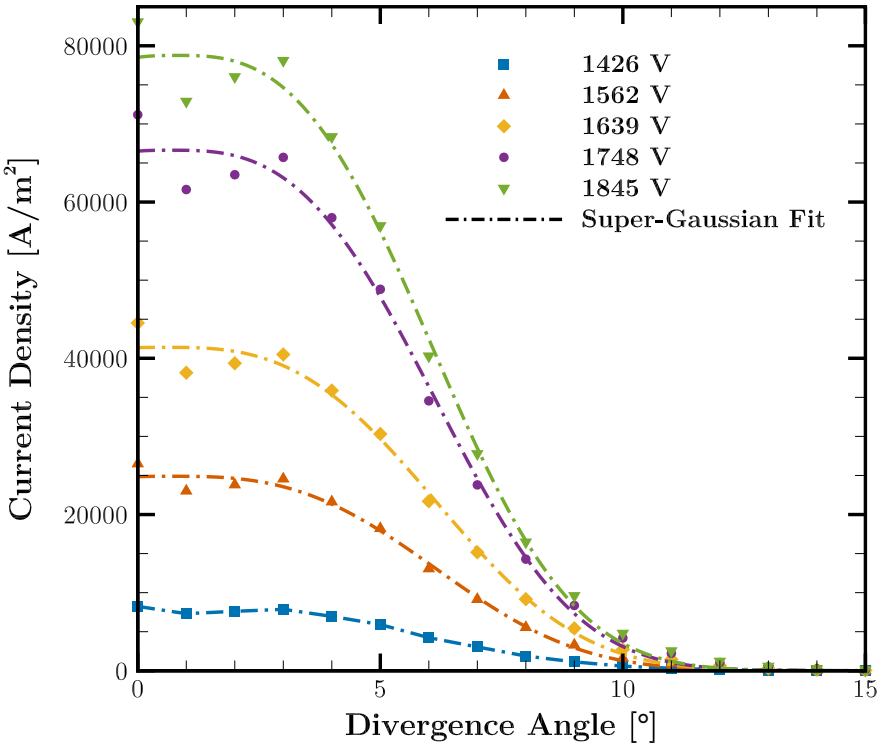

Figure 4.10: Divergence angle versus current density across extractor voltages at 250 μm from the emitter.

$$f(\theta) = \alpha \exp\left[-\left(\frac{(\theta-\theta_t)^2}{\theta_0^2}\right)^{\eta}\right], \tag{4.32}$$

where α is the plume magnitude, θ_t is the degree at which the angle is tilted away from the central axis, θ_0 is the plume width, and η is the plume sharpness. At $\eta = 1$ the distribution is a perfect Gaussian, where as values greater than one correspond to flatter profiles near the central axis and values less than one correspond to sharper profiles. Values for α, θ_0, and η for a given extractor voltage are curve-fit to the numerical data via Nelder-Mead optimization, with $\theta_t = 0$ due to the axisymmetry of the simulations. The current density distribution as a function of the divergence angle for each extractor voltage, alongside their respective super-Gaussian fits, are presented in Fig. 4.10.

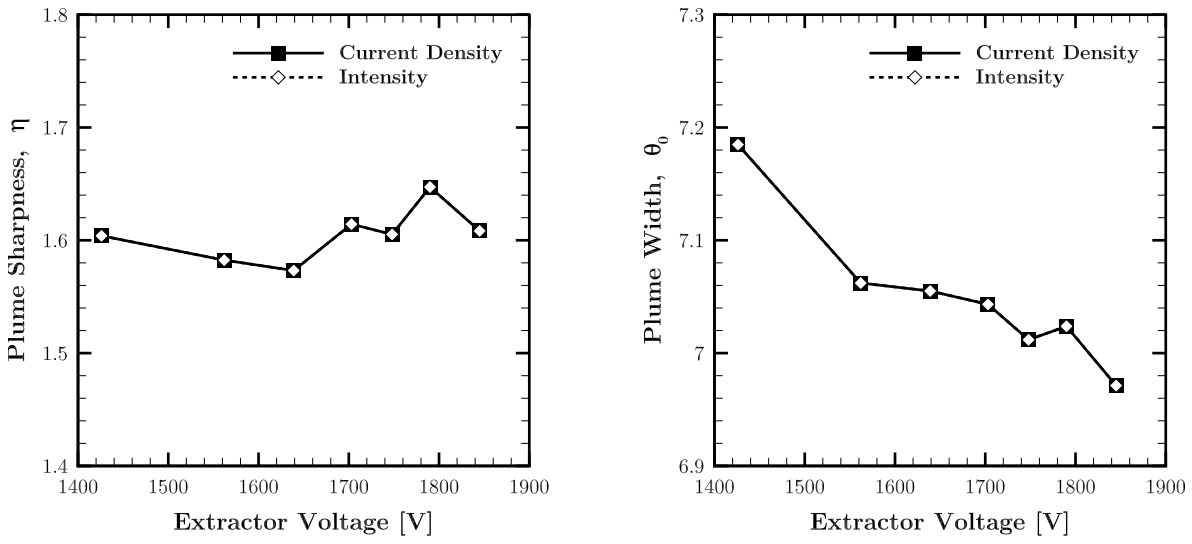

Figure 4.11: Super-Gaussian plume (a) sharpness and (b) width parameters of 250 μm current density and intensity distributions calculated across extraction voltages.

Parameterization of the radial distributions enables direct comparison of plume characteristics across simulation cases. In Fig. 4.11, the sharpness and width parameters are presented for the current density and intensity distributions calculated at a radial distance of 250 microns across each simulated voltage. Figure 4.11a shows the sharpness parameter remains relatively constant across all voltages at approximately 1.6. Figure 4.11b illustrates a decreasing trend in plume width with increasing extractor voltage, exhibiting the largest decrease between the 1426 V and 1845 V simulations. This reduction in plume width is consistent with increased focusing of ions at higher extraction voltages. However, as discussed in Subsection 4.5.3, this reduction is not significant enough to meaningfully alter the overall beam divergence angle. Furthermore, no discernible difference in sharpness and width is observed between the current density and intensity distributions, suggesting that neutral species do not significantly influence the macroscopic spatial characteristics of the plume in this operational and geometric regime.

4.6 Conclusions

In this chapter, a novel multiscale model was presented for a single-emitter ionic electrospray source. The model integrates high-fidelity EHD meniscus simulations with a semi-empirical emission model and a particle-in-cell-based plume model that incorporates field-free fragmentation of dimers. After calibration against experimental measurements from the AFET-2 thruster, the model demonstrated qualitative agreement with both spatially-averaged emission currents and thrust values. Spatial characteristics of the beam were calculated using a super-Gaussian parameterization, quantifying how attributes such as the plume sharpness, width, and amplitude evolve across a range of applied voltages.

Single-emitter simulations using operational conditions similar to those used by the AFET-2 demonstrated that the emission current and thrust follow expected trends with increasing extraction voltage, validating the hybrid modeling approach. The plume analysis revealed that beam divergence remains relatively constant across operational voltages, with 80% of species confined within a 6° angle and 99% within 11° from the central axis. The super-Gaussian parameterization showed a consistent sharpness parameter across all voltages, while the plume width decreased with increasing voltage due to enhanced ion focusing. It was found that neutral species generated through fragmentation did not significantly alter the macroscopic spatial characteristics of the plume in the operational and geometric regimes studied. The observed deviations between model predictions and experimental measurements at higher extraction voltages highlight potential effects of inter-emitter coupling and multiple emission sites per emitter that warrant further investigation.

The flexibility of the semi-empirical emission model suggests that it could be adapted to model other electrospray configurations, capturing empirical influences not explicitly represented in more detailed EHD meniscus models. Additionally, the end-to-end computational framework developed in this study provides a robust platform for parameter-space explorations and sensitivity analyses. Explored further in the subsequent chapter, this framework

serves as a valuable tool for subsequent investigations into life-limiting mechanisms such as electrode overspray and off-axis emission, supporting enhanced reliability and performance predictions for next-generation ionic electrospray propulsion systems.

Chapter 5

Surrogate-Based Design Space Exploration

In the previous chapter, a coupled emission and kinetic model was developed and implemented to simulate the end-to-end behavior of a single-emitter ionic electrospray thruster. This framework integrated detailed phenomena such as fragmentation, inlet conditions, and spatial plume characteristics to provide a comprehensive representation of ionic emission and downstream dynamics. The results from these simulations emphasized the sensitivity of plume characteristics to upstream conditions, providing a foundation for further studies on mitigating failure modes in electrospray thrusters.

Building on this framework, the current chapter explores the impact of operational and geometric perturbations on plume characteristics to address critical challenges in thruster design. Prior research has demonstrated that minor deviations in manufacturing tolerances or operational parameters can significantly alter plume morphology, exacerbating life-limiting mechanisms such as grid impingement [123, 124]. By leveraging the high-fidelity single-emitter model developed in Chapter 4, this chapter seeks to quantify the sensitivity of plume characteristics to these perturbations and identify tolerances that can enhance the reliability and performance of electrospray thrusters.

The investigation begins in Section 5.1 with a detailed axisymmetric analysis of how variations in extractor voltage and tip-to-extractor distance influence key plume characteristics, such as plume width, sharpness, and tilt. Using the axisymmetric simulation framework from Chapter 4, this study systematically maps the sensitivity of plume parameters across

a defined design space. These insights are then extended into a three-dimensional domain in Section 5.2, allowing for the exploration of non-axisymmetric geometric perturbations. In particular, translational and rotational misalignments of the emitter with respect to the extractor are considered, capturing the effects of manufacturing imperfections and assembly variability.

5.1 Axisymmetric Study

The combined emission and plume model presented in Chapter 4 is used to simulate the effects of varying the tip to extractor distance and extractor potential on downstream spatial plume characteristics. These characteristics are obtained from the super-Gaussian parameterization of radial plume cross section distributions of current density and beam intensity.

To characterize the influence of these geometric and operational conditions on the plume state, an axisymmetric parameter space is selected such that the plume is studied across a range of potentials and distances. The potential range is the same as that explored in Chapter 3, $\phi \in [1426\text{ V} - 1845\text{ V}]$, and tip to extractor distances ranging from flush with the emitter to 100 microns, $d \in [0\ \mu\text{m} - 100\ \mu\text{m}]$.

5.1.1 Surrogate Model Formulation

Understanding how the plume morphology evolves within this parameter space would ideally be accomplished through a refined discretization of each input variable, where the resultant grid of inputs is each evaluated as a unique simulation in the full end-to-end single emitter model. However, evaluation of the numerical model across each permutation of initial conditions would be prohibitive due to the computational cost. To mitigate this, a lower fidelity surrogate model is implemented as an efficient means of approximating output from the higher fidelity single emitter model.

Surrogate models, also known as response surface models, are nominally simple analytic

models that represent the functional behavior of more complex systems [85]. These models are built via regression training on underlying data of the original model at discrete sampling points. Although surrogate model construction still necessitates sampling of the original numerical model, the number of samples required to build a sufficiently accurate surrogate is often less than what would be required to resolve the original model directly. The result is a model that is significantly faster to sample than the original numerical model, while still retaining a sufficient level of accuracy away from the discrete evaluation points that were used to train it. Lastly, surrogate models are especially useful for design space exploration, optimization, and sensitivity analyses as the construction of a continuous analytic function over discrete data enables straightforward computation of their gradients.

To initialize each surrogate, the original single emitter model must be sampled across the axisymmetric parameter space. A full factorial sampling method is implemented where each input dimension is discretized and the numerical model is evaluated at all combinations of the resulting sample grid. Although this sampling plan is inefficient as the evaluation points required scale exponentially with the number of input parameters, it is sufficient for this use case due to the low dimensionality of the input space. The tip-electrode distance is discretized at every 20 microns, $d \in [0\ \mu\text{m}, 20\ \mu\text{m}, 40\ \mu\text{m}, 60\ \mu\text{m}, 80\ \mu\text{m}, 100\ \mu\text{m}]$, and the extractor voltages are discretized in accordance to the voltages used by Natisin et al. [99] between 1426 V and 1845 V, $V \in [1426\ \text{V}, 1562\ \text{V}, 1639\ \text{V}, 1748\ \text{V}, 1845\ \text{V}]$. The result is a sampling grid that requires 30 evaluation points of the single emitter numerical model.

At each evaluation point, a full two-dimensional axisymmetric single emitter simulation is conducted using the same computational domain and grid characteristics described in Chapter 4. In each case, radial cross sections of the current density and beam intensity are taken at a fixed distance 250 microns downstream from the emitter. Similar to Chapter 4, current density and beam intensity are chosen to quantify various spatial characteristics of the plume, where the latter incorporates the influence of neutral species while the former does not. From each distribution, a super-Gaussian parameterization, Eqn. (4.32), is fit to obtain

the characteristics of interest: width θ_0, sharpness η, and beam tilt θ_t. Unlike in Chapter 4, beam tilt is not assumed zero as variations in the tip-extractor distance—especially at lower values—is expected to alter the radial electric field component such that off-axis emission is plausible. Within a two-dimensional axisymmetric domain, this off-axis emission would be physically representative of an annular beam distribution.

After sampling the single emitter model at each evaluation point, the resultant data used to construct the surrogate model can be expressed as

$$\left(\mathbf{x}^{(i)}, \mathbf{f}^{(i)}\right), \tag{5.1}$$

where $\mathbf{x}^{(i)}$ is the input vector corresponding to a sampling point, $\mathbf{x}^{(i)} \in (\hat{d}^{(i)}, \hat{V}^{(i)})$, and $\mathbf{f}^{(i)}$ is the output vector of characteristics from each plume distribution. $\hat{d}^{(i)}$ and $\hat{V}^{(i)}$ represent the non-dimensional tip-extractor distance and extractor voltages, where each quantity is normalized by their maximum values of 100 μm and 1845 V, respectively. To construct a surrogate model from the dataset of Eqn. (5.1), a set of basis functions must be chosen that dictate the form of the model. Once set, the coefficients of that model must be solved such that the surrogate is sufficiently representative of the sampled data. For this study, a linear regression model is selected and takes the form

$$\hat{f} = \mathbf{w}^{\mathbf{T}}\boldsymbol{\psi}(x) = \sum_i w_i \psi_i(x), \tag{5.2}$$

where $\hat{f}$ represents the approximating function of the single emitter model, w is the vector of coefficients or weights, and $\boldsymbol{\psi}$ is the vector of basis functions. For the input vectors considered in Eqn. (5.1), a two-dimensional, second-order polynomial is chosen as the set of basis functions, $\boldsymbol{\psi} = [1, \hat{d}, \hat{V}, \hat{d}^2, \hat{V}^2, \hat{V}\hat{d}]$. This set corresponds to a weight vector $\mathbf{w} = [c_0, c_1, c_2, c_3, c_4, c_5]$ with a total of six coefficients. The resultant surrogate model to represent the functional relationship between extractor voltages and tip-extractor distances (inputs) and each plume characteristic of interest (outputs) is then

$$\hat{f}_j^k(\hat{d}, \hat{V}) = c_0 + c_1\hat{d} + c_2\hat{V} + c_3\hat{d}^2 + c_4\hat{V}^2 + c_5\hat{V}\hat{d}, \tag{5.3}$$

where $\hat{f}_j^k$ represents the model for the characteristic k for a given plume distribution j.

The coefficients of Eqn. (5.3) are determined such that the error between the approximated function values, $\hat{f}$, and the single emitter model values, $f^{(i)}$, are minimized. The form of this minimization problem is,

$$\underset{w}{\text{minimize}} \quad \sum_i \left(\hat{f}\left(w; x^{(i)}\right) - f^{(i)}\right)^2, \tag{5.4}$$

where the solution is a well-established optimization problem known as the least squared solution [85]. As such, a general analytical solution for the weights is also known,

$$w = (\Psi^{\mathbf{T}}\Psi)^{-1}\Psi^{\mathbf{T}}f, \tag{5.5}$$

where the matrix Ψ is defined as

$$\Psi = \begin{bmatrix} — & \psi(x^{(1)})^{\mathbf{T}} & — \\ — & \psi(x^{(2)})^{\mathbf{T}} & — \\ & \vdots & \\ — & \psi(x^{(n_s)})^{\mathbf{T}} & — \end{bmatrix} \tag{5.6}$$

and is of the size $(n_s \times n_w)$, where n_s is the number of samples taken of the original model and n_w is the number of coefficients in w for the surrogate model. For the system to be well determined, Eqn. (5.5) must satisfy the condition $n_s \geq n_w$. In the case of Eqn. (5.5), $n_s = 30$ and $n_w = 6$, ensuring that enough data is sampled to properly fit the surrogate.

5.1.2 Geometric and Operational Space Exploration

The coefficients of the surrogate model in Eqn. (5.3) are solved using least squares minimization and are presented in Table 5.1 for each plume characteristic across each

distribution type. Using the coefficients of Table 5.1, the dependencies of each characteristic on the tip-electrode distance and extractor voltages are shown for the current density in Fig. 5.1 and for the beam intensity in Fig. 5.2.

From the surrogate model fitting, several observations can be made on the dependence of how plume characteristics respond to variances of this particular design space. Generally, regardless of the distribution type, it can be seen via Table 5.1 that each characteristic is strongly dependent on both design variables. The data also suggests a stronger sensitivity to the tip-extractor distance relative to the extractor voltages across characteristics. Sensitivities of plume characteristics are further described in Subsection 5.1.3.

In Fig. 5.1a, one can observe an overall decrease in the plume width (and thus beam divergence) with increasing extractor voltage. This beam narrowing occurs despite the fact that higher extractor voltages result in increased emitter currents and thus a higher space charge density, where one may expect an increase in beam spreading due to the higher Coulombic forces between evaporated ions. Despite this larger Coulombic repulsion, the inverse trend observed in the data is corroborated in the literature [105, 114], suggesting that beam morphologies are largely determined by species inertia and the electric field streamlines. In other terms, the inertial and applied forces acting largely axially on the emitted species are dominant with respect to the radial forces applied by Coulombic repulsion. As the ratio

Table 5.1: Surrogate model parameter coefficients for each plume characteristic across distribution types for the axisymmetric, two-dimensional case.

Current Density						
Plume Characteristic, $\hat{f}^k_{cd}(\hat{d},\hat{V})$	$\mathbf{c_0}$	$\mathbf{c_1}$ $[\hat{d}]$	$\mathbf{c_2}$ $[\hat{V}]$	$\mathbf{c_3}$ $[\hat{d}^2]$	$\mathbf{c_4}$ $[\hat{V}^2]$	$\mathbf{c_5}$ $[\hat{d}\hat{V}]$
Width, θ_0	4.02	4.33	-0.61	-0.91	2.84e-3	-1.05
Sharpness, η	0.32	-0.50	1.22	1.13	-0.77	-0.03
Tilt, θ_t	6.13	4.16	-2.86	-10.11	0.56	2.53
Beam Intensity						
Plume Characteristic, $\hat{f}^k_{bi}(\hat{d},\hat{V})$	$\mathbf{c_0}$	$\mathbf{c_1}$ $[\hat{d}]$	$\mathbf{c_2}$ $[\hat{V}]$	$\mathbf{c_3}$ $[\hat{d}^2]$	$\mathbf{c_4}$ $[\hat{V}^2]$	$\mathbf{c_5}$ $[\hat{d}\hat{V}]$
Width, θ_0	2.60	4.02	2.72	-0.58	-1.79	-1.11
Sharpness, η	0.37	-0.56	1.06	1.01	-0.67	0.10
Tilt, θ_t	7.79	4.10	-6.27	-10.51	2.37	2.89

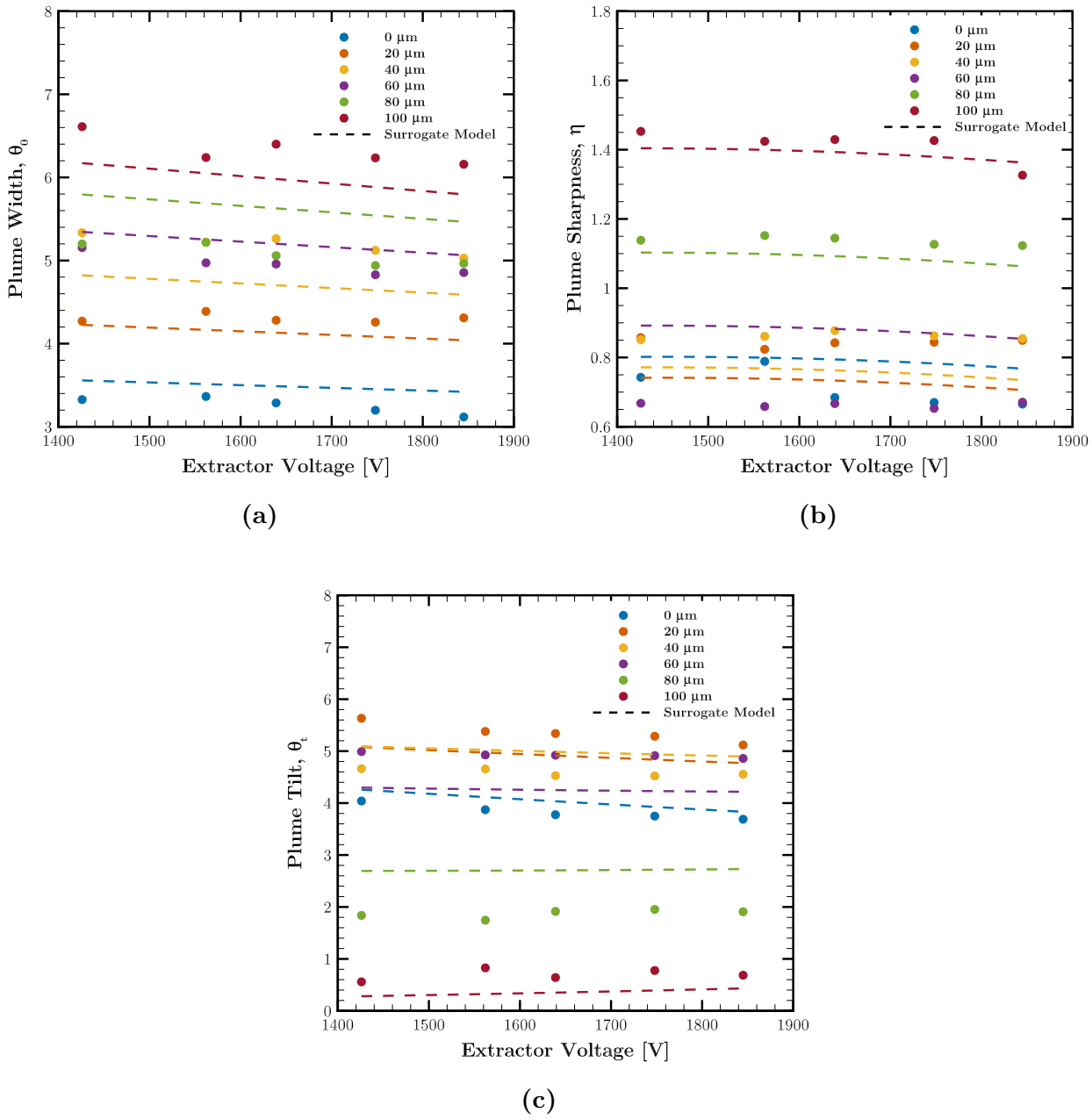

Figure 5.1: Sampled single-emitter model data and surrogate model fits for (a) plume width, (b) plume sharpness, and (c) plume tilt of current density for the axisymmetric study. Characterization parameters are calculated at a radial cross section of 250 µm downstream from the emitter tip.

of these axial and radial forces increase with larger extractor potentials, a smaller proportion of the beam acts to increase its divergence.

The phenomena of beam tightening is apparent across tip-electrode distances as well, with the extent at which this tightening occurs slightly decreasing with lower tip-extractor distances. The decrease in sensitivity likely corresponds to how the radial field component affects the beam spread at various axial distances (corresponding to the tip-electrode distances). At larger tip-extractor distances, the radial field component has more influence (integrated load) over the span of an ion's trajectory, and is thus more prominent at higher extractor potentials. This is in contrast to lower tip-electrode distances where the lesser component of the ion trajectory is influenced by the radial field component as they are more-quickly advected downstream away from the extractor's influence in accordance to the inverse square law.

In Fig. 5.1b, the plume sharpness is observed to have less of a dependency on the extractor voltage with respect to the tip extractor distance. At lower tip-extractor distances, the current density distributions share similar sharpness values and only slightly differ from Gaussian distributions where $\eta = 1$. Further increasing the tip-extractor distance results in a seemingly exponential increase in the plume sharpness as observed at the 80 and 100 micron tip-extractor distances. As sharpness is a characteristic that quantifies the 'drop-off' steepness from the distribution apex (i.e., with increasing sharpness, more so does the distribution qualitatively approaches a Heaviside step function), this is an indication that at smaller tip-extractor distances, there is a more uniform distribution of current density near the plume center axis, and a sharper drop-off of this density as one approaches higher divergence angles. This result is in agreement with the phenomena observed in Fig. 5.1a for the plume width, as this would suggest that at these higher tip-extractor distances a smaller proportional of the field acts radially to the plume to spread the distribution outward and reduce the sharpness as a result.

Similar to Figs. 5.1a and 5.1b, the plume tilt shown in Fig. 5.1c demonstrates a

stronger dependence on the tip-extractor distance relative to the extractor voltage. At lower tip-extractor distances, the data suggest a slight decrease in the tilt with increasing voltage, an intuitive result as a larger field in the axial direction naturally would result in a smaller deviance from the center axis. A decrease in tilt with increasing voltage is less apparent at higher tip-extractor distances where the initial tilt is already relatively aligned with the center axis. In alignment with Figs. 5.1a and 5.1b, increased tip-extractor distances act to reduce the plume tilt and minimize off-axial contributions of the applied field.

Figure 5.2 presents the same plume characteristics across the parameter space for the beam intensity. The inclusion of neutral species in the evaluation of beam intensity allows the consideration of how additional particles within the plume act to influence it's spatial characteristics about this parameter space. Qualitatively, a significant variance of plume characteristics is not observed over both design variables of interest when compared against the data in Fig. 5.1. A greater distinction is observed when comparing the non-dimensionalized parameter coefficients of the surrogate models in Table 5.1. Relative to the current density, the beam intensity surrogate coefficients corresponding to tip-extractor distance are comparable while a larger difference is observed for coefficients corresponding to the electrode potential. This result is an indication that neutrals affect the plume characteristics more significantly across voltage space. With increasing potential, the influence of neutral species on plume characteristics become more apparent as their trajectories increasingly deviate away from the trajectories of charged species. Since this trajectory deviation is directly a function of the applied field strength, this is likely why the most significant difference between the current density and beam intensity distributions is observed in the voltage coefficients. A lesser difference is observed in the tip-extractor coefficients as, per the earlier discussion, this quantity is more representative of the electric field streamline distribution rather than its magnitude.

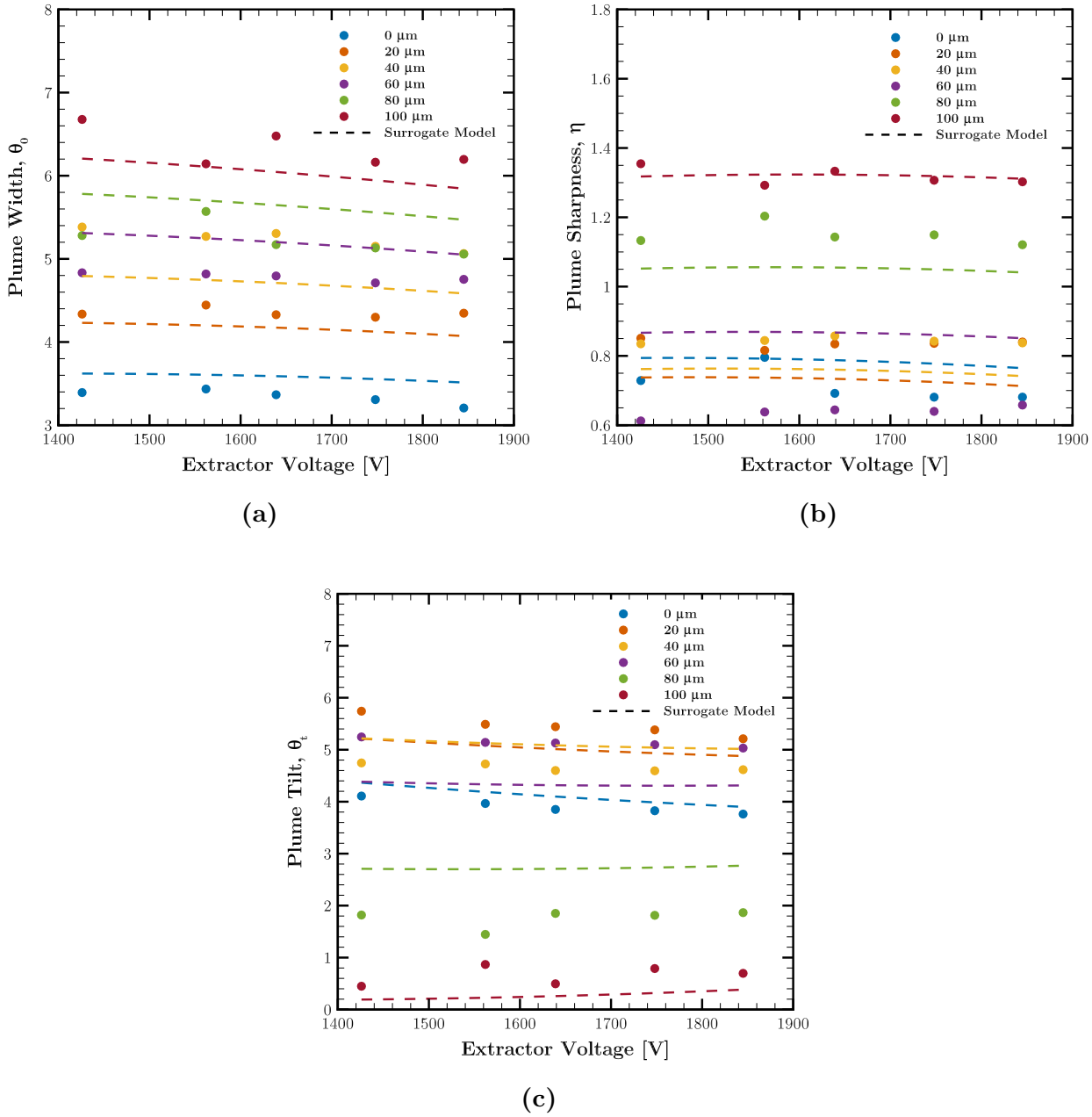

Figure 5.2: Sampled single-emitter model data and surrogate model fits for (a) plume width, (b) plume sharpness, and (c) plume tilt of beam intensity for the axisymmetric study. Characterization parameters are calculated at a radial cross section of 250 µm downstream from the emitter tip.

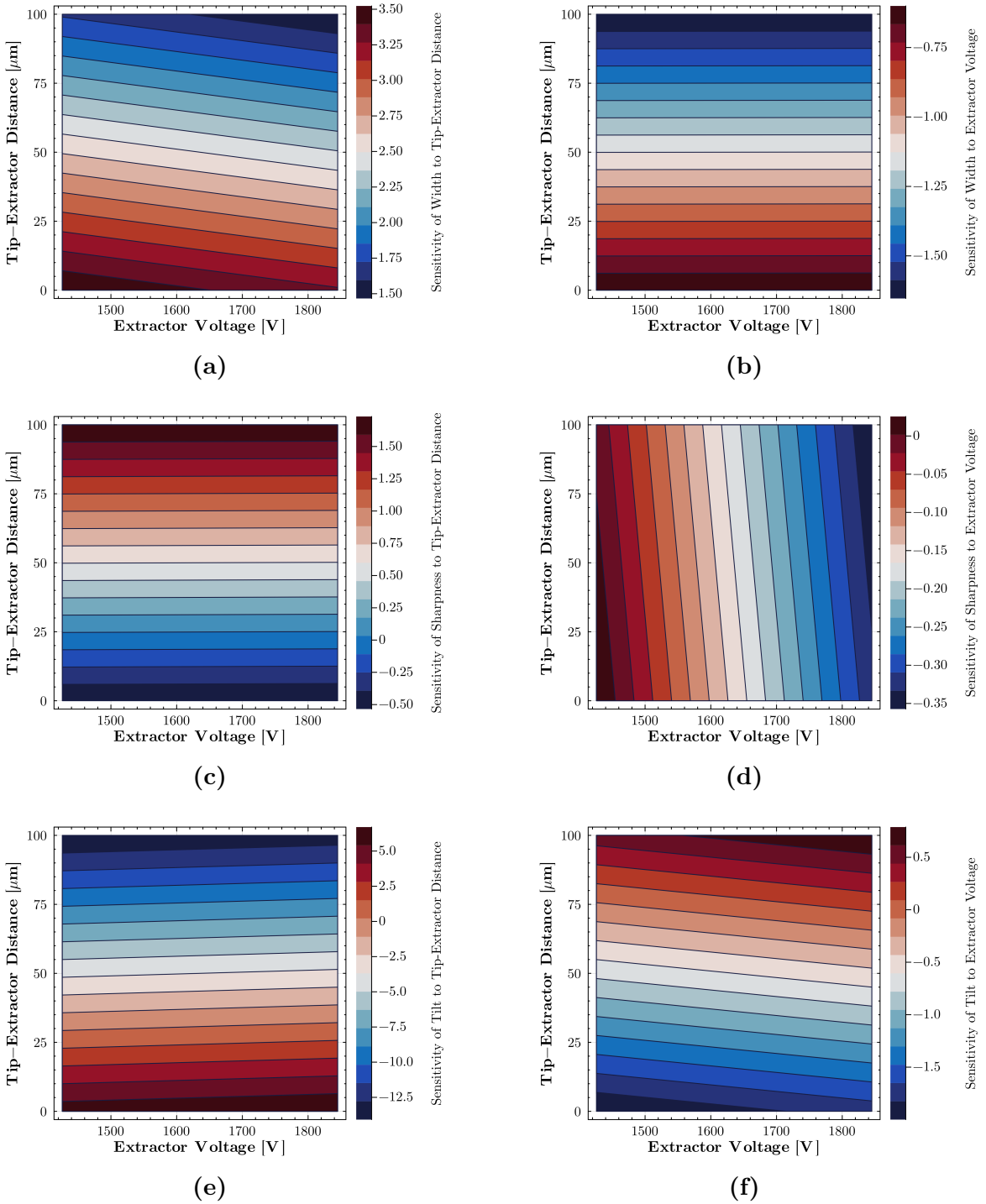

Figure 5.3: Sensitivity of current density plume to operational conditions for the axisymmetric study. These include the sensitivity of (a) width to tip-extractor distance, (b) width to voltage, (c) sharpness to tip-extractor distance, (d) sharpness to voltage, (e) tilt to tip-extractor distance, and (f) tilt to voltage.

5.1.3 Tip-Electrode Distance and Extractor Voltage Sensitivity

One of the advantages in utilizing a surrogate model with polynomial basis functions is that their gradients can be easily found via canonical power rule differentiation. Using this, the partial derivative of Eqn. (5.3) with respect to each independent variable can be calculated,

$$\frac{\partial \hat{f}_j^k}{\partial \hat{d}} = c_1 + 2c_3\hat{d} + c_5\hat{V}, \tag{5.7}$$

$$\frac{\partial \hat{f}_j^k}{\partial \hat{V}} = c_2 + 2c_4\hat{V} + c_5\hat{d}, \tag{5.8}$$

where $\partial \hat{f}_j^k/\partial \hat{d}$ and $\partial \hat{f}_j^k/\partial \hat{V}$ represent the gradients of the surrogate model with respect to normalized tip-electrode distance and extractor voltage, respectively. Together, Eqn. (5.7) and Eqn. (5.8) represent the sensitivity of the single emitter emission model with respect to each operational parameter within the design space. It should be noted, analogous to Eqn. (5.3) and the single emitter model, Eqn. (5.7) and Eqn. (5.8) are approximations of the system sensitivity and are dependent on the basis function space chosen for the original surrogate. For example, inclusion of the $\hat{V}\hat{d}$ term in Eqn. (5.3) enables consideration of cross-parameter influences in both the surrogate model and its corresponding gradients. Omission of said term would result in one-dimensional gradients where functional sensitivities to a given parameter are solely a function of that parameter.

Equations 5.7 and 5.8 are used to quantify, to first order, what extent perturbations of operational variables within the design space influence downstream spatial characteristics of the plume. The sensitivities of each plume characteristic (width, sharpness, and tilt) with respect to both extractor voltage and tip-extractor distances for current density are presented in Fig. 5.3. Across characteristics the system sensitivities are quasi-one-dimensional, where the sensitivity primarily varies in one direction with minimal to no variability in the cross-direction within the design space. With the exception of the voltage-sharpness response in Fig. 5.3d, each characteristic is predominantly more responsive to perturbations in the

tip-extractor distance relative to perturbations in extractor voltage. The sharpness-voltage response is an outlier in this regard in part due it having both the smallest sensitivity range and the smallest absolute sensitivities, where a voltage response becomes apparently dominant in the absence of a tip-extractor dependency. Both plume width sensitivities as well as the tilt-tip extractor sensitivity demonstrate an increased sensitivity with a reduction in tip-extractor distance. An inverse relationship to the tip-extractor distance is observed for the sharpness-tip extractor and tilt- extractor voltage responses.

The sensitivities of each plume characteristic with respect to both extractor voltage and tip-extractor distances for beam intensity are presented in Fig. 5.4. Similarly to the above discussion, the beam intensity sensitivities illustrate to what extent the inclusion of neutral EMI-BF4 species affect the plume characteristic responses. This influence is largely observed in the extractor voltage sensitivities and a minimal effect is observed for the tip-extraction distance sensitivities. Within the extractor voltage sensitivities, relative to the current density surface responses, the additional consideration of neutral species act to increase the sensitivity variance in the extractor voltage, deviating away from the quasi-one-dimensional behavior observed in Figs. 5.4b, 5.4d, and 5.4f.

The introduction of neutrals resulting in an increased sensitivity gradient with respect to extraction voltage is in alignment with the results discussed in Subsection 5.1.2. Again, when considering the current density, the relatively low ion number density coupled with the minimal influence of Coulombic forces on a particle trajectory result in electric field streamlines that are predominantly invariant to the applied potential. The result is, at constant tip-electrode distances, plume characteristics of the current density share this same invariance. When all plume constituents are considered within beam intensity, Fig. 5.4b demonstrates an increased sensitivity of the plume width to the extractor voltage relative to the beam current response surface. The exact reason for this is unclear, but it is postulated that the electric field may have a stronger influence on slower moving ions that are more likely to undergo fragmentation within the domain. The effects of this are then observed

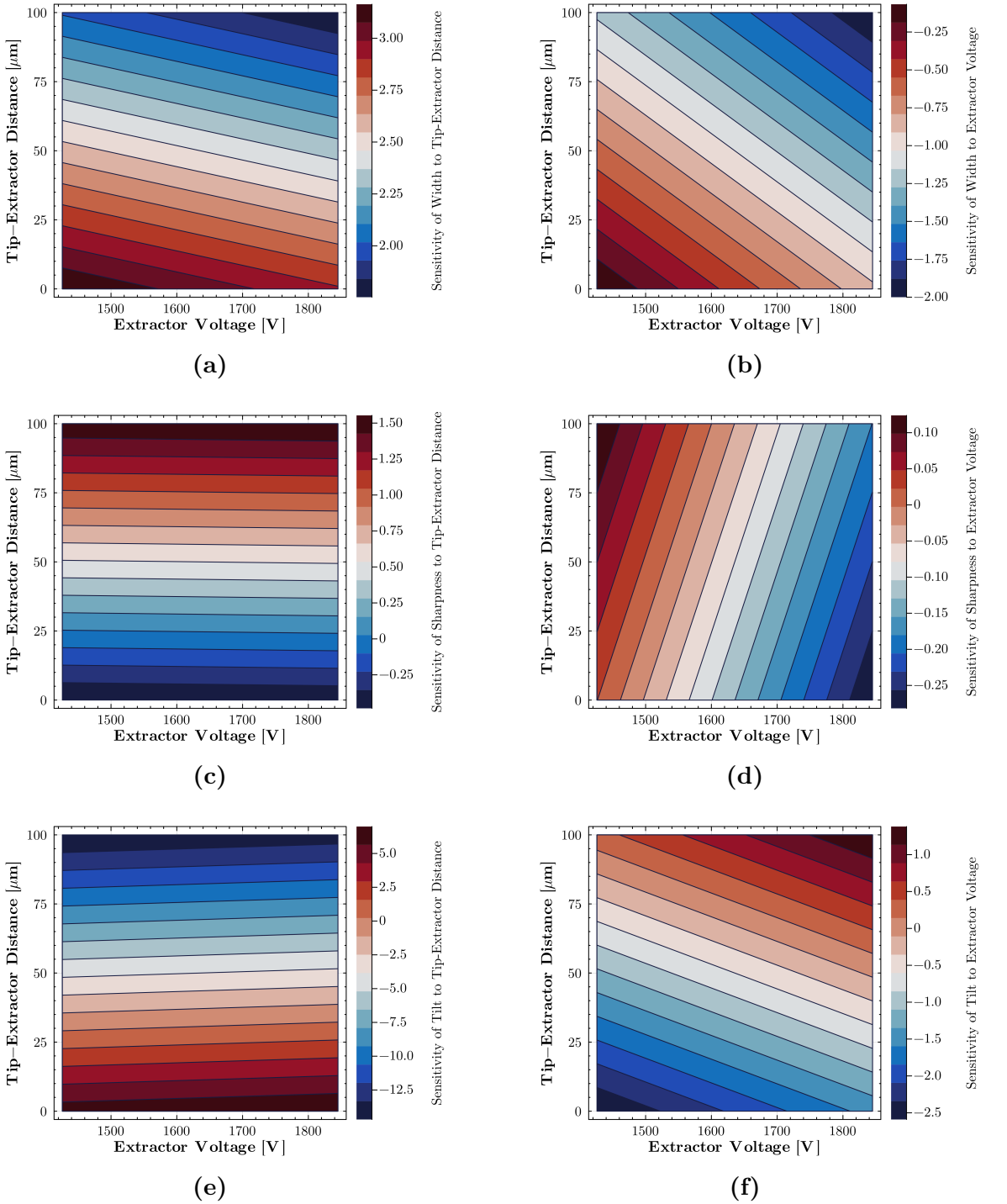

Figure 5.4: Sensitivity of beam intensity plume to operational conditions for the axisymmetric study. These include the sensitivity of (a) width to tip-extractor distance, (b) width to voltage, (c) sharpness to tip-extractor distance, (d) sharpness to voltage, (e) tilt to tip-extractor distance, and (f) tilt to voltage.

within the neutral species distribution captured by the beam intensity.

5.2 Three-Dimensional Study

In this section, the analysis conducted in Section 5.1 is repeated for an alternative design space defined within a fully three dimensional computational domain. Increasing the dimensionality of the grid enables exploration of geometric configurations that are not bound by axisymmetry. These configurations are representative of many arrayed emitters, where tolerances in the manufacturing process result in geometries that are perturbed from the on-axis orientation of a single centerline shared between the emitter and extracting electrodes.

Results from Subsection 5.1.2 demonstrate that, for the parameter space explored, spatial characteristics of the plume are more strongly dependent on variations in geometric conditions relative to operational conditions. For this reason, the three dimensional analysis explores solely a geometric parameter space. More specifically, geometric perturbations are made to the emitter relative to the electrodes to mimic manufacturing tolerances that deviate it from idealistic conditions. The goal of this study is to use a surrogate model trained on this perturbation space to inform to what extent deviations from on-axis emission affect spatial plume characteristics that directly contribute to known failure modes. It has been demonstrated that misalignment can result in a 20–50% lifetime reduction [124]. By sampling high-fidelity simulations of the plume across multiple dimensions of misalignment to train a surrogate, this study seeks to better quantify how misalignment influences life-limiting electrospray life-limiting mechanisms via spatial structures of the plume.

Subsection 5.2.1 describes how the three-dimensional case is initialized, including how the computational grid differs from the axisymmetric case and how the geometric perturbations are defined. In Subsection 5.2.2, the surrogate model is formulated for each beam distribution and the parameter coefficients are presented. Subsection 5.2.3 discusses several observed phenomena distinguishing plumes of misaligned emitters from those of aligned emitters. Subsection 5.2.4 and Subsection 5.2.5 respectively present how these perturbations affect the

plume morphology and their corresponding sensitivities.

5.2.1 Computational Domain

The computational domain of Section 5.1 is expanded into a fully three dimensional space. However, simply expanding on the domain and mesh conditions described in Chapter 4 onto an additional dimension would be too computationally prohibitive. To help alleviate this cost, several changes are made to the simulation conditions relative to the axisymmetric study.

The simulation domain used is nearly identical to the three-dimensional equivalent of that presented in Fig. 4.3, except the axial length of the domain, z_{dom}, is truncated to a length of 750 microns. The farthest cross sectional distribution of the plume is taken at an axial distance of 600 microns, leaving the remaining 150 microns to the outflow boundary as a buffer zone to mitigate potential boundary effects.

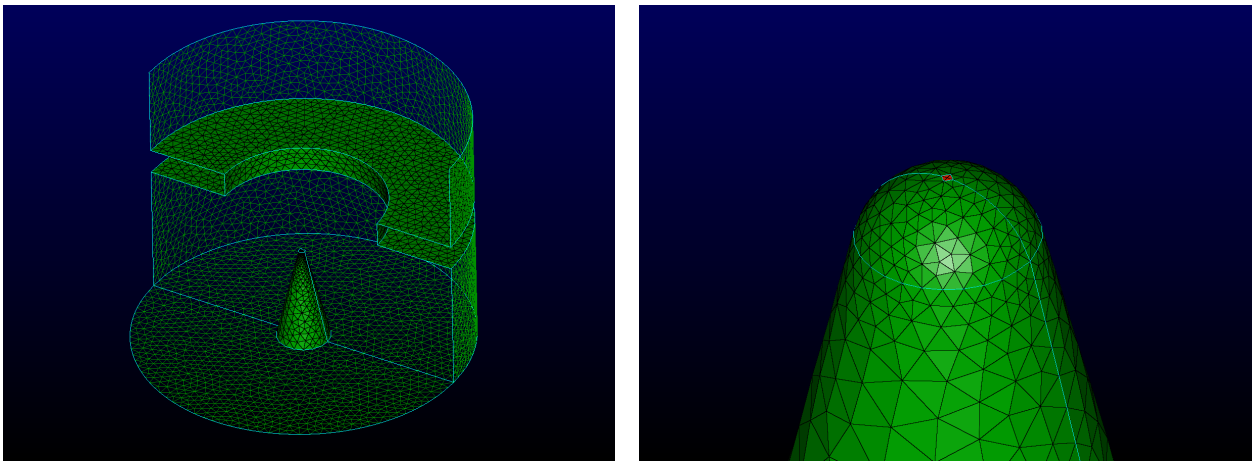

(a) **(b)**

Figure 5.5: Three-dimensional computational mesh of the single emitter domain. The overall domain is presented in (a) where selects facets are hidden for clarity. The emitter tip is presented in (b) with the area colored in red denoting the injection cells at which species are initialized.

The computational mesh utilized for the unperturbed case is presented in Fig. 5.5, where Fig. 5.5a presents an overview of the entire grid (select facets are hidden for clarity) and Fig. 5.5b presents the mesh at the emitter tip. In Fig. 5.5b, the cells at which species are injected are highlighted in red and collectively are refined to the order of the emission radius r^* to ensure the correct boundary condition criteria for alignment with the upstream ionic emission model. Unlike the axisymmetric study, the remaining grid cells are not also refined to this length scale as it would be too computationally prohibitive. Instead a baseline coarse mesh resolution is set throughout the domain, where a subdomain region is defined immediately downstream from the emitter that refines the mesh as a function of distance to the tip. The refining region is fixed across all simulations and takes the form of an inverted truncated cone with an upstream base radius of 40 microns, downstream base radius of 400 microns, and a length of 400 microns. The upstream base is flush with the injection cells at the tip and the radius is chosen such that regardless of the perturbation, the cells that evaporating species are injected into are sufficiently refined to gradients of the ion number density. The downstream base is flush with the outflow boundary and its radius is determined heuristically such that the refining region encapsulates the plume across most cases. Defining a refining region under these criteria allows for minimal changes to the mesh across perturbation samples while ensuring that the mesh near the site of emission is resolved regardless of where the tip is displaced.

5.2.2 Surrogate Model Formulation

The geometric perturbations are implemented as linear combinations of translational and rotational displacements of the emitter with respect to the centerline axis, shown in Fig. 5.6. Translational perturbations, demonstrated in Fig. 5.6b, are defined as translations along the positive x-axis while rotational perturbations, demonstrated in Fig. 5.6c, are defined as rotations of the z-y plane about the x-axis in the counterclockwise direction.

To construct the surrogate model, the bounds and discretization of the two-dimensional

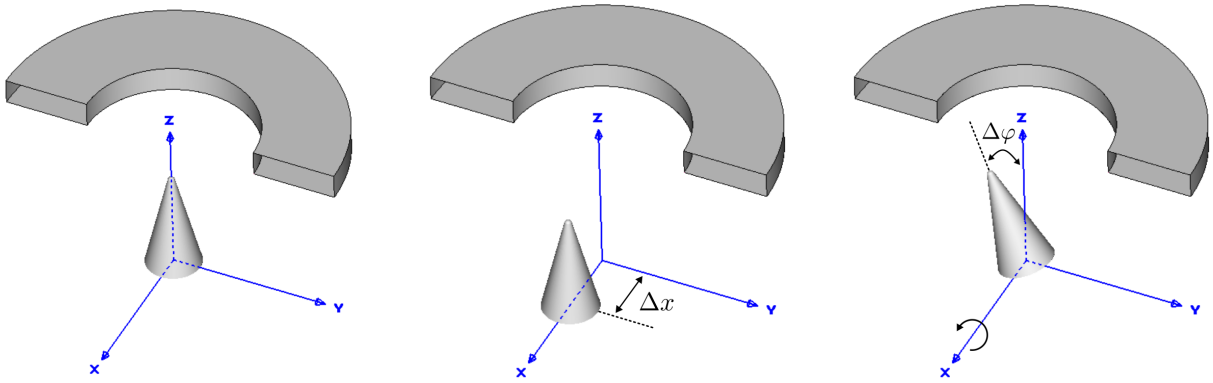

(a) **(b)** **(c)**

Figure 5.6: Schematic of the perturbation space explored in the three-dimensional study, where (a) represents the unperturbed emitter configuration, (b) represents a translational displacement of the emitter in the x-axis, and (c) represents a rotational displacement of the emitter about the x-axis in the counterclockwise direction.

perturbation space must be defined. The emitter is translationally displaced a maximum of 40 microns with a discretization of 10 microns starting from the unperturbed configuration, shown in Fig. 5.6a. The rotational perturbation is applied at a maximum of 10° with a discretization of 5 microns, also including the neutral position.

The influence of these perturbations on plume spatial characteristics is analyzed using the same surrogate model formulated in Subsection 5.1.1,

$$\hat{g}_j^k(\hat{x},\hat{\varphi}) = a_0 + a_1\hat{x} + a_2\hat{\varphi} + a_3\hat{x}^2 + a_4\hat{\varphi}^2 + a_5\hat{x}\hat{\varphi}, \tag{5.9}$$

where $\hat{g}_j^k$ is the model of the beam distribution j for plume characteristic k, $\hat{x}$ is the normalized translational displacement, $\hat{\varphi}$ is the normalized rotational displacement, and a_i are the fitting coefficients. The displacements $\hat{x}$ and $\hat{\varphi}$ are respectively normalized by their maximum values of 40 microns and 10°. Similar to Eqn. (5.3), Eqn. (5.9) utilizes a two dimensional, second order polynomial for the set of basis vectors, where each basis is scaled by its corresponding weight. These weights are again solved using the least squares minimization process described

in Subsection 5.1.1 and are presented in Table 5.2 for each plume characteristic of current density and beam intensity.

What is immediately apparent from Table 5.2 are the nearly identical set of coefficients between the distribution types regardless of the plume characteristic. In the axisymmetric example of Table 5.1, the coefficients across distribution types are of comparable order but still distinct, indicating that neutrals play a discernible (albeit minimal) role in determining the plume morphology. In other words, the change in plume morphology attributed to neutrals is significant with respect to the overall changes in morphology across the entire parameter space. In Table 5.2, the lack of distinction across distribution types suggests that the influence of neutrals is minimal relative to how the overall plume evolve in response to the perturbations. This overall response, described further in the subsequent sections, is significantly greater relative to the axisymmetric case and as a result effectively dampens the smaller contribution that neutrals play in determining spatial plume characteristics relative to ionic monomers and dimers. The influence of neutrals is likely be more apparent downstream from the simulation boundary, where a clearer distinction would be made from charged species whose trajectories are bounded to electric field streamlines. Nonetheless, given the nearly identical response across distribution types, the remaining analysis of this chapter will focus solely on the current density beam to avoid redundancy.

Table 5.2: Surrogate model parameter coefficients for each plume characteristic across distribution types for the three-dimensional perturbation study.

Current Density						
Plume Characteristic, $\hat{g}^k_{cd}(\hat{x},\hat{\varphi})$	$\mathbf{a_0}$	$\mathbf{a_1}$ $[\hat{x}]$	$\mathbf{a_2}$ $[\hat{\varphi}]$	$\mathbf{a_3}$ $[\hat{x}^2]$	$\mathbf{a_4}$ $[\hat{\varphi}^2]$	$\mathbf{a_5}$ $[\hat{x}\hat{\varphi}]$
Width, θ	4.63	0.51	-4.67	0.54	4.16	-0.49
Sharpness, η	0.72	-0.89	0.70	1.30	-0.54	-0.24
Tilt, θ_t	2.56	10.51	20.73	5.42	12.55	-6.29
Beam Intensity						
Plume Characteristic, $\hat{g}^k_{bi}(\hat{x},\hat{\varphi})$	$\mathbf{a_0}$	$\mathbf{a_1}$ $[\hat{x}]$	$\mathbf{a_2}$ $[\hat{\varphi}]$	$\mathbf{a_3}$ $[\hat{x}^2]$	$\mathbf{a_4}$ $[\hat{\varphi}^2]$	$\mathbf{a_5}$ $[\hat{x}\hat{\varphi}]$
Width, θ	4.62	0.51	-4.67	0.54	4.16	-0.49
Sharpness, η	0.72	-0.89	0.70	1.30	-0.54	-0.24
Tilt, θ_t	2.55	10.51	20.72	5.42	12.56	-6.29

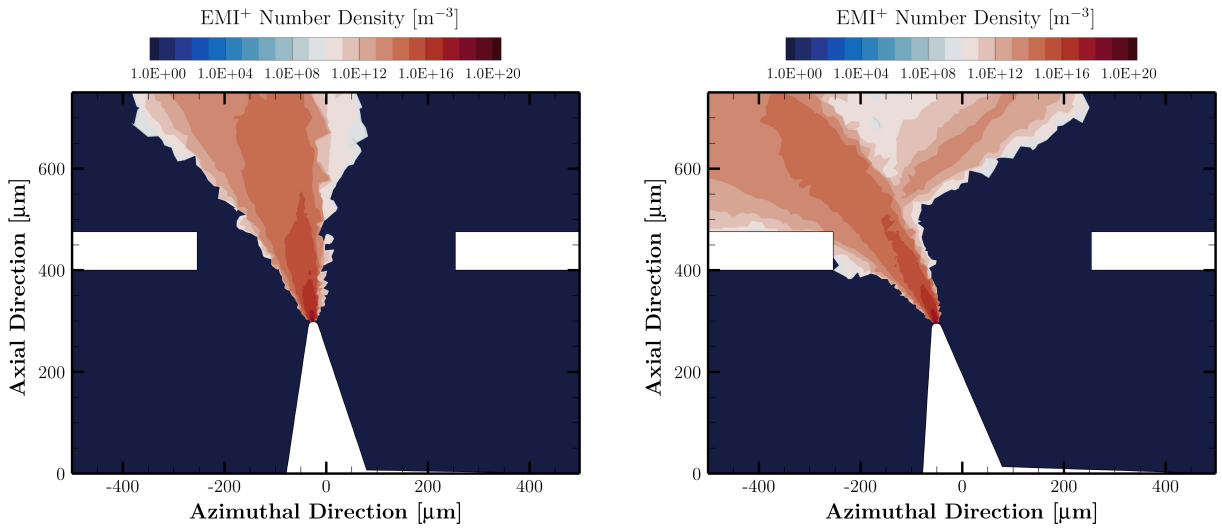

Figure 5.7: Logarithmic number density contours of EMI^+ monomers across the yz-plane for the three-dimensional (a) x=0 µm, φ=5° case and (b) x=0 µm, φ=10° case.

5.2.3 General Effects of Off-Axis Emission

Before discussion of the overarching plume response across the parameter space, it should be noted that several qualitative phenomena are observed that differentiate off-axis emission in perturbed ILIS plumes relative to their unperturbed counterparts.

One of these phenomenon include the steady-state plume morphology response to off-axis emission solely due to rotational perturbations, shown by number density contours of EMI^+ monomer species across the yz-plane in Fig. 5.7. Figures 5.7a and 5.7b present the monomer number density cross-sections for the $\varphi = 5°$ and $\varphi = 10°$ cases, respectively. In Fig. 5.7a, it can be seen that a slight emitter rotation of $\varphi = 5°$ results in a monomer plume whose morphology would be qualitatively comparable to a plume of an unperturbed emitter under some rotational transformation. This is in contract to Fig. 5.7b, where it can be seen that continued rotational displacement of the emitter results in a plume morphology

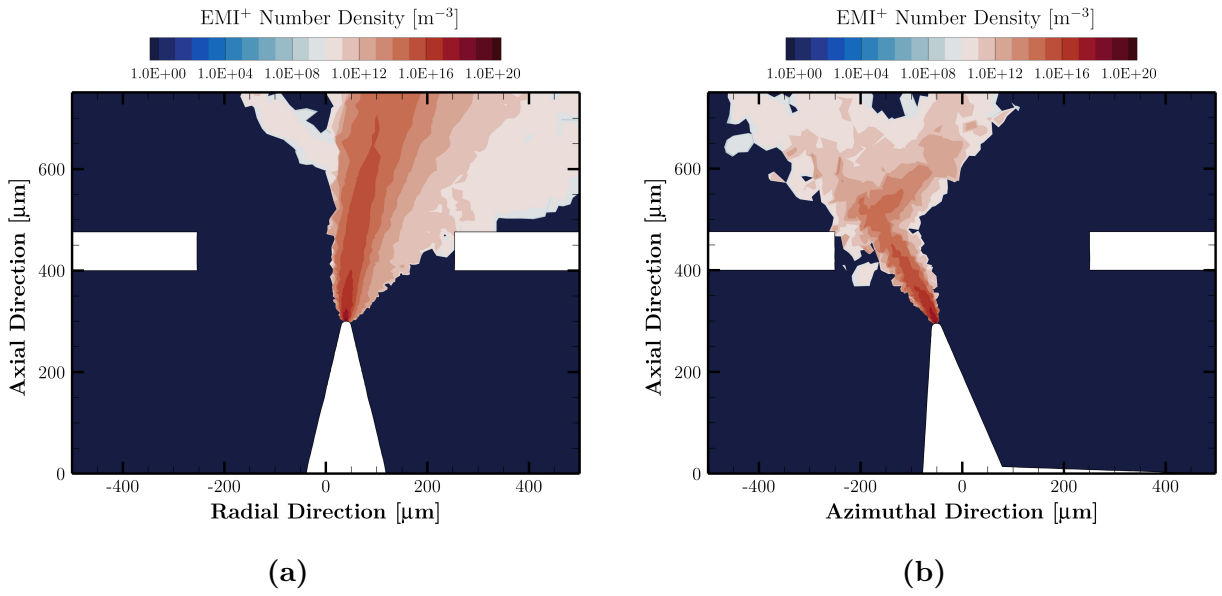

Figure 5.8: Logarithmic number density contours of EMI^+ monomers in three-dimensions (a) across the xz-plane for the x=40 µm, φ=0° case and (b) across the yz-plane at x=40 µm for the x=40 µm, φ=10° case.

that is fundamentally discrete from the $\varphi = 5°$ and unperturbed cases. The downstream monomer distribution of Fig. 5.7b suggests the existence of a critical emitter rotation that, once surpassed, results in a bifurcation of the beam into a dominant primary plume and a secondary, lesser plume traveling in the orthogonal direction. In the $\varphi = 5°$ case, the bulk balance between Coulombic repulsion of monomers and their attraction to the electrodes is still held, where the imposed asymmetry only acts to tilt the beam on the order of a few degrees. This bulk balance is broken at $\varphi = 10°$ as a significant portion of the beam partially screens the electric field in the direction of the tilt, reducing its relative strength compared to the field in the opposite direction. For an outermost component of the beam, this screening effect is significant enough to generate a resultant field that acts orthogonal to the rotational perturbation and is able to advect ionic species.

Similarly, the steady-state plume morphology during off-axis emission can be studied in response to translational perturbations as well. This is presented in Fig. 5.8 where number

density contours of EMI^+ are shown across two cases with the same translational displacement of 40 microns. Fig. 5.8a presents the case where no rotational displacement is considered and is taken across the xz-plane in order to showcase the beam asymmetry. The monomer distribution in this case shows similarities with both Fig. 5.7a and Fig. 5.7b. This is partially expected as the aforementioned physics governing the beam response to solely rotational displacements is generally applicable to perturbations of any type that result in off-axis emission. However, each perturbation type results in a unique normal direction of the injection facet relative to the centerline axis. Assuming identical emission site locations, a rotational displacement contributes a higher proportion of off-axis beam emission than the equivalent translational displacement. This behavior is observed in Fig. 5.8a, where the emitter translation approximately coincides with the $x = 0$ μm, $\varphi = 10°$ case yet demonstrates a diminished beam bifurcation in comparison.

In Fig. 5.8b, monomer number density is presented for the $x = 40$ μm, $\varphi = 10°$ case, sliced at a cross section parallel to the yz-plane and displaced 40 microns such that it intersects the emitter centerline. In this simulation, not only is the collective contribution of both translation and rotation considered, but done so at their respective maximums considered within the sampling space. Qualitatively, the beam takes a form that is similar to Figs. 5.7b and 5.8a in that bifurcation is observed. However, unlike Figs. 5.7b and 5.8a, the superposition of both perturbation types acting in orthogonal directions yields a plume with the largest displacement relative to the centerline axis. The perturbed emitter position coupled with the electric field distribution results in evaporated ionic species with comparatively large cross-flow velocity components that act to reduce the effective exhaust velocity and specific impulse of the thruster.

The influence of off-axis emission on plume morphology can also be illustrated using current density distributions as a function of divergence angle, defined in this geometry as the angle between a species' position vector and the z-axis. Figure 5.9 presents these distributions for the two cases where solely a rotational perturbation is applied. Cross sections of the beam

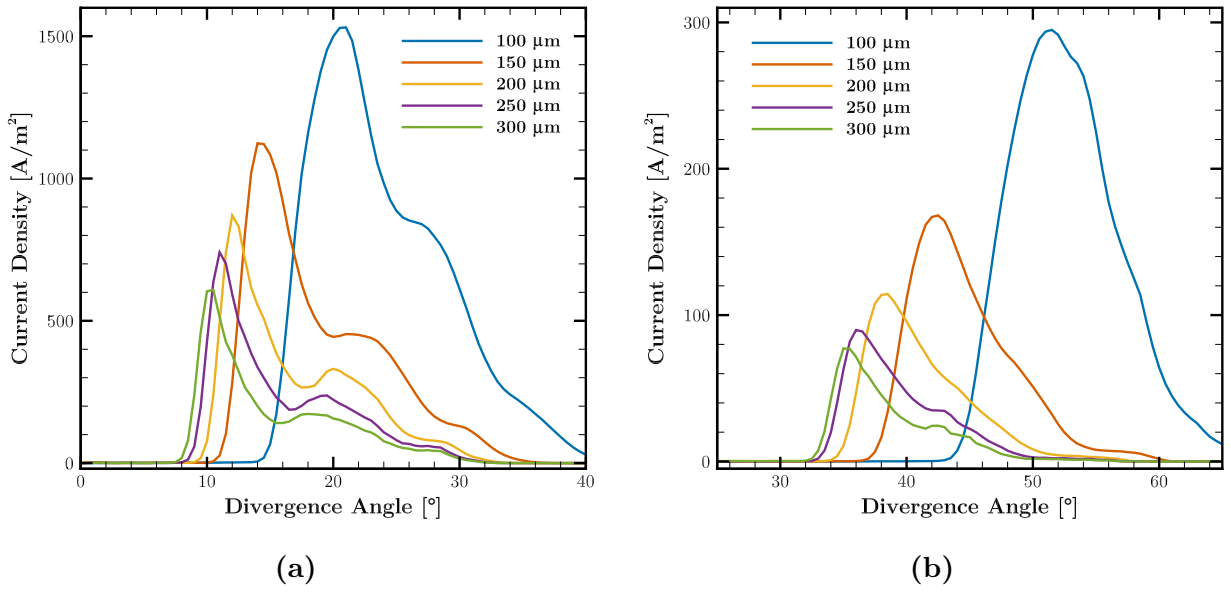

Figure 5.9: Current density distributions versus divergence angle from the z-axis across varying radial cross sections of the beam for (a) the x=0 µm, φ=5° case and (b) the x=0 µm, φ=10° case.

are taken at fixed radial distances relative to the hypothetical location of an unperturbed emitter tip—located at the Cartesian coordinate (0 µm, 0 µm, 300 µm)—ensuring that distributions for a given radius are comparable across all cases. Figure 5.9a presents current density distributions for the x = 0 µm, φ = 5° case, where a clear deviation from the nominal super-Gaussian profiles is observed relative to plume cross-sections of unperturbed emitters. At a radial distance of 100 µm, instead of continuously decaying, the density profile remains consistent for several degrees beginning at approximately 25° before continuing to decrease. With increased radial cross sections this phenomena continues, resulting in bimodal distributions for the remaining profiles. The explanation for this behavior is partially seen in the monomer number density contour of the same case in Fig. 5.7a. Since the divergence angle is taken with respect to the z-axis, at higher angles for a given radius there is an excess of ions that are displaced due to the field asymmetry. The ”bump” is manifested as a result of the collective amount of tilted ions that are coplanar, where the plane is the

curved surface that intersects the beam at a fixed radius. This phenomena is observed but to a lesser extent in Fig. 5.9b. The diminishing effect can be attributed to a greater beam spread as a result of the bifurcation, shown in Fig. 5.7b, resulting in a lower current density amplitude that decays more slowly at higher divergence angles. Across both cases current density amplitudes decrease with increasing radius as the same amount of current is being swept over a larger surface area. Effective divergence is observed to decrease with increasing radius as the evaporated species respond to the asymmetric radial and azimuthal components of the field as it travels downstream.

Radial expansion of the plume as a result of a perturbed emitter also leads to direct propellant flux to the extractor electrode, otherwise known as grid impingement. Impingement is known to occur as a result of two mechanisms. The primary mechanism is through direct overspray from the site of emission, where as the beam expands it comes into contact with either the extractor or acceleration electrodes. The secondary mechanism is through cross-flow expansion of the plume in response to Coulombic expansion and fragmentation of ionic species. Within the three-dimensional perturbation space, the cases where impingement of the extractor grid is observed at the final steady-state timestep are presented in Table 5.3. In cases where impingement occurs (examples of which can be seen in Figs. 5.7b, 5.8a, and 5.8b), the events can predominantly be attributed to direct overspray. While emitter asymmetries due to the displacements do contribute to a larger radial expansion of the plume, this additional expansion is a function of the geometric configuration rather than the

Table 5.3: Three-dimensional perturbation cases where propellant flux to the extractor electrode was observed, resulting in grid impingement. Simulations where impingement occurred during transient evolution of the plume but not at the final steady-state timestep are not included.

	Translational Displacement				
Rotational Displacement	0 μm	10 μm	20 μm	30 μm	40 μm
0°					×
5°					×
10°	×	×	×	×	×

underlying physics that govern the species dynamics. Radial plume expansion from Coulombic repulsion and fragmentation is a transient process that scales with the axial distance from the site of emission, and thus becomes more influential as the beam evolves downstream. As a result, grid impingement from this secondary mechanism is more commonly observed on acceleration electrodes, whose addition are omitted from this study due to the additional computational cost.

From Table 5.3, extractor grid impingement is observed for all cases that included the maximum rotational perturbation of $\varphi = 10°$. Impingement at smaller rotations are only observed in cases where the emitter is also translationally perturbed at the highest displacement of $x = 40$ μm. These results suggest the existence of a perturbation subspace that defines the bounds of which the emitter can still be displaced without impinging the extractor grid. However, further analysis is required to quantify how perturbations within this subspace may contribute to other life-limiting mechanisms, and to what extent these bounds are influenced by changes to operational conditions. Despite these caveats, the results of Table 5.3 can be utilized as an incipient consideration to inform manufacturing tolerances during the production of electrospray thruster emitter arrays. Analysis of how the perturbations considered influence spatial characteristics of the plume, regardless of whether impingement is observed or not, is conducted in the subsequent sections.

5.2.4 Perturbation Space Exploration

Surrogate model fits—after solving for the coefficients in Eqn. (5.9)—and sampled single-emitter model simulations for each plume characteristic across the perturbation space are presented in Fig. 5.10. Across each characteristic, it is clear that the plume responds distinctly to minor ($0° \leq \varphi \leq 5°$) and major ($5° < \varphi \leq 10°$) rotations of the emitter, regardless if any translations are applied. This is in alignment with the results discussed in Subsection 5.2.3, where major rotations often contributed to significant, macroscopic changes to the plume morphology that uniquely characterize them relative to plumes of emitters

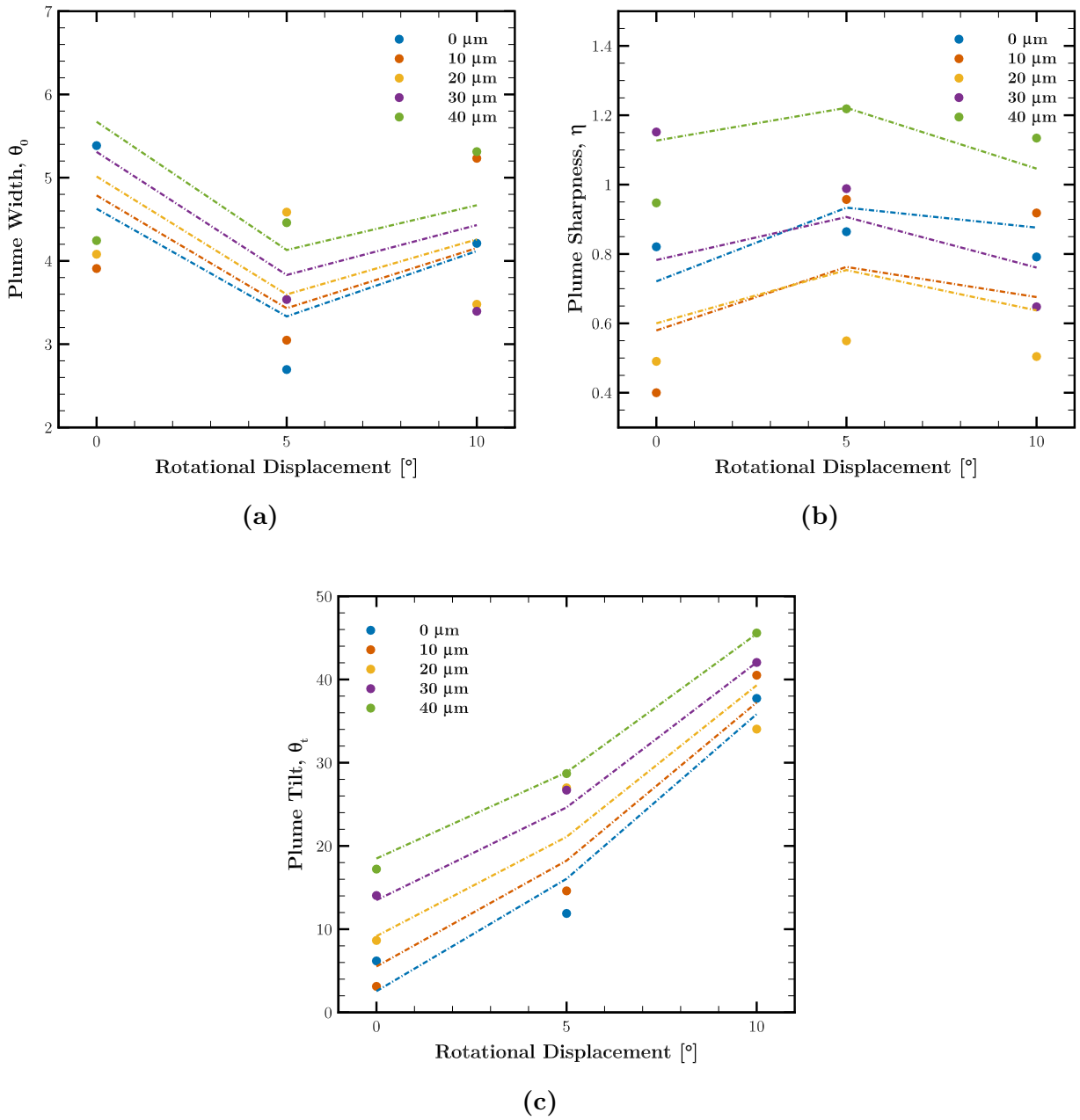

Figure 5.10: Sampled single-emitter model data and surrogate model fits for (a) plume width, (b) plume sharpness, and (c) plume tilt of current density for the three-dimensional perturbation study. Characterization parameters are calculated at a radial cross section of 250 µm downstream from the location of an unperturbed emitter tip.

undergoing little to no perturbation.

In Fig. 5.10a, surrogate model fits and single emitter model samples are shown for the plume width parameter. Minor increases of the emitter rotation have the effect of reducing the width. This is demonstrated in Fig. 5.7a where, relative to an unperturbed emitter plume, the field asymmetry experienced by ions at injection curtail radial expansion in the direction orthogonal to the tilt. The comparative increase of radial expansion in the tilt direction is not equal in magnitude, effectively compressing the beam and reducing the overall width. This behavior does not continue with further rotational displacement. Contrarily, an overall increase in the plume width is observed as an instability threshold is inevitably met and the plume bifurcates into two beams acting orthogonal to one another. As can be seen in Fig. 5.7b, this bifurcation drastically increases the radial influence of the beam and thus increases the effective width relative to the stable state. In response to emitter translations, the width is observed to increase with increased displacement. This behavior is expected, as the magnitude of radial field component is greater the further the emitter is translated. Emitted ionic species are then initialized at a greater potential energy upon injection that subsequently converts to kinetic energy in the cross-flow direction. This increased radial kinetic energy is then manifested as a wider plume with reduced exhaust velocity in the axial direction.

In Fig. 5.10b, surrogate model fits and single emitter model samples are shown for the plume sharpness. Sharpness is a parameter that arises from the super-Gaussian formulation of Eqn. (4.32), and is what distinguishes it from a traditional Gaussian distribution via the introduction of an exponential factor. It should be noted that its meaningfulness in this context is unclear as a parameterization tool as it has been shown in Fig. 5.9 that radial cross sections of perturbed plumes introduce elements of bimodality that may act to skew its value. For example, a bimodal distribution with larger distances between peaks may artificially act to increase its sharpness parameterization, as a super-Gaussian distribution with a ”flatter” tip would result in an overall smaller numerical error when curve fitting than a ”sharper”

tip that would better resolve the sharpness of the larger mode in the distribution. Despite this, Fig. 5.10b still demonstrates general trends of how the sharpness parameter evolves in response to certain perturbation types. For example, its response to emitter rotations is the inverse to that observed for the plume width, in that minor rotations act to increase the sharpness while major rotations act to decrease the sharpness. However, a trend is less clear in response to emitter translations, where this can likely be attributed to the aforementioned numerical issues.

In Fig. 5.10c, surrogate model fits and single emitter model samples are shown for the plume tilt. As expected, increased rotational perturbations of the emitter contribute to a more tilted beam relative to the centerline z-axis. The rate at which rotations affect tilt is found to be larger for major displacements relative to minor ones, and discussed further in the subsequent section on model sensitivities. A positive tilt correlation is also observed with respect to emitter translations, where the rate of this behavior is again dependent on the magnitude of displacement.

5.2.5 Translational and Rotational Displacement Sensitivity

The sensitivity of plume characteristics with respect to each perturbation type is found by taking partial derivatives of the surrogate model in Eqn. (5.9), analogous to the procedure demonstrated in Subsection 5.1.1. These equations take the form

$$\frac{\partial \hat{g}_j^k}{\partial \hat{x}} = a_1 + 2c_3\hat{x} + a_5\hat{\varphi}, \tag{5.10}$$

$$\frac{\partial \hat{g}_j^k}{\partial \hat{\varphi}} = a_2 + 2a_4\hat{\varphi} + a_5\hat{x}, \tag{5.11}$$

where $\partial \hat{g}_j^k/\partial \hat{x}$ is the partial derivative of the model for beam distribution j and plume characteristic k with respect to normalized emitter translation $\hat{x}$ and $\partial \hat{g}_j^k/\partial \hat{\varphi}$ is the partial derivative of the model for beam distribution j and plume characteristic k with respect to normalized emitter rotation $\hat{\varphi}$. Due to the nearly identical responses across both beam

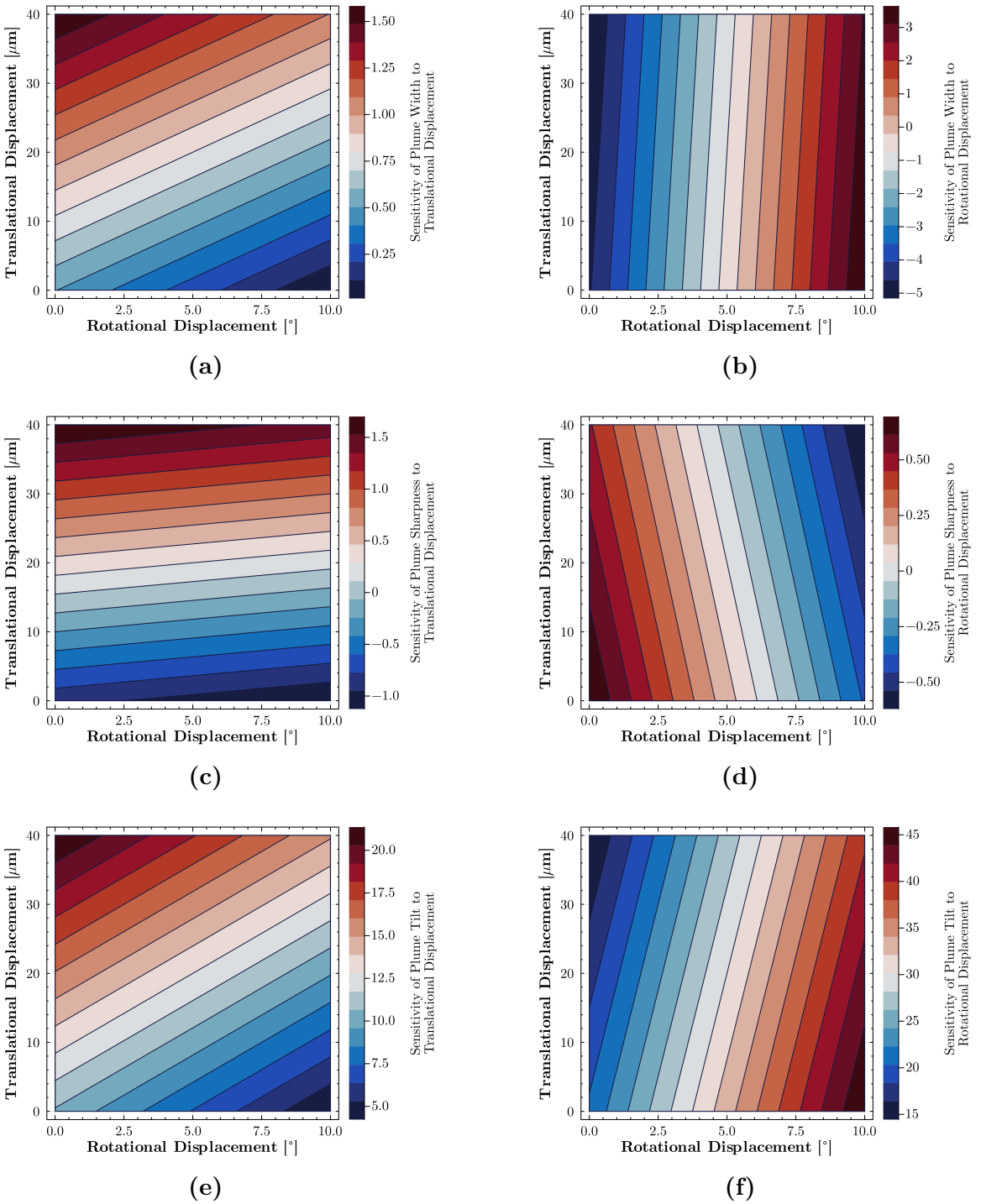

Figure 5.11: Sensitivity of current density plume characteristics to each displacement type for the three-dimensional study. These include the sensitivity of (a) width to translations, (b) width to rotations, (c) sharpness to translations, (d) sharpness to rotations, (e) tilt to translations, and (f) tilt to rotations.

distributions shown in Table 5.2, only sensitivities of the current density are considered to avoid redundancy.

Sensitivities of plume characteristics with respect to each perturbation type are plotted as two-dimensional response contours and presented in Fig. 5.11. Plume width sensitivities are shown in Figs. 5.11a and 5.11b for emitter translations and rotations, respectively. In both cases, the rate at which the width responds to a given perturbation type increases linearly with the magnitude of that same perturbation (i.e. sensitivity to rotations becomes greater with further rotational displacement). In Fig. 5.11a, plume width is shown to be less responsive to variations in emitter translations when additional rotational displacement is introduced. This cross-perturbation influence is not observed in the width's sensitivity to emitter rotations, where variations in translation have seemingly little effect. These results suggest that beam spread is overall more responsive to rotational perturbations, and that minimizing manufacturing tolerances of this type would most efficiently mitigate variation in plume divergence.

Sensitivity of plume sharpness with respect to each perturbation type is shown in Figs. 5.11c and 5.11d. Unlike the plume width, minimal cross-perturbation influence is observed and sensitivity to a given perturbation is largely a function of that same perturbation. In regards to the rotational sensitivity, unlike Fig. 5.11b, increasing the rotational displacement acts to reduce its influence on the sharpness variation.

Sensitivity of plume tilt with respect to each perturbation type is shown in Figs. 5.11e and 5.11f. Qualitatively, the tilt's response to variations of each perturbation type is similar to that observed for the beam width. Comparatively, the tilt's rotational sensitivity has a larger dependence to translational displacements. As a result, the tilt characteristic showcases the greatest sensitivity across perturbation types, where varying one perturbation directly influences how the tilt will respond to another perturbation. In addition, the magnitude of the tilt's sensitivity across perturbation types is approximately an order of magnitude larger than those observed for plume width and sharpness.

5.3 Conclusions

This chapter explored how plume characteristics in ionic electrospray thrusters are influenced by operational and geometric perturbations, leveraging the coupled emission and plume model developed in Chapter 4. By examining variations in key parameters such as extractor voltage, tip-to-extractor distance, and emitter alignment, this chapter quantified how these factors influence plume morphology, informing future design of multiplexed thruster arrays.

To efficiently explore the vast design space and mitigate the computational expense of high-fidelity simulations, a surrogate modeling approach was employed. Surrogate models provided a computationally efficient means of approximating the behavior of the high-fidelity single-emitter model, enabling the exploration of input-output relationships across a wide range of design parameters that would otherwise be computationally infeasible.

The axisymmetric analysis revealed a strong dependence of the plume characteristics considered—width, sharpness, and tilt—on both operational parameters and geometric conditions. Characteristics were shown to be broadly more sensitive to perturbations in tip-electrode distance relative to extractor potential. Results of the plume response demonstrated that its morphology is not strongly dependent on inter-particular Coulombic repulsion, but that ion trajectories are largely bound by electric field streamlines and species inertia, in agreement with current literature.

Extending the analysis to three dimensions allowed for the investigation of non-axisymmetric perturbations, including translational and rotational misalignments. Perturbations resulting in off-axis emission were shown to significantly alter plume morphology relative to unperturbed emitters, such as exhibiting cross-sectional distributions that deviated from the nominal super-Gaussian form and displayed elements of bimodality. This study demonstrated that even minor geometric deviations can lead to substantial variations in plume behavior, including phenomena such as beam bifurcation and increased risk of grid

impingement. Sensitivity analysis highlighted that rotational misalignments have a more pronounced effect on plume tilt and beam divergence compared to translational displacements, suggesting that manufacturing tolerances for rotational alignment should be particularly stringent.

Overall, the results of this chapter provided actionable insights for improving the reliability and performance of ionic electrospray thrusters using a combination of both high and lower fidelity models. These findings can inform manufacturing tolerances and operational guidelines for single-emitter designs and potentially multiplexed arrays, helping to extend the operational lifetime of these propulsion systems.

Chapter 6

Conclusions

This dissertation presented the formulation and implementation of an end-to-end single emitter model of an electrospray system undergoing steady-state, pure ionic emission and a parametric study demonstrating how such a model can be used in the mitigation of life-limiting mechanisms for these propulsive devices. Given these developments, this concluding chapter summarizes the research conducted, highlights the key contributions of the work, and provides recommendations for future investigation.

6.1 Summary of Dissertation

Chapter 1 introduced the material and motivation underpinning the work of this dissertation. The chapter began with a brief historical overview of electric propulsion, with an emphasis on the background and evolution of electrostatic electrospray thrusters from their incipience in the mid 20th century to their renaissance in the modern era, thanks in part to advancements in MEMS and the miniaturization of spacecraft. The characteristics of electrosprays thrusters were reviewed, including the various thruster technologies and emitter architectures, as well as their life-limiting mechanisms precluding their widespread implementation across missions that require a scalable propulsive device and/or fine attitude control. An emphasis on ILIS thrusters was specified due to their efficiency enabled by purely ionic emission, ease of implementation from their passively-fed operation, and straightforward fabrication from MEMS manufacturing. The unique role that modeling plays in advancing ILIS

technology was also reviewed in this chapter, in addition to a literature review summarizing the research efforts made thus far in simulating the governing physics of ILIS emission.

Chapter 2 laid the theoretical groundwork for understanding the physics underlying all emission from electrospray thrusters, especially those where ionic liquids—room temperature molten salts—are used as the working liquid. This began with the emergence of Taylor cones, canonical structures that form when the meniscus of a conductive fluid is electrically stressed beyond a critical threshold. How such a structure emerges from a spheroidal droplet was mathematically derived, demonstrating that the phenomenon is largely due to the interfacial balance between surface tension and electrostatic stresses from an applied potential gradient. This analysis led to Taylor's universal cone angle of approximately 49.29°, a result that fascinatingly does not depend on properties of the working liquid or the applied voltage. From a Taylor cone, one of several emission modes are possible depending on the operational configuration. In the steady cone-jet regime, a continuous liquid jet emanates from the cone apex and subsequently breaks into charged droplets. Scaling laws were derived to link characteristics of the jet—such as emission current and jet diameter–to key parameters such as electric conductivity, surface tension, and flow rate. As the nondimensional flow rate is reduced, the emitter transitions into a mixed mode where both droplets and ions contribute to emission, before finally reaching a purely ionic regime. This mode is favored by ionic liquids due to their high conductivity and large electrochemical windows that enable jet suppression and emission solely from ion evaporation. The physics of ion evaporation were derived using a modified Arrhenius model and the method of image charges, together yielding characteristic scaling laws for quantities of interest such as the critical field strength for emission, emission radius, and total current.

Chapter 3 introduced the electrohydrodynamic (EHD) meniscus model designed to capture the multiscale two-phase physics of steady-state ionic emission from an ionic liquid. The model coupled electrostatic phenomena using Laplace's equation in both the liquid and vacuum domains alongside low Reynolds number fluid dynamics using the Stokes approx-

imation of the incompressible Navier-Stokes equations. Within the liquid, this framework incorporated the Taylor-Melcher leaky dielectric model to handle the electrokinetics alongside a phenomenological ion evaporation law, allowing the model to solve for the current density distribution across the meniscus and thus the total emitted current. The chapter also presented the numerical implementation of the model and described a nonlinear global algorithm that uses finite element methods to solve for the electric potential and liquid velocity fields that enforced select boundary conditions at the interface for a given morphology. From this, an interfacial residual was calculated and used to perturb the meniscus shape, where the numerical procedure was repeated until convergence and a steady-state configuration was found. Special consideration was given to the numerical challenges faced during this implementation, namely within the mesh deformation and ill-conditioning of the Stokes system. Despite these challenges simulation results yielded select agreements with the literature, such as a quasi-Taylor cone morphology with a closed apex and electric field strengths that agree with known scaling laws.

In Chapter 4, an end-to-end single-emitter electrospray model was developed that coupled upstream ionic emission from the meniscus apex with a downstream kinetic plume solver that accounted for far-field ion dynamics. Due to the numerical challenges faced with the high-fidelity EHD model, an alternative lower-fidelity semi-empirical emission model was introduced to initialize the plume model. This secondary model used analytical scaling laws to calculate a zero-order approximation of the total ion current as a function of the interfacial electric field distribution, where the result was then fit onto experimental data to obtain a higher order of accuracy. Once determined, the emitted current was converted into number densities of monomer and dimer species that are weakly coupled into the plume model for initialization. The plume itself was simulated using a hybrid Direct Simulation Monte Carlo (DSMC) and Particle-in-Cell (PIC) method that respectively account for species collisions and their dynamics in response to an applied potential gradient. Modifications were made to the original in-house solver to account for the single-polarity nature of the ionic plume

as well as incorporate a fragmentation submodel that captured the dissociation of dimer species into monomers and neutrals. Simulation results included plume characteristics such as beam divergence and thrust and were partially validated against experimental data from the AFET-2 thruster developed at AFRL. The analysis demonstrated agreement near the onset of significant ionic emission, while discrepancies at higher voltages highlighted the influence of fragmentation and neutral species on thruster performance.

Chapter 5 showcased an example of how the end-to-end single-emitter emission and plume models could be used to advance the current technology readiness level of electrospray thrusters. Namely, the chapter explored how perturbations in both the operational and geometric configuration influenced downstream plume characteristics, which could directly contribute to select life-limiting mechanisms such as overspraying resulting in electrode impingement. These perturbations were explored using lower-fidelity surrogate models that enabled efficient exploration of the design space without the prohibitive computational cost of conducting full sweeps of high-fidelity simulations. Surrogate models also map discrete simulation samples onto a continuous function space with analytical gradients, reducing the barrier to conduct sensitivity analysis studies as well. An axisymmetric, two-dimensional study was conducted where extractor voltage and tip-to-extractor distances were varied and their influence on spatial characteristics of the simulated plume were observed. The input parameter space was discretized using a full-factorial sampling and the resulting dataset was used to train a two-dimensional second-order polynomial surrogate model. A sensitivity analysis was conducted by taking partial derivatives of the surrogate model, revealing that the plume structure was more strongly influenced by variations in the tip-to-electrode distance relative to the extractor voltage within the parameter space explored. An additional three-dimensional study was conducted that investigated the influence of non-axisymmetric perturbations, specifically translational and rotational misalignments of the emitter relative to the extractor electrode that mimicked deviations in manufacturing processes. These perturbations were shown to significantly influence plume behavior, such as introducing off-axis emission, beam

bifurcation, and even grid impingement under severe misalignments. Sensitivity analyses for this case indicated that rotational misalignments had a particularly pronounced effect on plume characteristics such as tilt and beam divergence relative to translational misalignments, suggesting that rotational alignment tolerances should be prioritized in electrospray thruster designs.

6.2 Novel Contributions

The objective of the research described in this dissertation was to develop mathematical models and numerical toolsets that resolve the physics governing ionic emission within single-emitter electrospray thruster configurations, with the overarching goal of enhancing simulation capabilities for mitigating life-limiting mechanisms. The novel research contributions of this work toward achieving that objective included:

- **Formulation of a steady-state electrohydrodynamic (EHD) meniscus model**

  Although other EHD meniscus models have been presented in the literature, this work introduced a unique formulation that is distinct in the handling of several phenomena. These include an Ohmic conduction model that is independent of temperature and an emission model that is independent of space charge effects, both due to their negligible influences. Depending on the operational configuration, the resulting model was capable of retaining its fidelity while requiring comparatively fewer computational resources to execute.

- **Development and implementation of a finite element solver for the EHD meniscus model**

  Simulation of the EHD meniscus model was accomplished through the development of a ∼10,000 line C++ finite element code that discretized the weak formulation of the Laplace and Stokes boundary value problems, employed numerical methods to solve the linear system, and implemented a global algorithm that perturbed the meniscus

morphology as a function of the interfacial residual. Despite the numerical challenges faced, the code laid the foundational groundwork for a comprehensive solver and was developed in a modular fashion, enabling straightforward integration and replacement of numerical methods. This framework not only facilitated detailed investigation of EHD phenomena at the meniscus but also provided a scalable platform for future enhancements to improve simulation accuracy and computational efficiency.

- **Introduction of a novel semi-empirical single-emitter ionic emission model**

  By considering characteristic scaling laws and experimental data measured for the AFET-2 thruster, this work introduced a novel one-dimensional semi-empirical model that approximated the emission current across the meniscus as a function of the normal electric field strength. It was shown that the model was valid in select operational conditions where the meniscus morphology can be approximated as an idealized Taylor cone. Input field strength distributions were obtained using the multidomain Laplace equation module within the EHD meniscus solver.

- **Expansion of in-house direct simulation Monte Carlo (DSMC)/particle-in-cell (PIC) solver capability for single-polarity electrospray plumes**

  The in-house DSMC/PIC solver, originally designed to simulate plasma plumes of traditional EP systems, was reformulated with a direct Poisson solver instead of one derived from electron fluid models. This was required as the charged nature of electrospray plumes does not originate from an active ionization process, resulting in negligible electron number densities relative to ion and neutral number densities. This work also introduced a field-free fragmentation model within the plume solver that simulates the dissociation of solvated ion clusters, which is crucial for capturing the polydispersity and performance-limiting dynamics of evaporated species.

- **Development of the coupled emission-plume framework and its comparison against experimental measurements from the AFET-2 thruster**

Given the emission current, this work presented injection boundary conditions that weakly coupled the continuum EHD and kinetic plume models to formulate a cohesive end-to-end framework to simulate a single emitter. As a result, the influence of upstream inlet conditions, such as the emitter geometry, on downstream plume characteristics can be directly studied. Although AFET-2 data were used to calibrate the semi-empirical emission model, partial validation of the end-to-end framework was still accomplished using thrust measurements, where agreement was found across a range of extraction voltages.

- **Conduction of sensitivity analyses using surrogate models to quantify the plume response to perturbations in geometric and operational conditions**

  Surrogate models were shown to be a computationally efficient means of exploring the configuration design space of coupled emission-plume simulations in two and three dimensions. Gradients of these models enabled this work to quantify the sensitivity of spatial plume characteristics to perturbations in select geometric and operational configurations, offering insights and a framework for future design optimization studies.

6.3 Recommendations for Future Work

The work described in this dissertation focused on building the foundational tools required for high-fidelity end-to-end simulation of electrospray thrusters. Despite these advances, many challenges remain to be addressed before the framework can be considered a fully stable and robust solver.

Future researchers interested in simulation of EHD menisci and single-polarity ionic plumes should consider pursuing alternative conceptual formulations and methodologies that would be both more computationally amenable and more straightforward to implement thanks in part to the ease-of-use and capability of modern numerical libraries. For example, the EHD

model of Chapter 3 could be reformulated as a partial differential equation (PDE)-constrained optimization problem [76], where the steady-state meniscus morphology is found by seeking the minima or stationary points of certain functionals derived from the governing interfacial physics. In the case of an EHD meniscus undergoing field evaporation, this functional would account for the electrostatic energy, surface energy, and viscous dissipation within the ionic liquid. The combined functional would be constrained by the interfacial boundary conditions such as the phenomenological ion evaporation law and the PDEs describing both the liquid fluid dynamics and the electric field potential across the liquid and vacuum domains. Once the minimization problem is defined, the objective functional and corresponding conditions are discretized such that the optimization variable becomes finitely dimensional. In this form, the minimization problem would then be subject to one of several possible gradient-based optimization methods that would ultimately solve for the steady-state morphology. In terms of solver and software development, several tools and libraries are readily available that provide high-level functionality of the implementation and discretization of optimization algorithms. Assuming a finite-element discretization, the FEniCS computing platform [7] is a popular open-source library for solving PDEs that enables the quick translation of a variational formulation into an efficient FEM solver. Another resource includes the Toolkit for Advanced Optimization (TAO), a package of optimization algorithms developed at Argonne National Laboratory and is distributed with the Portable Extensible Toolkit for Scientific Computing (PETSc) [6]. TAO was designed with scalability in mind on high-performance architectures, allowing future researchers to more focus on the higher-level physics instead of the lower-level implementation of numerical algorithms.

Several recommendations for areas of future research are also provided to improve the fidelity and computational efficiency of the models and numerical methods that were implemented in this work:

- **Implementation of alternative numerical routines within the EHD meniscus code**

  Several numerical modifications and additions are recommended for the EHD meniscus solver to address the challenges discussed in Chapter 3. Firstly, an alternative numerical routine is suggested for solving the Stokes equations using Taylor-Hood elements as implemented. It is suggested that the DUNE numerical solvers be substituted with those made available by PETSc [6], an alternative library of parallel and scalable routines for the solutions of partial differential equations. Within PETSc, the Stokes problem can be efficiently solved using a block preconditioner via their MatNest and VecNest data structures, resulting in a scheme that would be both better conditioned and parallelized for increased computational efficiency. Secondly, alternative routines are recommended for the internal mesh deformation between interfacial perturbations. It is recommended that future research consider the implementation of arbitrary Langrangian-Eulerian (ALE) methods that would better evolve the mesh as it would be coupled within the problem weak formulation. However, ALE methods may not be sufficient in cases where significant interfacial deformation is required due to a large displacement between initial and final meniscus morphologies. For these scenarios, it is recommended that future work consider applying automatic remeshing routines or mesh-free implementations entirely.

- **Strong coupling between emission and plume models**

  Currently, a weak coupling is applied between emission and plume domains that limits communication among solvers to a single downstream direction. This is sufficient in the conditions explored where space-charge effects around the emission regime are considered negligible and thus would have a minimal effect on the meniscus morphology and emission characteristics. However, in cases where significant ion evaporation is expected, this assumption may no longer be valid. For this reason,

it is recommended that future work consider implementation of a strong boundary condition where the Poisson solvers within the EHD code and kinetic plume code communicate with one another to check for discrepancies in the electric field distribution across the meniscus. Significant emission could contribute to a space charge distribution that may act to screen the field strength at the meniscus apex, breaking the interfacial stress balance and requiring the EHD code to seek a new steady-state configuration that would presumably reduce the total emitted current and in turn provide different injection number densities into the plume code.

- **Field-induced fragmentation model for solvated ions**

  The field-free fragmentation model implemented within the plume code accounts for the spontaneous dissociation of dimers independent of an applied electric field that has been experimentally observed to follow a constant-rate equation. Such a model only partially captures the total fragmentation occurring within the plume as it does not account for how the activated process is accelerated in the presence of an applied potential gradient. Future work should consider increasing the fidelity of the fragmentation model by adding an additional subroutine (which would likely be empirically based or derived from molecular dynamics simulations) that considers how the electric field influences the fragmentation rate of dimer and trimer species. This is critical as considering the field would only act to increase the fragmentation rate and the neutral number density within the plume, likely increasing the beam divergence and thus the likelihood of grid impingement occurring.

- **Expansion of design space and computational domain**

  Future studies should consider expanding the geometric and operational configurations explored in this dissertation to better understand the range of conditions that result in steady emission and minimize electrode impingement. For example, due to the increased computational cost and dimensionality of the input parameter space, the

simulations conducted did not explore the influence of an additional downstream acceleration electrode on spatial plume characteristics. Given the prevalence of these grids in passively-fed porous electrospray thruster designs that act to improve the viability of these propulsive systems, it would be very beneficial to include their relative influence in future end-to-end single-emitter simulations.

- **Single-emitter validation data and improved emission diagnostics**

  Simulations were validated against emission and thrust measurements of the AFET-2, a multiplexed electrospray thruster where hundreds of emitters are operating in parallel. Single emitter data were calculated by assuming a linear relationship with multiplexed data. However, measurements have demonstrated that emission properties are not spatially uniform across arrays [55], demonstrating that inter-emitter coupling effects are present. Thus, to properly validate the end-to-end model, future work should be validated against single-emitter measurements, which were not available at the time the EHD meniscus model was developed. In addition, future computational research would benefit from improved current measuring capability as field emission is a nano-scale phenomenon and present-day diagnostics are incapable of resolving such small scales, partially due to the contribution of secondary emission from external factors such as facility effects.

- **Simulation of multiple emitters operating in parallel**

  As mentioned in the previous recommendation, emission characteristics of electrospray thruster arrays operating in parallel display spatial nonuniformities. It has been postulated that this is due to varying hydraulic transport experienced by each emitter due to the passively-fed porous configuration and the onset of multiple emission sites emerging from the single emitter [55]. The EHD meniscus model described in this dissertation could be utilized as a basis to explore such phenomena in future work. For example, an upstream model could be appended that simulates the flow of

propellant through the porous substrate and initializes the inlet conditions of the EHD meniscus model. Parallel simulations of the EHD model with perturbations in the inlet model could quantity the effects that pore size variability may play on emission characteristics. Additionally, future work could consider configuring the EHD meniscus model to explore for potential operating conditions that result in steady-state morphologies where more than one emission site may emerge.

Bibliography

[1] Ona-Olapo Adeola, Esho, Tosin Iluyomade, Tosin Olatunde, and Osayi Philip Igbinenikaro. Electrical propulsion systems for satellites: A review of current technologies and future prospects. International Journal of Frontiers in Engineering and Technology Research, 6:35–044, April 2024. doi: 10.53294/ijfetr.2024.6.2.0034.

[2] N. N. Antropov, A. V. Bogatyy, V. N. Boykachev, G. A. Dyakonov, N. V. Lyubinskaya, G. A. Popov, S. A. Semenikhin, V. K. Tyutin, and V. N. Yakovlev. Development of Russian next-generation ablative pulsed plasma thrusters. Procedia engineering, 185: 53–60, 2017.

[3] Jeffrey Asher, Ziyu Huang, Chen Cui, and Joseph Wang. Multi-scale modeling of ionic electrospray emission. Journal of Applied Physics, 131(1):014902, January 2022. ISSN 0021-8979, 1089-7550. doi: 10.1063/5.0071483.

[4] Jeffrey S. Asher and Joseph Wang. Three-Dimensional Particle-in-Cell Simulations of Bipolar Ionic Electrospray Thruster Plume. Journal of Propulsion and Power, 38(4): 573–580, 2022. ISSN 0748-4658. doi: 10.2514/1.B38610.

[5] Meusnier J. B. Memoire sur la courbure des surfaces. Mem des savan etrangers, 10 (1776):477–510, 1785.

[6] Satish Balay, Shrirang Abhyankar, Mark Adams, Jed Brown, Peter Brune, Kris Buschelman, Lisandro Dalcin, Alp Dener, Victor Eijkhout, and William Gropp. PETSc users manual. 2019.

[7] Igor A. Baratta, Joseph P. Dean, Jørgen S. Dokken, Michal Habera, Jack Hale, Chris N. Richardson, Marie E. Rognes, Matthew W. Scroggs, Nathan Sime, and Garth N. Wells. DOLFINx: The next generation FEniCS problem solving environment. Zenodo, December 2023. doi: 10.5281/zenodo.10447666.

[8] A. Barrero, J. M. López-Herrera, A. Boucard, I. G. Loscertales, and M. Márquez. Steady cone-jet electrosprays in liquid insulator baths. Journal of Colloid and Interface Science, 272(1):104–108, April 2004. ISSN 0021-9797. doi: 10.1016/j.jcis.2003.10.035.

[9] John W. Barrett and Charles M. Elliott. Finite element approximation of the Dirichlet problem using the boundary penalty method. Numerische Mathematik, 49(4):343–366, July 1986. ISSN 0029-599X, 0945-3245. doi: 10.1007/BF01389536.

[10] Peter Bastian, Felix Heimann, and Sven Marnach. Generic implementation of finite element methods in the Distributed and Unified Numerics Environment (DUNE). Kybernetika, 46(2):294–315, 2010. ISSN 0023-5954.

[11] T. Bates, J. Mahoney, R. Moore, J. Perel, and A. Yahiku. Research on a charged particle bipolar thrustor. In 6th Electric Propulsion and Plasmadynamics Conference, Colorado Springs,CO,U.S.A., September 1967. American Institute of Aeronautics and Astronautics. doi: 10.2514/6.1967-728.

[12] Graeme A. Bird. Molecular Gas Dynamics and the Direct Simulation of Gas Flows. Oxford university press, 1994.

[13] Markus Blatt, Ansgar Burchardt, Andreas Dedner, Christian Engwer, Jorrit Fahlke, Bernd Flemisch, Christoph Gersbacher, Carsten Gräser, Felix Gruber, Christoph Grüninger, Dominic Kempf, Robert Klöfkorn, Tobias Malkmus, Steffen Müthing, Martin Nolte, Marian Piatkowski, and Oliver Sander. The Distributed and Unified Numerics Environment, Version 2.4. Archive of Numerical Software, 4(100):13–29, May 2016. ISSN 2197-8263. doi: 10.11588/ans.2016.100.26526.

[14] Arnaud Borner and Deborah A. Levin. Coupled Molecular Dynamics—3-D Poisson Simulations of Ionic Liquid Electrospray Thrusters. IEEE Transactions on Plasma Science, 43(1):295–304, January 2015. ISSN 1939-9375. doi: 10.1109/TPS.2014.2327913.

[15] Arnaud Borner, Zheng Li, and Deborah A. Levin. Prediction of Fundamental Properties of Ionic Liquid Electrospray Thrusters using Molecular Dynamics. The Journal of Physical Chemistry B, 117(22):6768–6781, June 2013. ISSN 1520-6106. doi: 10.1021/jp402092e.

[16] Iain D. Boyd and Thomas E. Schwartzentruber. Nonequilibrium Gas Dynamics and Molecular Simulation. Cambridge University Press, March 2017. ISBN 978-1-107-07344-9.

[17] Iain D. Boyd and John T. Yim. Modeling of the near field plume of a Hall thruster. Journal of Applied Physics, 95(9):4575–4584, May 2004. ISSN 0021-8979, 1089-7550. doi: 10.1063/1.1688444.

[18] M. Bretti. Ais-ilis1 ionic liquid ion source electrospray thruster. Applied Ion Systems LLC, 2020.

[19] Natalya Brikner and Paulo C. Lozano. The role of upstream distal electrodes in mitigating electrochemical degradation of ionic liquid ion sources. Applied Physics Letters, 101(19):193504, November 2012. ISSN 0003-6951. doi: 10.1063/1.4766293.

[20] Natalya Anna Brikner. On the Identification and Mitigation of Life-Limiting Mechanisms of Ionic Liquid Ion Sources Envisaged for Propulsion of Microspacecraft. Thesis, Massachusetts Institute of Technology, 2015.

[21] John R. Brophy. NASA's Deep Space 1 ion engine (plenary). Review of Scientific Instruments, 73(2):1071–1078, 2002.

[22] Sílvio Cândido and José C. Páscoa. Dynamics of three-dimensional electrohydrodynamic instabilities on Taylor cone jets using a numerical approach. Physics of Fluids, 35(5): 052110, May 2023. ISSN 1070-6631. doi: 10.1063/5.0151109.

[23] Chong Chen, Maolin Chen, Wei Fan, and Haohao Zhou. Effects of non-uniform operation of emission sites on characteristics of a porous electrospray thruster. Acta Astronautica, 178:192–202, January 2021. ISSN 0094-5765. doi: 10.1016/j.actaastro.2020.09.002.

[24] Yongjun Choi. Modeling an Anode Layer Hall Thruster and Its Plume. Thesis, University of Michigan, 2008.

[25] M. Cloupeau. Recipes for use of EHD spraying in cone-jet mode and notes on corona discharge effects. Journal of Aerosol Science, 25(6):1143–1157, September 1994. ISSN 0021-8502. doi: 10.1016/0021-8502(94)90206-2.

[26] M. Cloupeau and B. Prunet-Foch. Electrostatic spraying of liquids in cone-jet mode. Journal of Electrostatics, 22(2):135–159, July 1989. ISSN 0304-3886. doi: 10.1016/0304-3886(89)90081-8.

[27] M. Cloupeau and B. Prunet-Foch. Electrostatic spraying of liquids: Main functioning modes. Journal of Electrostatics, 25(2):165–184, October 1990. ISSN 0304-3886. doi: 10.1016/0304-3886(90)90025-Q.

[28] Michel Cloupeau and Bernard Prunet-Foch. Electrohydrodynamic spraying functioning modes: A critical review. Journal of Aerosol Science, 25(6):1021–1036, September 1994. ISSN 0021-8502. doi: 10.1016/0021-8502(94)90199-6.

[29] Chase Coffman, Manuel Martínez-Sánchez, F. J. Higuera, and Paulo C. Lozano. Structure of the menisci of leaky dielectric liquids during electrically-assisted evaporation of ions. Applied Physics Letters, 109(23):231602, December 2016. ISSN 0003-6951. doi: 10.1063/1.4971778.

[30] Chase S. Coffman, Manuel Martínez-Sánchez, and Paulo C. Lozano. Electrohydrodynamics of an ionic liquid meniscus during evaporation of ions in a regime of high electric field. Physical Review E, 99(6):063108, June 2019. ISSN 2470-0045, 2470-0053. doi: 10.1103/PhysRevE.99.063108.

[31] Chase Spenser Coffman. Electrically-Assisted Evaporation of Charged Fluids : Fundamental Modeling and Studies on Ionic Liquids. Thesis, Massachusetts Institute of Technology, 2016.

[32] Daniel G. Courtney and Herbert Shea. Influences of porous reservoir Laplace pressure on emissions from passively fed ionic liquid electrospray sources. Applied Physics Letters, 107(10):103504, September 2015. ISSN 0003-6951, 1077-3118. doi: 10.1063/1.4930231.

[33] Chen Cui and Joseph Wang. Simulations of Pure Ionic Electrospray Thruster Plume Neutralization. In AIAA Propulsion and Energy 2020 Forum, AIAA Propulsion and Energy Forum. American Institute of Aeronautics and Astronautics, August 2020. doi: 10.2514/6.2020-3613.

[34] A. de Boer, M. S. van der Schoot, and H. Bijl. Mesh deformation based on radial basis function interpolation. Computers & Structures, 85(11):784–795, June 2007. ISSN 0045-7949. doi: 10.1016/j.compstruc.2007.01.013.

[35] L. de Juan and J. Fernández de la Mora. Charge and Size Distributions of Electrospray Drops. Journal of Colloid and Interface Science, 186(2):280–293, February 1997. ISSN 0021-9797. doi: 10.1006/jcis.1996.4654.

[36] Johan Kølsen de Wit, Mads Givskov Senstius, Asbjørn Clod Pedersen, Riccardo Ragona, and Stefan Kragh Nielsen. Two-plasmon decay of microwaves in low temperature magnetized laboratory plasmas. EPJ Web of Conferences, 313:01002, 2024. ISSN 2100-014X. doi: 10.1051/epjconf/202431301002.

[37] Andreas Dedner, Stefan Girke, Robert Klöfkorn, and Tobias Malkmus. The DUNE-FEM-DG module. Archive of Numerical Software, 5(1):21–61, April 2017. ISSN 2197-8263. doi: 10.11588/ans.2017.1.28602.

[38] Jim Douglas and Todd Dupont. Interior Penalty Procedures for Elliptic and Parabolic Galerkin Methods. In R. Glowinski and J. L. Lions, editors, Computing Methods in Applied Sciences, Lecture Notes in Physics, pages 207–216, Berlin, Heidelberg, 1976. Springer. ISBN 978-3-540-37550-0. doi: 10.1007/BFb0120591.

[39] Rainer A. Dressler, Benjamin St. Peter, Yu-Hui Chiu, and Timothy Fedkiw. Multiple Emission Sites on Porous Glass Electrospray Propulsion Emitters Using Dielectric Propellants. Journal of Propulsion and Power, pages 1–13, April 2022. ISSN 1533-3876. doi: 10.2514/1.B38453.

[40] Michael Dropmann, Manfred Ehresmann, A. S. Pagan, Quang Hoa Le, Francesco Romano, Christoph Montag, and Georg Herdrich. Low Power Arcjet Application for End of Life Satellite Servicing. In Proceedings of the 7th European Conference on Space Debri, Darmstadt, Germany, pages 18–21, 2017.

[41] Kazuma Emoto, Toshiyuki Tsuchiya, and Yoshinori Takao. Numerical Investigation of Steady and Transient Ion Beam Extraction Mechanisms for Electrospray Thrusters. Transactions of the Japan Society for Aeronautical and Space Sciences, Aerospace Technology Japan, 16(2):110–115, 2018. doi: 10.2322/tastj.16.110.

[42] Juan Fernández de la Mora. The Fluid Dynamics of Taylor Cones. Annual Review of Fluid Mechanics, 39(1):217–243, 2007. doi: 10.1146/annurev.fluid.39.050905.110159.

[43] Lord Rayleigh F.R.S. On the equilibrium of liquid conducting masses charged with electricity. The London, Edinburgh, and Dublin Philosophical Magazine and Journal of Science, September 1882. doi: 10.1080/14786448208628425.

[44] A. M. Gañán-Calvo, J. Dávila, and A. Barrero. Current and droplet size in the electrospraying of liquids. Scaling laws. Journal of Aerosol Science, 28(2):249–275, March 1997. ISSN 0021-8502. doi: 10.1016/S0021-8502(96)00433-8.

[45] Alfonso M. Gañán-Calvo. On the general scaling theory for electrospraying. Journal of Fluid Mechanics, 507:203–212a, July 2004. ISSN 1469-7645, 0022-1120. doi: 10.1017/S0022112004008870.

[46] M. D. Gabovich. Liquid-metal ion emitters. Soviet Physics Uspekhi, 26(5):447, May 1983. ISSN 0038-5670. doi: 10.1070/PU1983v026n05ABEH004407.

[47] Ximo Gallud and Paulo C. Lozano. The emission properties, structure and stability of ionic liquid menisci undergoing electrically assisted ion evaporation. Journal of Fluid Mechanics, 933:A43, February 2022. ISSN 0022-1120, 1469-7645. doi: 10.1017/jfm.2021.988.

[48] M. Gamero-Castaño and J. Fernández de la Mora. Direct measurement of ion evaporation kinetics from electrified liquid surfaces. The Journal of Chemical Physics, 113(2):815–832, July 2000. ISSN 0021-9606. doi: 10.1063/1.481857.

[49] M. Gamero-Castaño and J. Fernández de la Mora. Direct measurement of ion evaporation kinetics from electrified liquid surfaces. The Journal of Chemical Physics, 113(2):815–832, July 2000. ISSN 0021-9606. doi: 10.1063/1.481857.

[50] Manuel Gamero-Castaño and Vladimir Hruby. Electric measurements of charged sprays emitted by cone-jets. Journal of Fluid Mechanics, 459:245–276, May 2002. ISSN 1469-7645, 0022-1120. doi: 10.1017/S002211200200798X.

[51] Manuel Gamero-Castaño and M. Magnani. The minimum flow rate of electrosprays in the cone-jet mode. Journal of Fluid Mechanics, 876:553–572, October 2019. ISSN 0022-1120, 1469-7645. doi: 10.1017/jfm.2019.569.

[52] Paul N. Giuliano and Iain D. Boyd. Particle simulation of collision dynamics for ion beam injection into a rarefied gas. Physics of Plasmas, 20(3):033505, March 2013. ISSN 1070-664X, 1089-7674. doi: 10.1063/1.4794954.

[53] R. H. Goddard. The green notebooks, vol. 1. The Dr. Robert H. Goddard Collection at Clark University Archives, Clark University, Worceseter, MA, 1610, 1906.

[54] David J. Griffiths. Introduction to Electrodynamics. Cambridge University Press, November 2023. ISBN 978-1-00-939775-9.

[55] C. Guerra-Garcia, D. Krejci, and P. Lozano. Spatial uniformity of the current emitted by an array of passively fed electrospray porous emitters. Journal of Physics D: Applied Physics, 49(11):115503, February 2016. ISSN 0022-3727. doi: 10.1088/0022-3727/49/11/115503.

[56] I. Guerrero, R. Bocanegra, F. J. Higuera, and J. Fernandez De La Mora. Ion evaporation from Taylor cones of propylene carbonate mixed with ionic liquids. Journal of Fluid Mechanics, 591:437–459, November 2007. ISSN 0022-1120, 1469-7645. doi: 10.1017/S0022112007008348.

[57] I. Guerrero, R. Bocanegra, F. J. Higuera, and J. Fernandez De La Mora. Ion evaporation from Taylor cones of propylene carbonate mixed with ionic liquids. Journal of Fluid Mechanics, 591:437–459, November 2007. ISSN 1469-7645, 0022-1120. doi: 10.1017/S0022112007008348.

[58] I. Hayati, A. I. Bailey, and Th. F. Tadros. Mechanism of stable jet formation in electrohydrodynamic atomization. Nature, 319(6048):41–43, January 1986. ISSN 0028-0836, 1476-4687. doi: 10.1038/319041a0.

[59] G. Herdrich, T. Binder, A. Boxberger, A. Chadwick, Y. A. Chan, M. Ehresmann, N. Harmansa, Ch Montag, F. Romano, and J. Skalden. Research and development on electric and advanced propulsion at IRS. In Proceedings of the 35th International Electric Propulsion Conference, Atlanta, GA, USA, pages 8–12, 2017.

[60] F. J. Higuera. Flow rate and electric current emitted by a Taylor cone. Journal of Fluid Mechanics, 484:303–327, June 2003. ISSN 1469-7645, 0022-1120. doi: 10.1017/S0022112003004385.

[61] F. J. Higuera. Liquid flow induced by ion evaporation in an electrified meniscus. Physical Review E, 69(6):066301, June 2004. doi: 10.1103/PhysRevE.69.066301.

[62] F. J. Higuera. Breakup of a supported drop of a viscous conducting liquid in a uniform electric field. Physical Review E, 78(1):016314, July 2008. ISSN 1539-3755, 1550-2376. doi: 10.1103/PhysRevE.78.016314.

[63] F. J. Higuera. Model of the meniscus of an ionic-liquid ion source. Physical Review E, 77(2):026308, February 2008. ISSN 1539-3755, 1550-2376. doi: 10.1103/PhysRevE.77.026308.

[64] C. W Hirt, A. A Amsden, and J. L Cook. An arbitrary Lagrangian-Eulerian computing method for all flow speeds. Journal of Computational Physics, 14(3):227–253, March 1974. ISSN 0021-9991. doi: 10.1016/0021-9991(74)90051-5.

[65] J. V. Iribarne. On the evaporation of small ions from charged droplets. The Journal of Chemical Physics, 64(6):2287, 1976. ISSN 00219606. doi: 10.1063/1.432536.

[66] J. V. Iribarne and B. A. Thomson. On the evaporation of small ions from charged droplets. The Journal of Chemical Physics, 64(6):2287–2294, March 1976. ISSN 0021-9606. doi: 10.1063/1.432536.

[67] Hani Kamhawi, Thomas Haag, David Jacobson, and David Manzella. Performance Evaluation of the NASA-300M 20 kW Hall Thruster. In 47th AIAA/ASME/SAE/ASEE Joint Propulsion Conference & Exhibit, San Diego, California, July 2011. American Institute of Aeronautics and Astronautics. ISBN 978-1-60086-949-5. doi: 10.2514/6.2011-5521.

[68] David Krejci, Fernando Mier-Hicks, Robert Thomas, Thomas Haag, and Paulo Lozano. Emission Characteristics of Passively Fed Electrospray Microthrusters with Propellant Reservoirs. Journal of Spacecraft and Rockets, 54(2):447–458, March 2017. ISSN 0022-4650, 1533-6794. doi: 10.2514/1.A33531.

[69] Renato Krpoun and Herbert R. Shea. A method to determine the onset voltage of single and arrays of electrospray emitters. Journal of Applied Physics, 104(6):064511, September 2008. ISSN 0021-8979. doi: 10.1063/1.2981077.

[70] L. D. Landau, J. S. Bell, M. J. Kearsley, L. P. Pitaevskii, E. M. Lifshitz, and J. B. Sykes. Electrodynamics of Continuous Media. Elsevier, 1960. ISBN 978-1-4832-9375-2.

[71] Michael LaPointe, E. Strzempkowski, and E. Pencil. High Power MPD Thruster Performance Measurements. In 40th AIAA/ASME/SAE/ASEE Joint Propulsion Conference and Exhibit, Fort Lauderdale, Florida, July 2004. American Institute of Aeronautics and Astronautics. ISBN 978-1-62410-037-6. doi: 10.2514/6.2004-3467.

[72] Robert S. Legge and Paulo C. Lozano. Electrospray Propulsion Based on Emitters Microfabricated in Porous Metals. Journal of Propulsion and Power, 27(2):485–495, March 2011. ISSN 0748-4658, 1533-3876. doi: 10.2514/1.50037.

[73] Zhigang Lei, Biaohua Chen, Yoon-Mo Koo, and Douglas R. MacFarlane. Introduction: Ionic Liquids. Chemical Reviews, 117(10):6633–6635, May 2017. ISSN 1520-6890. doi: 10.1021/acs.chemrev.7b00246.

[74] Kristina Lemmer. Propulsion for CubeSats. Acta Astronautica, 134:231–243, May 2017. ISSN 0094-5765. doi: 10.1016/j.actaastro.2017.01.048.

[75] Dan Lev, Roger M. Myers, Kristina M. Lemmer, Jonathan Kolbeck, Hiroyuki Koizumi, and Kurt Polzin. The technological and commercial expansion of electric propulsion. Acta Astronautica, 159:213–227, June 2019. ISSN 0094-5765. doi: 10.1016/j.actaastro.2019.03.058.

[76] Juan Carlos De los Reyes. Numerical PDE-Constrained Optimization. Springer, February 2015. ISBN 978-3-319-13395-9.

[77] I. G. Loscertales and J. Fernández de la Mora. Experiments on the kinetics of field evaporation of small ions from droplets. The Journal of Chemical Physics, 103(12): 5041–5060, September 1995. ISSN 0021-9606, 1089-7690. doi: 10.1063/1.470591.

[78] I. G. Loscertales and J. Fernández de la Mora. Experiments on the kinetics of field evaporation of small ions from droplets. The Journal of Chemical Physics, 103(12): 5041–5060, September 1995. ISSN 0021-9606. doi: 10.1063/1.470591.

[79] S. Lounes-Mahloul, N. Oudini, and A. Bendib. Numerical study of the collisionless interaction between positive and negative ion beams. Physics of Plasmas, 25(4):043505, April 2018. ISSN 1070-664X. doi: 10.1063/1.5022730.

[80] Paulo Lozano and Manuel Martínez-Sánchez. Ionic liquid ion sources: Suppression of electrochemical reactions using voltage alternation. Journal of Colloid and Interface Science, 280(1):149–154, December 2004. ISSN 0021-9797. doi: 10.1016/j.jcis.2004.07.037.

[81] Paulo Lozano and Manuel Martinez-Sanchez. Efficiency Estimation of EMI-BF4 Ionic Liquid Electrospray Thrusters. In 41st AIAA/ASME/SAE/ASEE Joint Propulsion Conference & Exhibit, Tucson, Arizona, July 2005. American Institute of Aeronautics and Astronautics. ISBN 978-1-62410-063-5. doi: 10.2514/6.2005-4388.

[82] W. D. Luedtke, Uzi Landman, Y.-H. Chiu, D. J. Levandier, R. A. Dressler, S. Sok, and M. S. Gordon. Nanojets, Electrospray, and Ion Field Evaporation: Molecular Dynamics Simulations and Laboratory Experiments. The Journal of Physical Chemistry A, 112 (40):9628–9649, October 2008. ISSN 1089-5639. doi: 10.1021/jp804585y.

[83] Marco Magnani and Manuel Gamero. Modeling of the Dissipation and Self-Heating of the Propellant in Electrospray Thrusters. In AIAA Propulsion and Energy 2019 Forum, Indianapolis, IN, August 2019. American Institute of Aeronautics and Astronautics. ISBN 978-1-62410-590-6. doi: 10.2514/6.2019-4171.

[84] John F. Mahoney, Arthur Y. Yahiku, Howard L. Daley, R. David Moore, and Julius Perel. Electrohydrodynamic ion source. Journal of Applied Physics, 40(13):5101–5106, 1969.

[85] Joaquim R. R. A. Martins and Andrew Ning. Engineering Design Optimization. Cambridge University Press, November 2021. ISBN 978-1-108-83341-7.

[86] K. Matyash, R. Schneider, F. Taccogna, A. Hatayama, S. Longo, M. Capitelli, D. Tskhakaya, and F. X. Bronold. Particle in Cell Simulation of Low Temperature Laboratory Plasmas. Contributions to Plasma Physics, 47(8-9):595–634, 2007. ISSN 1521-3986. doi: 10.1002/ctpp.200710073.

[87] Stéphane Mazouffre. Electric propulsion for satellites and spacecraft: Established technologies and novel approaches. Plasma Sources Science and Technology, 25(3): 033002, April 2016. ISSN 0963-0252. doi: 10.1088/0963-0252/25/3/033002.

[88] Jonathan C. McDowell. The Low Earth Orbit Satellite Population and Impacts of the SpaceX Starlink Constellation. The Astrophysical Journal Letters, 892(2):L36, April 2020. ISSN 2041-8205. doi: 10.3847/2041-8213/ab8016.

[89] Neil A. Mehta and Deborah A. Levin. Molecular dynamics electrospray simulations of coarse-grained ethylammonium nitrate (EAN) and 1-ethyl-3-methylimidazolium tetrafluoroborate (EMIM-BF4). Aerospace, 5(1):1, 2017.

[90] Neil A. Mehta and Deborah A. Levin. Molecular Dynamics Electrospray Simulations of Coarse-Grained Ethylammonium Nitrate (EAN) and 1-Ethyl-3-Methylimidazolium Tetrafluoroborate (EMIM-BF4). Aerospace, 5(1):1, March 2018. ISSN 2226-4310. doi: 10.3390/aerospace5010001.

[91] Neil A. Mehta and Deborah A. Levin. Sensitivity of electrospray molecular dynamics simulations to long-range Coulomb interaction models. Physical Review E, 97(3): 033306, March 2018. doi: 10.1103/PhysRevE.97.033306.

[92] J R Melcher and G I Taylor. Electrohydrodynamics: A Review of the Role of Interfacial Shear Stresses. Annual Review of Fluid Mechanics, 1(1):111–146, January 1969. ISSN 0066-4189, 1545-4479. doi: 10.1146/annurev.fl.01.010169.000551.

[93] T. M. Mel'kumov. Pioneers of Rocket Technology: Selected Works. National Aeronautics and Space Administration, 1965.

[94] Mackenzie Meyer, Matthew Byrne, Benjamin Jorns, and Iain D. Boyd. Erosion of a meshed reflector in the plume of a Hall effect thruster, Part 1: Modeling. In AIAA Propulsion and Energy 2019 Forum, Indianapolis, IN, August 2019. American Institute of Aeronautics and Astronautics. ISBN 978-1-62410-590-6. doi: 10.2514/6.2019-3987.

[95] Catherine E. Miller and Paulo C. Lozano. Measurement of the dissociation rates of ion clusters in ionic liquid ion sources. Applied Physics Letters, 116(25):254101, June 2020. ISSN 0003-6951. doi: 10.1063/5.0006529.

[96] J. Fernández De La Mora and I. G. Loscertales. The current emitted by highly conducting Taylor cones. Journal of Fluid Mechanics, 260:155–184, February 1994. ISSN 1469-7645, 0022-1120. doi: 10.1017/S0022112094003472.

[97] Juergen Mueller. Thruster options for microspacecraft: A review and evaluation of state-of-the-art and emerging technologies. Micropropulsion for small spacecraft, 147: 45, 2000.

[98] Juergen Mueller, Richard Hofer, and John Ziemer. Survey of propulsion technologies applicable to cubesats. May 2010.

[99] M R Natisin, H L Zamora, W A McGehee, N I Arnold, Z A Holley, M R Holmes, and D Eckhardt. Fabrication and characterization of a fully conventionally machined, high-performance porous-media electrospray thruster. Journal of Micromechanics and

Microengineering, 30(11):115021, November 2020. ISSN 0960-1317, 1361-6439. doi: 10.1088/1361-6439/abb8c3.

[100] Nakul Nuwal, Victor A. Azevedo, Matthew R. Klosterman, Siddharth Budaraju, Deborah A. Levin, and Joshua L. Rovey. Multiscale modeling of fragmentation in an electrospray plume. Journal of Applied Physics, 130(18):184903, November 2021. ISSN 0021-8979, 1089-7550. doi: 10.1063/5.0064711.

[101] Hermann Oberth. Wege Zur Raumschiffahrt. Walter de Gruyter GmbH & Co KG, 2019.

[102] Dillon O'Reilly, Georg Herdrich, and Darren F. Kavanagh. Electric Propulsion Methods for Small Satellites: A Review. Aerospace, 8(1):22, January 2021. ISSN 2226-4310. doi: 10.3390/aerospace8010022.

[103] C. Pantano, A. M. Gañán-Calvo, and A. Barrero. Zeroth-order, electrohydrostatic solution for electrospraying in cone-jet mode. Journal of Aerosol Science, 25(6):1065–1077, September 1994. ISSN 0021-8502. doi: 10.1016/0021-8502(94)90202-X.

[104] Julius Perel. Alkali metal ion sources. Journal of the Electrochemical Society, 115(12): 343C, 1968.

[105] Elaine M. Petro, Ximo Gallud, Sebastian K. Hampl, Madeleine Schroeder, Carl Geiger, and Paulo C. Lozano. Multiscale modeling of electrospray ion emission. Journal of Applied Physics, 131(19):193301, May 2022. ISSN 0021-8979. doi: 10.1063/5.0065615.

[106] Kurt A. Polzin, Thomas E. Markusic, Boris J. Stanojev, Amado DeHoyos, Yevgeny Raitses, Artem Smirnov, and Nathaniel J. Fisch. Performance of a Low-Power Cylindrical Hall Thruster. Journal of Propulsion and Power, 23(4):886–888, July 2007. ISSN 0748-4658, 1533-3876. doi: 10.2514/1.28595.

[107] I. Romero-Sanz, R. Bocanegra, J. Fernandez de la Mora, and M. Gamero-Castaño. Source of heavy molecular ions based on Taylor cones of ionic liquids operating in the pure ion evaporation regime. Journal of Applied Physics, 94(5):3599–3605, September 2003. ISSN 0021-8979. doi: 10.1063/1.1598281.

[108] Youcef Saad and Martin H. Schultz. GMRES: A Generalized Minimal Residual Algorithm for Solving Nonsymmetric Linear Systems. SIAM Journal on Scientific and Statistical Computing, 7(3):856–869, July 1986. ISSN 0196-5204. doi: 10.1137/0907058.

[109] Lara Galán Sánchez, Josep Ribé Espel, Ferdy Onink, G. Wytze Meindersma, and André B. de Haan. Density, Viscosity, and Surface Tension of Synthesis Grade Imidazolium, Pyridinium, and Pyrrolidinium Based Room Temperature Ionic Liquids. Journal of Chemical & Engineering Data, 54(10):2803–2812, October 2009. ISSN 0021-9568. doi: 10.1021/je800710p.

[110] D. A. Saville. ELECTROHYDRODYNAMICS:The Taylor-Melcher Leaky Dielectric Model. Annual Review of Fluid Mechanics, 29(1):27–64, January 1997. ISSN 0066-4189, 1545-4479. doi: 10.1146/annurev.fluid.29.1.27.

[111] M. M. Selim and R. P. Koomullil. Mesh Deformation Approaches – A Survey. Journal of Physical Mathematics, 7(2):1–9, January 2016. ISSN 2090-0899, 2090-0902. doi: 10.4172/2090-0902.1000181.

[112] Leslie R. Shepherd and A. Val Cleaver. The atomic rocket. IV. J. Brit. Interplanetary Soc., 8, 1949.

[113] Jonathan Shewchuk. What is a good linear finite element? interpolation, conditioning, anisotropy, and quality measures (preprint). University of California at Berkeley, 2002, 2002.

[114] Adler G. Smith and Elaine M. Petro. Propagating an Electrospray Emission Model to Array Scales Using Particle-in-Cell. Journal of Propulsion and Power, 40(5):677–690, 2024. ISSN 0748-4658. doi: 10.2514/1.B39400.

[115] K. A. Stephani, I. D. Boyd, R. L. Balthazor, M. G. McHarg, B. A. Mueller, and R. J. Adams. Analysis and observation of spacecraft plume/ionosphere interactions during maneuvers of the space shuttle. Journal of Geophysical Research: Space Physics, 119 (9):7636–7648, 2014. ISSN 2169-9402. doi: 10.1002/2013JA019476.

[116] E. Stuhlinger. Possibilities of Electrical Space Ship Propulsion. In Friedrich Hecht, editor, Bericht über den V. Internationalen Astronautischen Kongreß, pages 100–119. Springer Berlin Heidelberg, Berlin, Heidelberg, 1955. ISBN 978-3-662-37558-7 978-3-662-38334-6. doi: 10.1007/978-3-662-38334-6_7.

[117] E. Stuhlinger. Electrical propulsion system for space ships with nuclear source: Part II. Journal of Astronautics, 3:11, 1956.

[118] Ernst Stuhlinger. Electrical propulsion system for space ships with nuclear power source. Journal of the Astronautical Sciences, 2(Pt 1):149–152, 1955.

[119] James Szabo, Bruce Pote, Surjeet Paintal, Mike Robin, Adam Hillier, Richard D. Branam, and Richard E. Huffmann. Performance Evaluation of an Iodine-Vapor Hall Thruster. Journal of Propulsion and Power, 28(4):848–857, July 2012. ISSN 0748-4658, 1533-3876. doi: 10.2514/1.B34291.

[120] G. I. Taylor and A. D. McEwan. The stability of a horizontal fluid interface in a vertical electric field. Journal of Fluid Mechanics, 22(1):1–15, May 1965. ISSN 1469-7645, 0022-1120. doi: 10.1017/S0022112065000538.

[121] Geoffrey Ingram Taylor. Disintegration of water drops in an electric field. Proceedings of the Royal Society of London. Series A. Mathematical and Physical Sciences, 280 (1382):383–397, July 1964. doi: 10.1098/rspa.1964.0151.

[122] Geoffrey Ingram Taylor, A. D. McEwan, and L. N. J. de Jong. Studies in electrohydrodynamics. I. The circulation produced in a drop by an electric field. Proceedings of the Royal Society of London. Series A. Mathematical and Physical Sciences, 291(1425): 159–166, April 1966. doi: 10.1098/rspa.1966.0086.

[123] A. Thuppul, A. L. Collins, P. L. Wright, N. M. Uchizono, and R. E. Wirz. Mass flux and current density distributions of electrospray plumes. Journal of Applied Physics, 130(10):103301, September 2021. ISSN 0021-8979, 1089-7550. doi: 10.1063/5.0056761.

[124] Anirudh Thuppul, Peter L. Wright, Adam L. Collins, John K. Ziemer, and Richard E. Wirz. Lifetime Considerations for Electrospray Thrusters. Aerospace, 7(8):108, August 2020. ISSN 2226-4310. doi: 10.3390/aerospace7080108.

[125] D. Tskhakaya, K. Matyash, R. Schneider, and F. Taccogna. The Particle-In-Cell Method. Contributions to Plasma Physics, 47(8-9):563–594, 2007. ISSN 1521-3986. doi: 10.1002/ctpp.200710072.

[126] Akshay Reddy Tummala and Atri Dutta. An overview of cube-satellite propulsion technologies and trends. Aerospace, 4(4):58, 2017.

[127] Fred K. Wohlhuter and Osman A. Basaran. Shapes and stability of pendant and sessile dielectric drops in an electric field. Journal of Fluid Mechanics, 235:481–510, February 1992. ISSN 1469-7645, 0022-1120. doi: 10.1017/S0022112092001198.

[128] Barbara I. Wohlmuth. Discretization Methods and Iterative Solvers Based on Domain Decomposition, volume 17 of Lecture Notes in Computational Science and Engineering. Springer, Berlin, Heidelberg, 2001. ISBN 978-3-540-41083-6 978-3-642-56767-4. doi: 10.1007/978-3-642-56767-4.

[129] B. Wollenhaupt, Alex Hammer, Georg Herdrich, Stefanos Fasoulas, and H. Roser. A very low power arcjet (VELARC) for small satellite missions. In 32nd International Electric Propulsion Conference, Wiesbaden, Germany, pages 1988–2007. Citeseer, 2011.

[130] R. J. Young. P. D. Prewett and G. L. R. Mair Focused Ion Beams from Liquid Metal Ion Sources Research Studies Press. 344pp; Price £52.50; $108.70. ISBN 0863 80120X, Wiley 0471 930881. (1991). Surface and Interface Analysis, 18(5):377–377, 1992. ISSN 1096-9918. doi: 10.1002/sia.740180511.

[131] John Zeleny. Instability of Electrified Liquid Surfaces. Physical Review, 10(1):1–6, July 1917. doi: 10.1103/PhysRev.10.1.

[132] John Zeleny. The role of surface instability in electrical discharges from drops of alcohol and water in air at atmospheric pressure. Journal of the Franklin Institute, 219(6): 659–675, June 1935. ISSN 0016-0032. doi: 10.1016/S0016-0032(35)91985-8.

[133] Fei Zhang, Xikai Jiang, Gaofeng Chen, Yadong He, Guoqing Hu, and Rui Qiao. Electric-Field-Driven Ion Emission from the Free Surface of Room Temperature Ionic Liquids. The Journal of Physical Chemistry Letters, 12(1):711–716, January 2021. ISSN 1948-7185, 1948-7185. doi: 10.1021/acs.jpclett.0c03335.

[134] John Ziemer and S. Merkowitz. Microthrust Propulsion for the LISA Mission. In 40th AIAA/ASME/SAE/ASEE Joint Propulsion Conference and Exhibit, Fort Lauderdale, Florida, July 2004. American Institute of Aeronautics and Astronautics. ISBN 978-1-62410-037-6. doi: 10.2514/6.2004-3439.

[135] John K. Ziemer, Thomas Randolph, Vlad Hruby, Douglas Spence, Nathaniel Demmons, Tom Roy, William Connolly, Eric Ehrbar, Jurg Zwahlen, and Roy Martin. Colloid Microthrust Propulsion for the Space Technology 7 (ST7) and LISA Missions. AIP Conference Proceedings, 873(1):548–555, November 2006. ISSN 0094-243X. doi: 10.1063/1.2405097.

[136] John K. Ziemer, Thomas M. Randolph, Manuel Gamero-Castaño, Vlad Hruby, William Connolly, Nathaniel Demmons, Eric Ehrbar, Roy Martin, Tom Roy, and Douglas Spence. Flight hardware development of colloid microthruster technology for the space technology 7 and LISA missions. In 30th International Electric Propulsion Conference. Florence Italy, 2007.

[137] Dieter Zube, Dan Fye, Ideo Masuda, and Yoshifumi Gotoh. Low bus voltage hydrazine arcjet system for geostationary satellites. In 34th AIAA/ASME/SAE/ASEE Joint Propulsion Conference and Exhibit, Cleveland,OH,U.S.A., July 1998. American Institute of Aeronautics and Astronautics. doi: 10.2514/6.1998-3631.

Appendix A

Weak Formulation of the Multidomain Laplace Problem

Laplace's equation is used to model the electric potential within the two-dimensional liquid and vacuum domains, Ω_{liq} and Ω_{vac}. The Laplace problem within each domain is coupled by Dirichlet–Neumann conditions at their interface Γ_{int}, with Dirichlet conditions enforced at the remaining boundaries. The electric potential $\phi : \Omega_{vac} \cup \Omega_{liq} \mapsto \mathbb{R}$ solves the boundary value problem

$$\begin{aligned}
\nabla^2 \phi_l &= 0 && \text{in } \Omega_{liq}, \\
\nabla^2 \phi_v &= 0 && \text{in } \Omega_{vac}, \\
[\![\nabla \phi \cdot \hat{\mathbf{n}}]\!] &= f(\phi) && \text{on } \Gamma_{int}, \\
\phi_l &= \phi_v && \text{on } \Gamma_{int}, \\
\phi_l &= 0 && \text{on } \Gamma_{emi} \cup \Gamma_{inl}, \\
\phi_v &= V_0 && \text{on } \Gamma_{ext}, \\
\phi_v &= f(V_0) && \text{on } \Gamma_{sub},
\end{aligned}$$

The solution is defined on a Sobolev space $H^1(\Omega)$, the space of all scalar square–integrable L^2 functions on Ω with weak derivatives in $L^2(\Omega)$, where $\Omega = \Omega_{liq} \cup \Omega_{vac}$. A space is similarly defined for the set of test functions as well,

$$\begin{aligned}
\mathbf{H}^1_{\mathbf{g}}(\Omega) &\coloneqq \{\theta \in H^1(\Omega, \mathbb{R}) \quad : \quad \mathrm{tr}(\theta) = \mathbf{g}\}, \\
L_{2,0}(\Omega) &\coloneqq \{\theta \in L_2(\Omega_{liq}) \quad : \quad \theta|_\Gamma = 0\},
\end{aligned}$$

where

$$\mathbf{g} \coloneqq \begin{cases} \phi_v & \text{on } \Gamma_{int}, \\ 0 & \text{on } \Gamma_{emi} \cup \Gamma_{inl}, \\ V_0 & \text{on } \Gamma_{ext}, \\ f(V_0) & \text{on } \Gamma_{sub}, \end{cases}.$$

Laplace's equation in the boundary value problem is multiplied by a test function θ from its corresponding space and integrated over the boundary Ω. We can present the governing weak formulation using the bilinear form and linear forms

$$a(\phi, \theta) \coloneqq \int_{\Omega} \nabla\phi \cdot \nabla\theta \; d\Omega$$
$$l(\theta) \coloneqq \int_{\Gamma} j\theta \; d\Gamma,$$

where j is the Neumann condition. Representing the weak formulation in this manner does not allow for implementation of the Neumann condition jump across the interfacial boundary. Instead of a traditional Galerkin discretization, a Discontinuous Galerkin discretization is implemented at the interfacial boundary and the problem is reformulated to minimize a discrete residual of the form

$$\text{Find } \phi \in \mathbf{H}^1_{\mathbf{g}}(\Omega) \quad : \quad r^{\text{SIPG}}(\phi, \theta) = 0 \qquad \forall\theta \in L_{2,0}(\Omega),$$

where

$$\begin{aligned} r^{\text{SIPG}}(\phi, \theta) = &\int_{\Omega_{liq}} \nabla\phi \cdot \nabla\theta \; d\Omega_{liq} + \int_{\Omega_{vac}} \nabla\phi \cdot \nabla\theta \; d\Omega_{vac} \\ &- \int_{\Gamma_{int}} \{\langle \nabla\phi, \hat{\mathbf{n}} \rangle\} [\![\theta]\!] \; d\Gamma_{int} - \int_{\Gamma_{int}} \{\langle \nabla\theta, \hat{\mathbf{n}} \rangle\} [\![\phi]\!] \; d\Gamma_{int} \\ &+ \kappa \sum_{\Gamma \in \Gamma_{int}} \frac{1}{h_\Gamma} \int_{\Gamma} [\![\phi]\!][\![\theta]\!] \; d\Gamma_{int} \\ &- \int_{\Gamma_{int}} [\![\langle \nabla\phi, \hat{\mathbf{n}} \rangle]\!] [\![\theta]\!] \; d\Gamma_{int}, \end{aligned}$$

is minimized. $\langle \cdot, \cdot \rangle$ denotes the inner product, κ is a penalty term, and h_Γ is the characteristic length scale of an arbitrary intersection Γ. The first two terms on the right hand side of

represent the volumetric residual within each subdomain, while the following two terms couple the subdomains by penalizing the interfacial jump in potential and enforcing continuity. The final term corresponds to a interfacial jump in the potential gradient.

Appendix B

Weak Formulation of the Stokes Problem

The Stokes equations are used to model a viscous, incompressible fluid in the two-dimension domain Ω_{vac}. The two unknowns in this problem are the fluid velocity field $\mathbf{u} : \Omega_{liq} \mapsto \mathbb{R}^2$ and the fluid pressure $p : \Omega_{liq} \mapsto \mathbb{R}$, where together they solve the boundary value problem

$$\begin{aligned}
\mu\nabla^2\mathbf{u} - \nabla p = 0 \qquad & \text{in } \Omega_{liq}, \\
\nabla \cdot \mathbf{u} = 0 \qquad & \text{in } \Omega_{liq}, \\
\hat{\mathbf{t}} \cdot \nabla\mathbf{u} \cdot \hat{\mathbf{n}} = u_{int}^{\hat{\mathbf{t}}} \qquad & \text{on } \Gamma_{int}, \\
\mathbf{u} \cdot \hat{\mathbf{n}} = u_{int}^{\hat{\mathbf{n}}} \qquad & \text{on } \Gamma_{int}, \\
\mathbf{u} = \mathbf{u}_{inl} \qquad & \text{on } \Gamma_{inl}, \\
\mathbf{u} = 0 \qquad & \text{on } \Gamma_{emi}.
\end{aligned}$$

As the boundary value problem only solves the pressure p up to a constant function, it is defined such that $\int_{\Omega_{liq}} p \, d\Omega_{liq} = 0$. We define the spaces

$$\begin{aligned}
\mathbf{H}^1_{\mathbf{g}}(\Omega_{liq}) &\coloneqq \{\mathbf{v} \in H^1(\Omega_{liq}, \mathbb{R}^2) \quad : \quad \mathrm{tr}(\mathbf{v}) = \mathbf{g}\}, \\
L_{2,0}(\Omega_{liq}) &\coloneqq \{q \in L_2(\Omega_{liq}) \quad : \quad \int_{\Omega_{liq}} q \, d\Omega_{liq} = 0\},
\end{aligned}$$

where

$$\mathbf{g} \coloneqq \begin{cases} \mathbf{u}_{int}^{\hat{\mathbf{n}}} & \text{on } \Gamma_{int} \\ \mathbf{u}_{inl} & \text{on } \Gamma_{inl} \\ 0 & \text{on } \Gamma_{emi} \end{cases} .$$

If $\mathbf{g}$ is sufficiently smooth, the variational problem has a unique solution. The Stokes equations are known to be a saddle point problem, where Taylor-Hood elements are traditionally used to find a stable finite element approximation solution. Taylor-Hood elements combine a quadratic–order interpolation of velocity with a linear–order interpolation of pressure. We also introduce the bilinear forms

$$\begin{aligned} a(\mathbf{u}, \mathbf{v}) &\coloneqq \int_{\Omega_{liq}} \mu \nabla \mathbf{u} : \nabla \mathbf{v} \, d\Omega_{liq}, \\ b(\mathbf{v}, p) &\coloneqq \int_{\Omega_{liq}} (\nabla \cdot \mathbf{v}) p \, d\Omega_{liq}, \\ b(\mathbf{u}, q) &\coloneqq \int_{\Omega_{liq}} (\nabla \cdot \mathbf{u}) q \, d\Omega_{liq}, \end{aligned}$$

where the weak formulation of the Stokes problem is

$$\text{Find } (\mathbf{u}, p) \in \mathbf{H}^1_{\mathbf{g}}(\Omega_{liq}) \times L_{2,0}(\Omega_{liq}) \quad \text{such that}$$

$$\begin{aligned} a(\mathbf{u}, \mathbf{v}) + b(\mathbf{v}, p) &= \frac{\alpha}{h} \int_{\Gamma_{int}} (\mathbf{u} \cdot \hat{\mathbf{n}} - \mathbf{u}_{int}^{\hat{\mathbf{n}}})(\mathbf{v} \cdot \hat{\mathbf{n}}) \, d\Gamma_{int} + \int_{\Gamma_{int}} u_{int}^{\hat{\mathbf{t}}} (\mathbf{v} \cdot \hat{\mathbf{t}}) \, d\Gamma_{int} && \forall \mathbf{v} \in \mathbf{H}^1_0(\Omega_{liq}), \\ b(\mathbf{u}, q) &= 0 && \forall q \in L_{2,0}(\Omega_{liq}). \end{aligned}$$

The first term on the right hand side of the equation corresponding to the velocity test function is a weak enforcement of the Dirichlet condition normal to the interface, while the second term corresponds to the Neumann condition enforced tangential to the interface. The Dirichlet conditions at the inlet Γ_{inl} and emitter boundary Γ_{emi} are enforced strongly and thus are not represented in the weak formulation.